Mehanizam redukcije HMG-CoA katalizirane ljudskom HMG-CoA reduktazom

Mihaljević-Jurič, Paula

Master's thesis / Diplomski rad

2018

University of Osijek
Department of Chemistry
Graduate Study of Chemistry

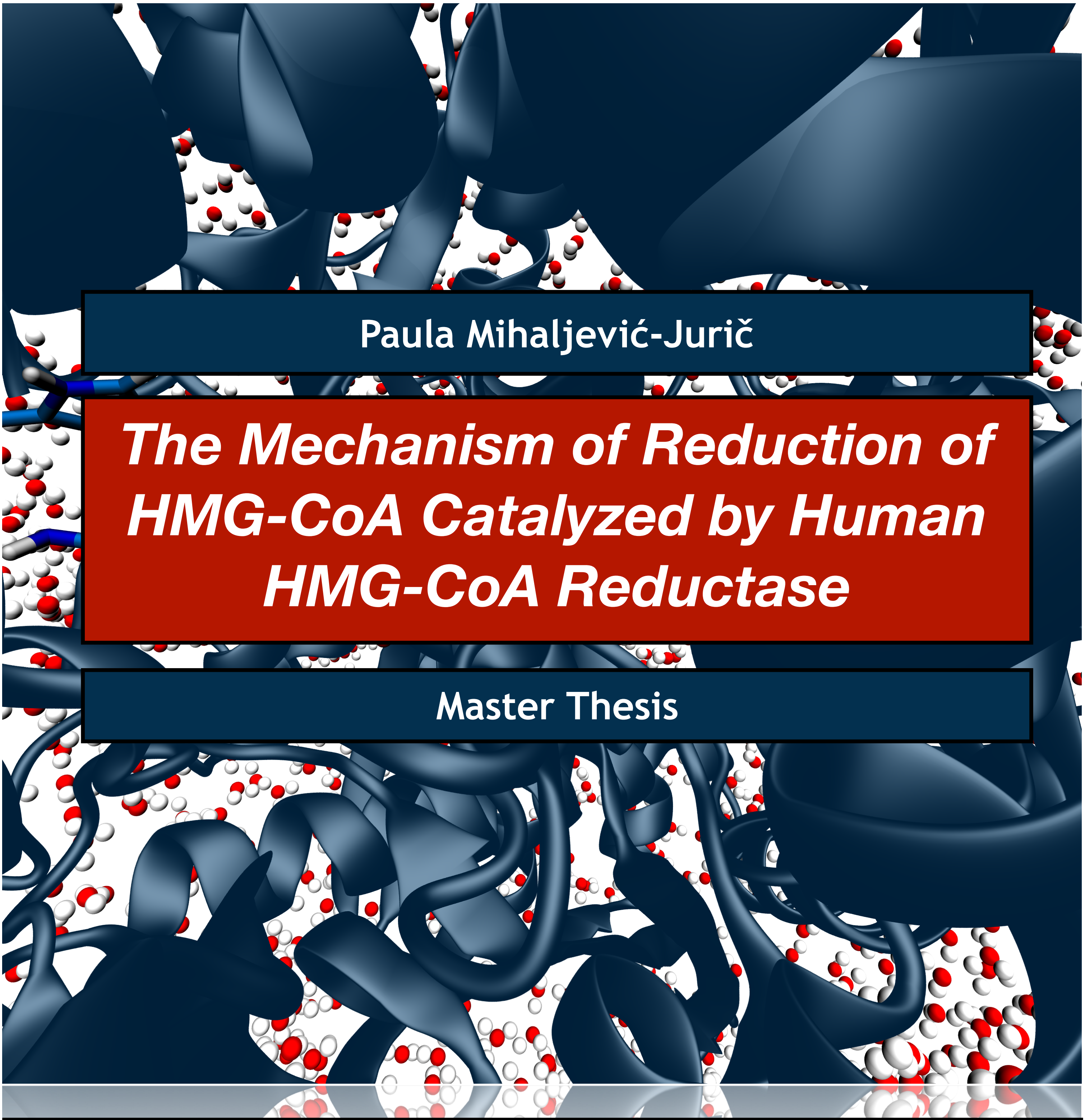

Paula Mihaljević-Jurič

The Mechanism of Reduction of HMG-CoA Catalyzed by Human HMG-CoA Reductase

Master Thesis

Mentor: Assistant Professor Martina Medvidović-Kosanović
Co-mentor: Research Assistant Sergio F. Sousa

Osijek, 2018.

For Adelina

Acknowledgements

Firstly, I want to express my greatest appreciation to my mentors prof. Sergio F. Sousa and prof. Martina Medvidović-Kosanović, as well as to prof. Pedro A. Fernandes who invited me to the University of Porto. They all guided me through this eight-months process from which I learned so much. I can never thank them enough.

Then, I want to thank my wonderful parents, Ljiljana and Drago, who gave me nothing but love and support in both my life and education. I hope all children in the world have amazing parents like them.

I want to thank all people in Computational Chemistry group at the University of Porto, for talks about science and all the help through these last months. Mainly, I want to express my gratitude to Henrique and André who helped me with their insights and many technical issues I had.

Without meeting prof. Safiye Erdem, who is a far best professor I ever had, in Istanbul, I would never have the opportunity to explore the amazing world of Computational Chemistry.

Also, I want to thank all of my people and my dear friends for their love and support.

TEMELJNA DOKUMENTACIJSKA KARTICA Diplomski rad

Sveučilište Josipa Jurja Strossmayera u Osijeku
Odjel za kemiju
Diplomski studij kemije
Znanstveno područje: Prirodne znanosti
Znanstveno polje: Kemija

Mehanizam redukcije HMG-CoA katalizirane ljudskom HMG-CoA reduktazom

Paula Mihaljević-Jurič

Rad je izrađen na: Sveučilištu u Portu, Odjel za kemiju i biokemkiju
Mentor: PhD Martina Medvidović-Kosanović, PhD Sergio F. Sousa

Sažetak

Redukcijski mehanizam HMG-CoA katalizirane ljudskom HMG-CoA reduktazom ispitivan je QM/MM (ONIOM) metodom. Sustav je podijeljen na dva dijela gdje se aktivno mjesto tretiralo kvantnom mehanikom (DFT, B3LYP), a ostatak enzima s klasičnim metodama molekularne mehanike. Istraživana su tri različita modela drugog hidridnog prijelaza mehanizma s različitim protonacijskim stanjima katalitičkih amino kiselinskih ostataka. U aktivnom mjestu nalazio se NADPH kofaktor, mevaldehid substrat te glutamat, lizin, aspartat i histidin (Glu98, Lys639, Asp715 i His405). Metodom molekularne dinamike (MD) dobila se najpovoljnija konformacija početne kristalografske strukture, koja se koristila u svim daljnjim simulacijama. U prvom modelu glutamta i aspartat su bili deprotonirani, lizin je bio protoniran, a histidin dvostruko protoniran, dok je u drugom modelu histidin bio protoniran, a u trećem modelu lizin deprotoniran.

Diplomski rad obuhvaća: 105 stranica, 49 slika, 5 tablica, 115 literaturnih navoda i 5 priloga.
Jezik izvornika: engleski
Ključne riječi: B3LYP, DFT, HMG-CoA, HMG-CoA reduktaza, ljudska HMGR, ONIOM, QM/MM
Rad prihvaćen: 27. lipnja 2018
Stručno povjerenstvo za ocjenu:
1. doc. dr. sc. Elvira Kovač-Andrić
2. doc. dr. sc. Martina Medvidović-Kosanović
3. doc. dr. sc. Mirela Samardžić

Rad je pohranjen: Knjižnica Odjela za kemiju, Franje Kuhača 20, Osijek

University of Osijek
Department of Chemistry

University of Porto
FCUP (Department of Chemistry and Biochemistry)

BASIC DOCUMENTATION CARD **Master Thesis**

Josip Juraj Strossmayer University of Osijek
Department of Chemistry
Graduate Study of Chemistry
Scientific Area: Natural Sciences
Scientific Field: Chemistry

The Mechanism of Reduction of HMG-CoA Catalyzed by Human HMG-CoA Reductase

Paula Mihaljević-Jurič

Thesis completed at: University of Porto, Department of Chemistry and Biochemistry

Supervisor: Martina Medvidović-Kosanović, Assistant Professor; Sergio F. Sousa, Assistant Researcher

Abstract

Reduction mechanism of HMG-CoA catalysed by human HMG-CoA reductase has been studied with the QM/MM (ONIOM) method. The system has been partitioned in two parts where the active site was treated with quantum mechanics (DFT, B3LYP) and the rest of the enzyme with classical methods of molecular mechanics. The second hydride transfer of the catalytic mechanism have been studied through three different models with different protonation states of the catalytic residues. In the active site NADPH cofactor, mevaldehyde substrate, glutamate, lysine, aspartate and histidine (Glu559, Lys639, Asp715 i His405) were placed. Through molecular dynamics simulations the most favourable conformation of the initial crystallographic structure was obtained and used throughout all the later simulations. In the first model, glutamate and aspartame were deprotonated, lysin was protonated and histidine was double-protonated, whereas in the second model, histidine was protonated, and in third model lysine was deprotonated.

Thesis includes: 105 pages, 49 figures, 5 tables, 115 references, 5 appendices
Original in: English
Keywords: B3LYP, DFT, HMG-CoA, HMG-CoA reductase, human HMGR, ONIOM, QM/MM
Thesis accepted: 27th June 2018
Reviewers:
1. doc. dr. sc. Elvira Kovač-Andrić
2. doc. dr. sc. Martina Medvidović-Kosanović
3. doc. dr. sc. Mirela Samardžić

Thesis deposited in: Library of Department of Chemistry, Franje Kuhača 20, Osijek

Contents

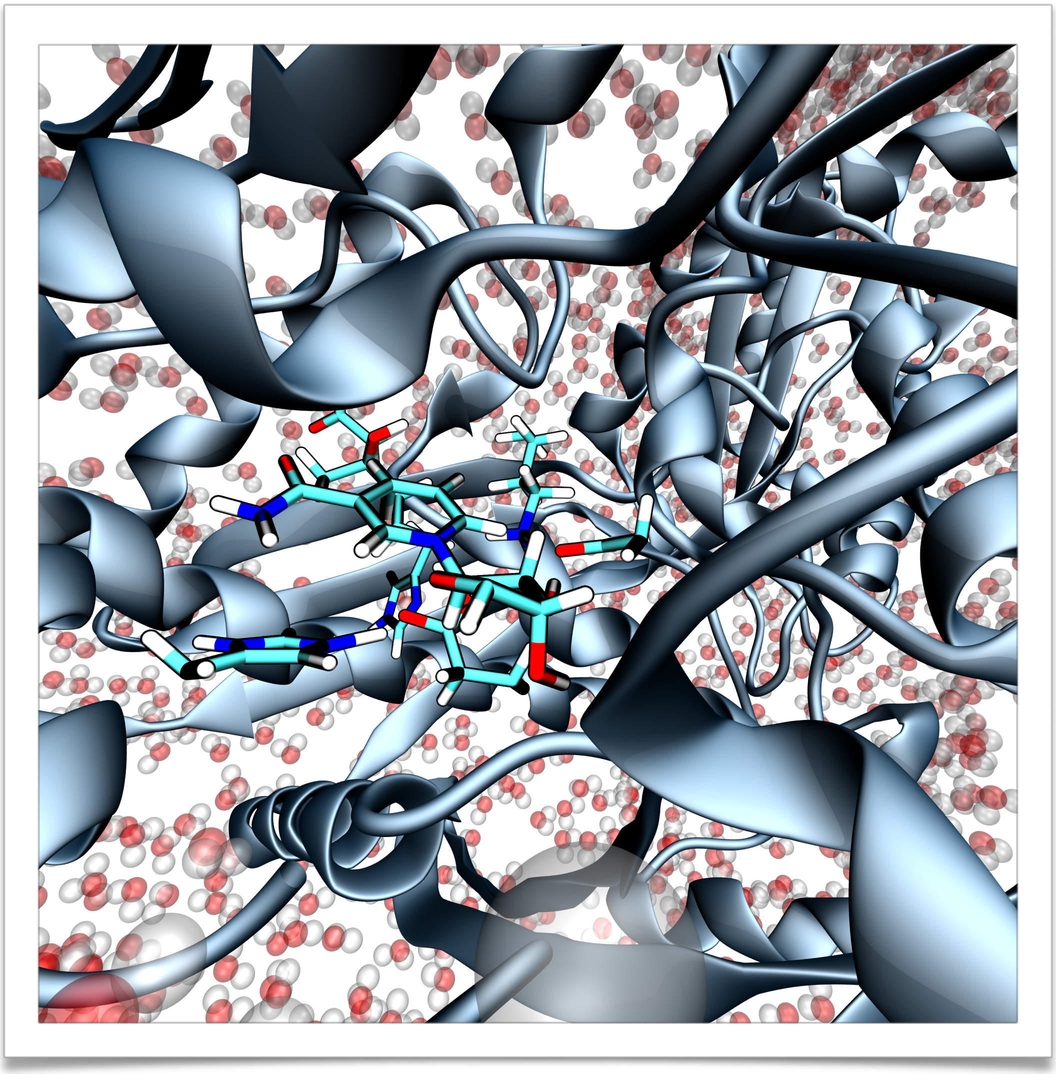

Chapter 1 - The HMG-CoA Reductase Riddle

1. Introduction

The *β*-hydroxy-*β*-methylglutaryl-CoA reductase, or simply HMG-CoA reductase (HMGCR), is one of the most regulated enzymes in the human body **[1]**, which catalyzes the four-electron reduction of *β*-hydroxy-*β*-methylglutaryl-CoA , HMG-CoA (**Figure 1.1**), to mevalonate. **[2]** The importance of the enzyme lies in the impact of statins, cholesterol-lowering drugs and HMG-CoA reductase inhibitors, on human health. Recently, HMGCR has been recognised as a target for the antimicrobial drugs. [Haines *] Furthermore, the reaction mechanism itself has been studied for decades using X-ray crystallography, but there are only a few computational studies that tested all the hypothesis of this complex reaction. **[3,4]** The reaction itself involves multiple chemical steps with large-scale to coupled domain motions of the homodimeric enzyme. The first mechanism proposals were based on the kinetic and labelling experiments with analogy to the known dehydrogenase mechanisms. [Haines *] Correspondingly, to synthesise better drugs, it is important to understand how the reaction mechanism is occurring and why in that particular manner. The complete mevalonate pathway is represented in the **Figure 1.2**.

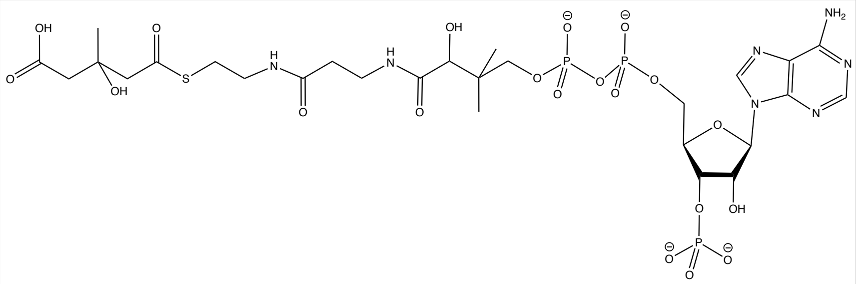

Figure 1.1 The structure of HMG-CoA.

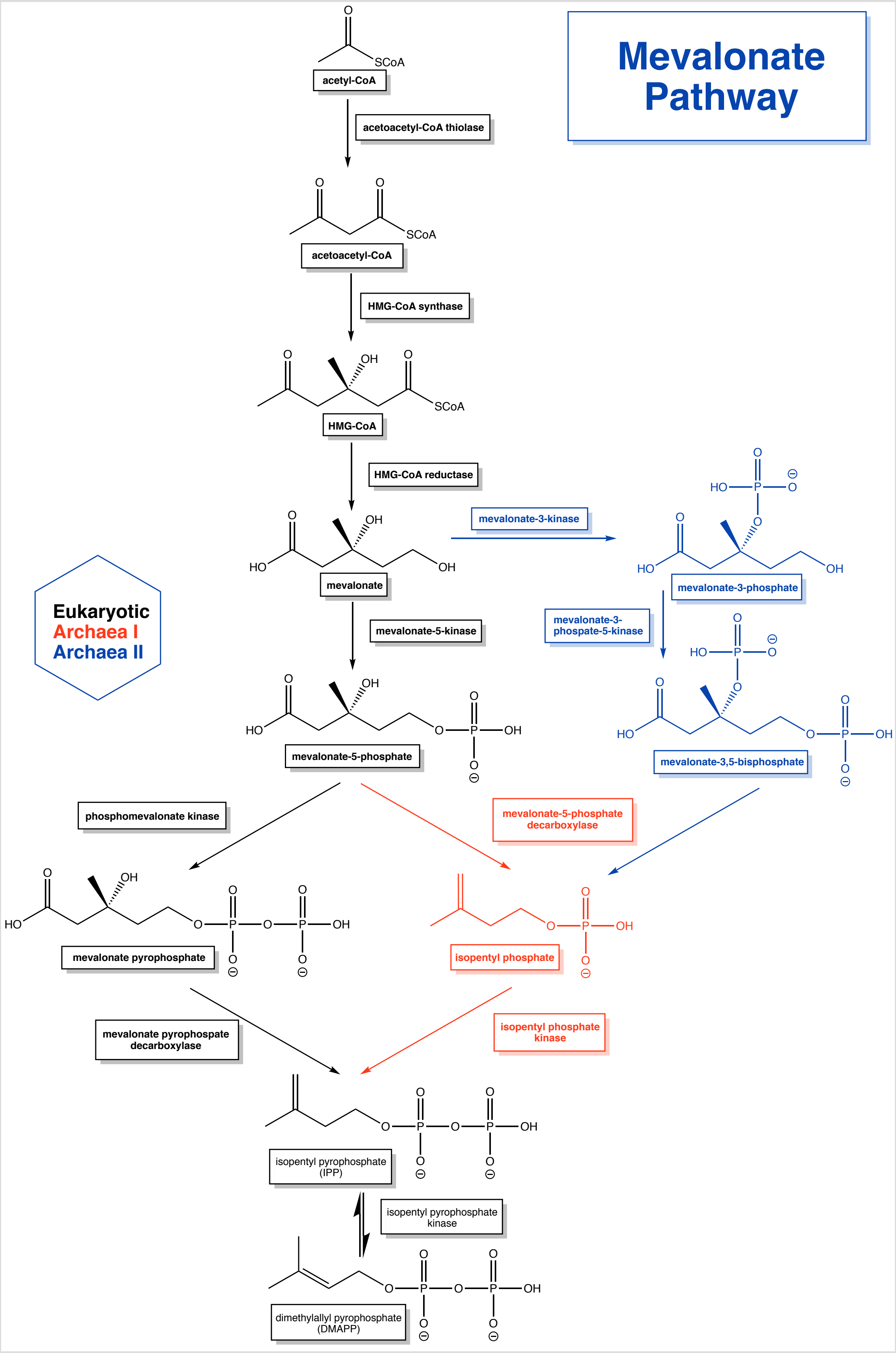

Figure 1.2 Mevalonate pathway / cholesterol biosinthesys.

1.1 The Importance of HMG-CoA Reductase

HMG-CoA reductase is an oxidoreductase (**Figure 1.3**) that catalyses the interconversion of HMG-CoA and mevalonate. **[3]** In fact, it plays an important role in a biosynthesis of lipids like cholesterol, as well as some other compounds as steroids (**Figure 1.4 b**) and isoprenoids. **[5,6]** Cholesterol (**Figure 1.4 a**) is always publicised in a bad manner due to its correlation to many cardiovascular diseases. However, cholesterol is quite an important compound in our body, since it is a component of cellular membranes and a precursor of steroid hormones and bile acids. Although cholesterol is a complex compound, all of its atoms come from one precursor, acetate. The so-called isoprene units are essential intermediates in the pathway from acetate to cholesterol, and also precursors to many other natural lipids. **[5]** Isoprenoids are compounds that are involved in sterol synthesis and growth control. **[2]**

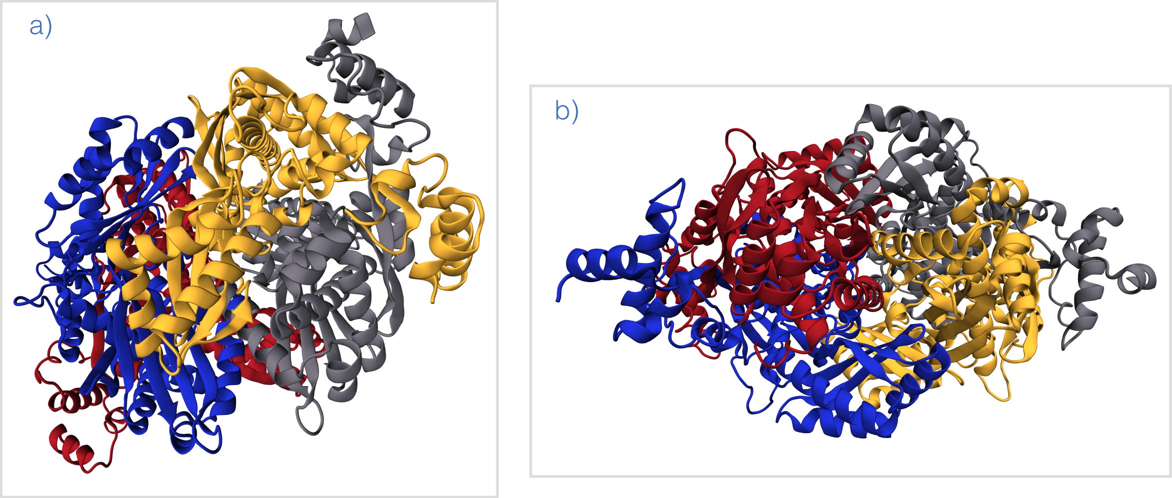

Figure 1.3 Graphical representation of HMG-CoA reductase in *New Cartoon* (PDB:1DQA) using Visual Molecular Dynamics software (VMD).

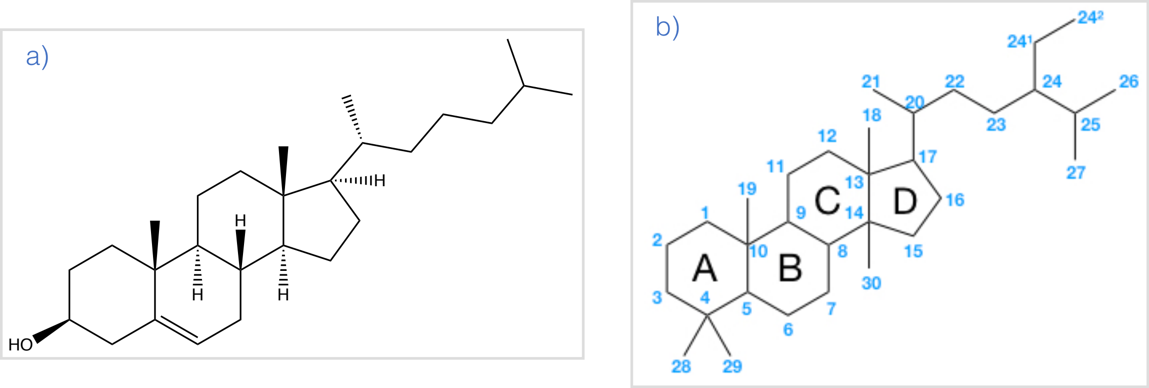

Figure 1.4 (a) Structure of cholesterol. (b) Structure of steroid.

HMG-CoA reductase is involved in a mevalonate synthesis starting from acetate compound, which is the first stage in cholesterol biosynthesis. Two molecules of acetyl-CoA condense to form acetoacetyl-CoA in a reaction catalysed by thiolaze, which then condenses with a third molecule of acetyl-CoA to form *ß*-hydroxy-*ß*-methylglutaryl-CoA (HMG-CoA) in a reaction catalysed by HMG-CoA synthase. Reduction of HMG-CoA to mevalonate, the third reaction, is the rate-limiting step at the expense of two molecules of NADPH (**Figure 1.5**). In addition, HMG-CoA reductase is an integral membrane protein of the smooth endoplasmic reticulum, a regulative point in a cholesterol biosynthesis, and it totally depends on NAD(P)H. **[2,3]**

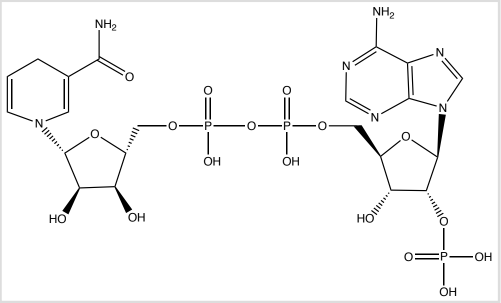

Figure 1.5 The structure of NADPH.

1.2 The HMG-CoA Reductase Structure

As seen in **Figure 1.6**, HMG-CoA reductase is a tetramer with chains intercepting each other as „dimer of dimers“, with an active site on each chain. **[7]** As protein crystallography developed more and more, it gave better and clearer images of HMG-CoA reductase crystal structure with lysine in its active site. With the development of the bioinformatics and molecular biology, which enabled advanced mutagenesis experiments and sequence analysis, glutamate, histidine and aspartate residues were identified as catalytically relevant. Most mechanisms that were based on crystallography gave us detailed structure of the enzyme, as well as its substrate and cofactor, but there is no information about thermodynamics and dynamics of the system. **[8]**

Furthermore, there are two evolutionarily divergent classes of HMG-CoA reductases divided in two groups - eukaryotes (Class I) and prokaryotes (Class II). Not that long ago, all HMGR enzymes belonged to the same group of Class I, because of inabillity to properly purify and express the enzyme due to their membrane-bound nature. The Class I HMG-CoA reductases are mainly membrane-bound, and consist of a transmembrane and a catalytic domain. **[8]** In more details, it consists of a carboxy-terminal catalytic domain and an amino-terminal membrane anchor domain, which are highly and poorly conserved, respectively. **[9]** As to Class II HMGR enzymes, they are all cytostolic and lack membrane anchor domain. **[8,9]**

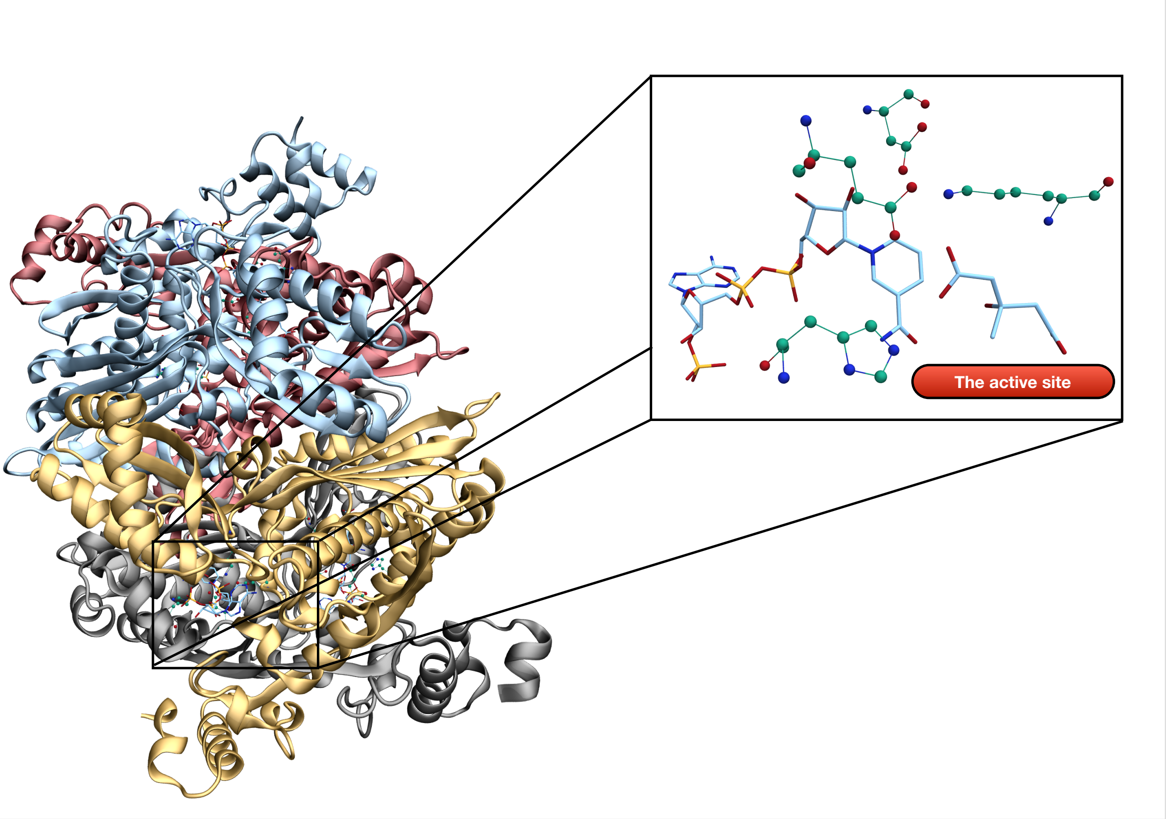

1.6 Graphical representation of the HMGR tetramer with chains A, B C and D in *NewCartoon* and one active site in *Licorice* using *Visual Molecular Dynamics* (VMD) software.

The HMG-binding pocket is characterised by a “cis loop” (residues 692-694). The COOH-terminal residues of the HMGCR are known to be mobile parts of the protein. In the structures of a bacterial form of HMGCR (*Pseudomonas mevalonii*) there is a larger COOH-terminal domain which is not present in the human enzyme. The flexibility of the COOH-terminal domain is vastly exploited by statins for binding site and inhibition. Regarding the interactions formed between the HMG-moieties and residues in the “cis loop” (Ser684, Asp690, Lys691 and Lys692), they are mostly polar. Also, Lys691 is involved in a hydrogen-bonding network with Glu559 and Asp767, as well as the hydroxyl group of statins in the inhibition. It is also stated that the COOH-terminal group of HMG-moiety forms a salt bridge with Lys735. Identical interactions have been observed between the protein and HMG, as well as the reaction product mevalonate. However, as mevalonate product is released from the active site it is highly likely that not all of the interactions with the protein are stabilising. Thus, the observations suggest that the hydrophobic groups of the inhibitors are mainly responsible for the nanomolar K_i values. Hydrophobic side chains of the residues Leu562, Val683, Leu853, Ala856 and Leu857 are involved in van der Waals interactions with the statins. **[10]**

1.2.1 The Crystallographic Structure of PmHMGR

The first crystallographic structure of the obtained HMGR was the one from PmHMGR (Pseudomonas mevalonii). That confirmed that the large domain is centred on a hydrophobic α-helix of 24 residues surrounded by three mixed α/βwalls. The binding pocket is well-defined for HMG moiety and CoA part is positioned in a shallow surface groove with few hydrogen bonds with the enzyme. The CoA adenine ring is pushed down by an arginine, whereas phosphate groups interact with enzyme through hydrogen bonds. **[11]**

The small domain binds NADH with a dinucleotide fold of a four-strand anti-parallel β sheet and two crossover helices one side. The loop is conserved and contains DAMG sequence that connects the third strand and the second helix. Additionally, this is analogous to the G-rich loop in the dinucleotide domain of binding. Moreover, the cofactor is stretched out on the enzyme with the inserted nicotinamide ring parallel to the HMG moiety of the substrate in the active site. The position of the cofactor is rather unique as it is parallel to the HMG moiety, which might suggest that it has to be exchanged surging the reaction and that is why it is not placed under or over the substrate. **[8]**

It was discovered that the enzyme had an activity in the crystal form, while trying to solve the ternary complex of the crystallographic structure, which was nonproductive and an oxidase form of the cofactor. This study showed an electron density of the flap domain (377-428 residues) over the active site in three α-helices connected with short loops. Additionally, the first helix is connected to the central helix of the large domain by a hinge region that probably plays a role in a substrate binding. The flap domain itself interacts with the first helix and the small domain of the second chain, bound substrate and cofactor. When the flap domain reorders, it aligns the hydrophobic residues that form a pocket in the helix and provides protection of the active site from the solvent. In addition, the moment the flap domain closes, it brings the His381 in the active site close to the sulphur atom of the HMG-CoA. **[12,13]**

1.2.2 The Crystal Structure of The Human HMGR

Istvan et al. studied the human HMGR and observed similar motifs and conserved catalytic residues in the active site. **[2]** This enzyme forms a tearer in two dimeric structures that resemble those in the *PmHMGR* structure. This study noted a very different secondary structure and the 'cis-loop' that positions the lysine residue (Lys735). **[14, 2]**

1.3 Catalytic Mechanism

The catalytic mechanism of HMG-CoA reductase is a rare example of an oxidoreductase (four electrons in total) that uses two molecules of cofactor NADP(H). The reaction itself is the irreversible conversion of (S)-HMG-CoA to (R)-mevalonate through two intermediates, mevaldyl-CoA and mevaldehyde. There are two hydride transfers, a cofactor exchange step and a hemitioacetal decomposition step (**Figure 1.7**). However, the mevaldehyde (aldehyde intermediate) has never been experimentally detected. Thus, the hypothesis of a hemithioacetal as an intermediate was developed **[15-19]**

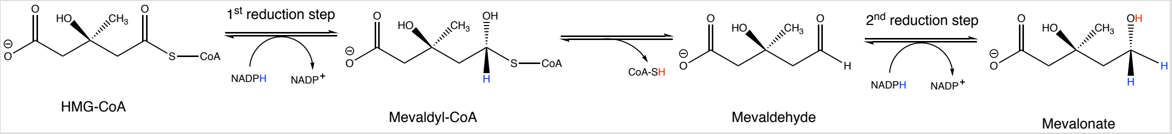

Figure 1.7 General accepted reaction catalysed by HMG-CoA reductase.

Moreover, this theory has been supported by a crystal structure for a tetrahedral hemithioacetal analogue in the active site. The free energy calculations were performed on the ternary complexes, as well. **[3, 11]** Therefore, a problem arises as the hemithioacetal is presumably unreactive towards NAD(P)H, and the question remains - at which point does aldehyde form in this reaction? **[8]**

The second complication of this mechanism arises from the cofactor exchange. Furthermore, in *PmHMGR* crystallographic structure with one or no ligands, there is no C-terminal 50 residues known as the flap domain. **[20]**

But when a crystallographic structure was obtained with two ligands present, the flap domain has been observed over the active site in a three α-helix bundle in contact with substrate and cofactor (**Figure 1.8**). Therefore, flap domain movements are involved in binding of a substrate and cofactor. Some motions of the flap domain occur between the hydride transfer steps to support the process of cofactor exchange. This suggests that flap domain motions have an impact on formation of aldehyde intermediate. **[8]**

Moreover, the crystallographic structure of the human HMGR is in conflict with previous mechanism as there are some differences between two classes of HMGRs. **[21,15 , 22, 23, 24, 12, 11, 25, 14, 26, 2]**

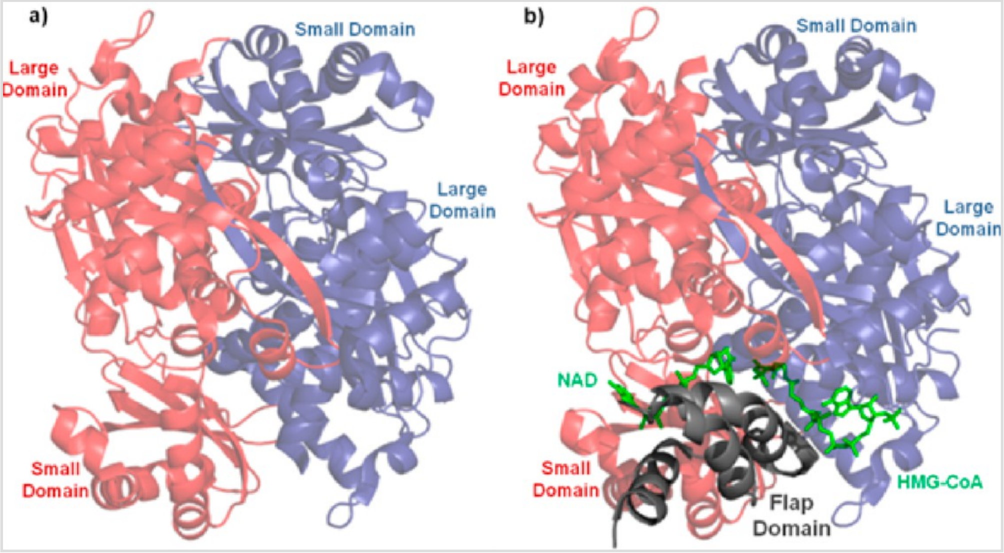

Figure 1.8 Graphical representation of crystallographic structure of HMGCR showing large, small and flap domain.

1.3.1 The PmHMGR mechanism

Before PmHMGR discovery, there was only one class of these enzymes, Class I. They were extremely hard to study as they are membrane bound and most research was focused on absence of aldehyde intermediate in the yeast HMGR. Thus, a hypothesis of hemithioacetal emerged. *Qureshi et al.* described it as a hydride transfer mechanism and its stereoselectivity, as well as hemithioacetal breakdown, which implied acidic and basic residues. Veloso et al proposed a mechanism using pH dependent kinetic analysis to determine acidic residues and a histidine in cationic form as the catalytic residues in the active site. Additionally, the reductions steps were studied as the classic dehydrogenase as shown in **Figure 1.9**. Because of the complicated kinetics, it was not possible to determine the rate limiting step and the ligand binding was again uncertain. Also, they stated that the protonation of the histidine has an effect on redox form of the cofactor. **[27]**

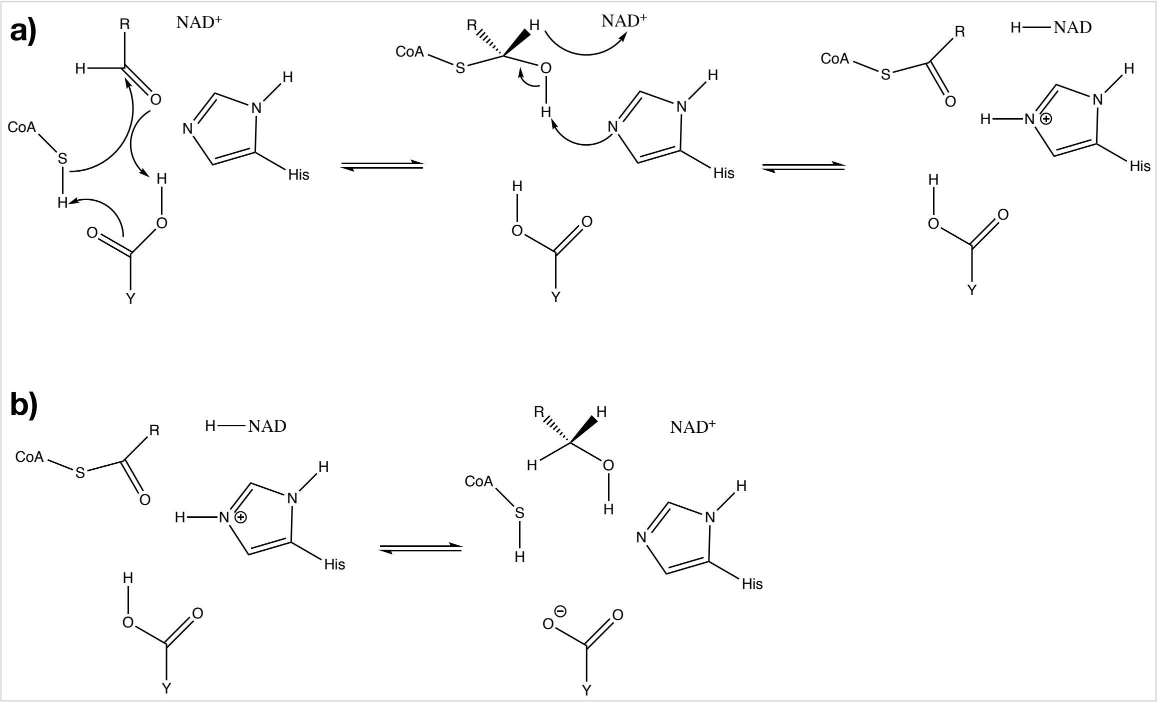

Figure 1.9 Reduction mechanism proposed by *Veloso et al. [27]*

Pseudomonas mevalonii are organisms that can live on mevalonate as a source of carbon. Thus, it was discovered that there are large quantities of *PmHMGR* for mevalonate catabolism, which is the reverse mevalonate pathway. **[28]**

It has been shown that some HMGRs of the Class I are inactivated through modification of cysteine by sulfhydryl agents. It was thought that cysteine has an important role in the binding. Therefore, they mutated two cysteine to alanine residues, which showed that mutated groups catalysed the reactions with the same efficiency as the wilde-type enzyme and the previous proposal was revised. **[23]**

Through protein sequence alignment of the HMGRs, conserved acidic residues and histidine were observed. It was shown that for *PmHMGR* activity, Glu83 and His381 were essential. After which, for mammalian enzyme an Asp766 was identified in the Syrian hamster HMGR, as it was confirmed that the enzyme was inactivated after mutation. **[29]** So, a new mechanism was proposed as shown in **Figure 1.10**. Moreover, the glutamate and histidine mutants were capable of catalysing one or more half reactions, but aspartate mutant had no activity, so the new proposal was formed with the aspartate as the catalytic residue. **[13]** In contrast to that, studies on the bacterial HMGR concluded that the catalytic residue in this mechanism is Glu83, which is more consistent with the studies in general.

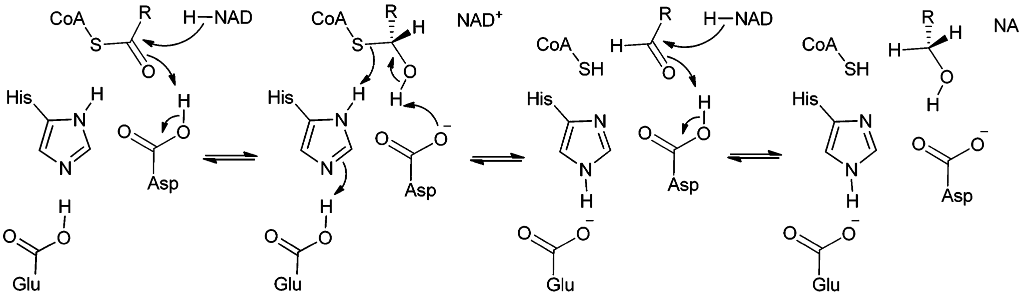

Figure 1.10 Reduction mechanism proposed by *Frimpong et al. [13]*

Through the *PmHMGR* structures, positions of the conserved residues Asp283, Lys267 and Asn271 were observed in the active site. The lysine is centrally located in the near proximity to the Glu83 and Asp283, which were later confirmed as important in catalysis. Additionally, the protonated Lys267 was bonded to the third carbonyl of the substrate, thus *Tabernero et al.* proposed a new mechanism described in **Figure 1.11**.

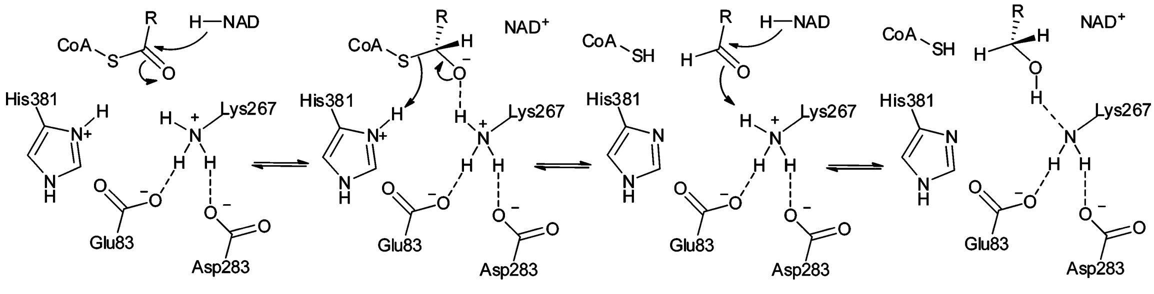

Figure 1.11 Reduction mechanism proposed by *Tabernero et al. [12]*

It is stated that the lysine polarises the carbonyl of the substrate in each hydride transfer. Moreover, it is general acid for protonation of the mevalonate in the end of the reaction mechanism. Aspartate and and some other residues interact with the lysine through secondary hydrogen bonds. When Glu83 is close, it assists mevaldyl-CoA decomposition and subsequently passes the proton to the lysine. Also, His381 protonates the thiolate anion of the CoA after the first hydride transfer. **[12]**

1.3.2 The Human HMGR Mechanism

A study of *Istvan et al.* and their discoveries led to a new proposal, **Figure 1.12**, where the acidic residue Glu559 (analogous to Glu83) is protonated. Moreover, a negatively charged aspartate, Asp767 (analogous to Asp283) affects its pK_a. Thus, the Glu559 and Lys735 form an oxyanion hole and stabilise the intermediates after the hydride transfer. This also means that glutamate is general acid/base for the reaction, and not lysine as previously mention. Asp767 supports the position of Lys691, which controls the protonation state of the glutamate, whereas the His866 has the same function as previously described. The only difference between **Figure 8 and 9** is protonation state of the glutamate, which cannot be confirmed through crystallographic structures. *Istvan et al.* stated that different mechanisms could arise from different classes of the two studied enzymes. **[26]**

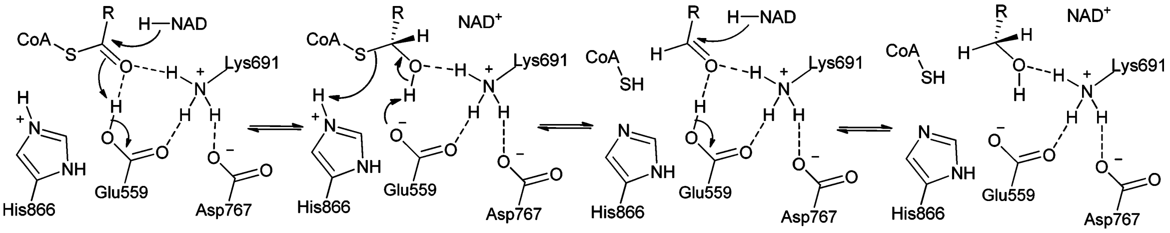

Figure 1.12 Reduction mechanism proposed by *Istvan et al. [26]*

Haines et al. conducted a computational study **[3]** that was focused on the protonation state of the glutamate in the PmHMGR mechanism, as direct calculation of the pK_a of that residue in this environment is not really possible. This study showed that in terms of energy barriers for both protonation states of the glutamate, the first hydride transfer is the rate limiting one. Moreover, when

Glu83 is deprotonated, the barriers are 10 kcal/mol higher than when its protonated. Also, it showed that Glu83 is an acid/base for this reaction, and that Lys267 cannot perform this function in both cases. It is also stated that deprotonated glutamate cannot stabilise the hemithioacetal intermediate in *PmHMGR* mechanism, where the carbon-sulphur bond of the hemithioacetal extends and dissociates and that is not consistent with the experimental data. **[3, 8, 11, 13]** This would confirm that there is no general mechanism for all HMGRs.

1.3.3 Intermediates and Cofactors

Mevaldyl-CoA active substrate was generated in situ and it is observed that it converts to a product in the presence of cofactor NADPH. **[21, 19, 8]** Initially, dithio-HMG-CoA was thought to be a competitive inhibitor of HMGR **[30]**, but in the complex with *PmHMGR* and NADH it was discovered that it is rather slow substrate. A study shown that electron density for a tetrahedral dithiohemiacetal (a hemithioacetal intermediate analogue) in the active site and it forms from the natural substrate. Moreover, a network of hydrogen bonds with the flap domain residues, was identified, as well as the conserved catalytic residue Ser85 and the amide group close to the HMG-CoA sulphur. **[11]**

The flap domain and closing patterns arise from changes in the active site and hydrogen bonds of the catalytic residues. An extensive study concluded that a major distortion of the substrate is structurally important for the reaction, where a substrate has to flip its ring for 180° through interactions with Ser85 and His381. However, no study detected a mevaldehyde intermediate, which still remains ambiguous. **[15, 16, 17, 30]** The problem with aldehyde intermediate arises from the fact that in the solutions its equilibration is known to be rapid so, it is not strange to expect appropriate amount of it in this reaction. Furthermore, it is unlikely that mevaldehyde would stay bounded to the enzyme due to its K_m values that are in μM-mM range, which implies a dissociation process after solvent exposure. Also, it is possible that mevaldehyde is somehow protected from the solvent as it is highly hydrated. **[8,27]**

In terms of cofactor exchange, it can reasonably occur before or after decomposition of the hemithioacetal. Thus, if the exchange happens after decomposition, aldehyde would dissociate and be able to be detected. However, if the exchange happens before, an aldehyde would not be exposed to solvent and dissociate. This would confirm the observation stated before. Moreover, it indicates that the decomposition is slower than the exchange of the cofactor. Some computational studies support thermodynamical preference of mevaldyl-CoA and support this theory, as well as the eclectrostatical interaction between oxidase cofactor and deprotonated glutamate that slow the process of decomposition. **[3]**

Haines et al. proposed a revised mechanism in **Figure 1.13**, where the thioester of HMG-CoA is reduced and the oxyanion is stabilised through Glu83 and hydrogen bond with Lys267. When the flap domain opens, the oxidised cofactor dissociates, whereas after the binding of the reduced cofactor, flap domain reorders. Besides, the Glu83 assists decomposition of the hemithioacetal supported with base to produce mevaldehyde and the CoA thiolate anion. Afterwards, the thiolate anion is protonated by cationic His381. It is proposed that CoASH is held in the active site with the assistance of Ser85 and His381, while mevaldehyde is reduced to mevalonate, and the oxyanion is stabilised by Glu83 and hydrogen bond with Lys267. So, after the flap domain opens, mevalonate, CoASH and NAD^+ are released. Although, the rate-limiting step has not been determined experimentally, it has been computationally determined that for the first hydride transfer the energy barrier is 21.8 kcal/mol, which is consistent with the rate constant of 1 s^{-1}/min, which has been experimentally determined. **[3, 8]**

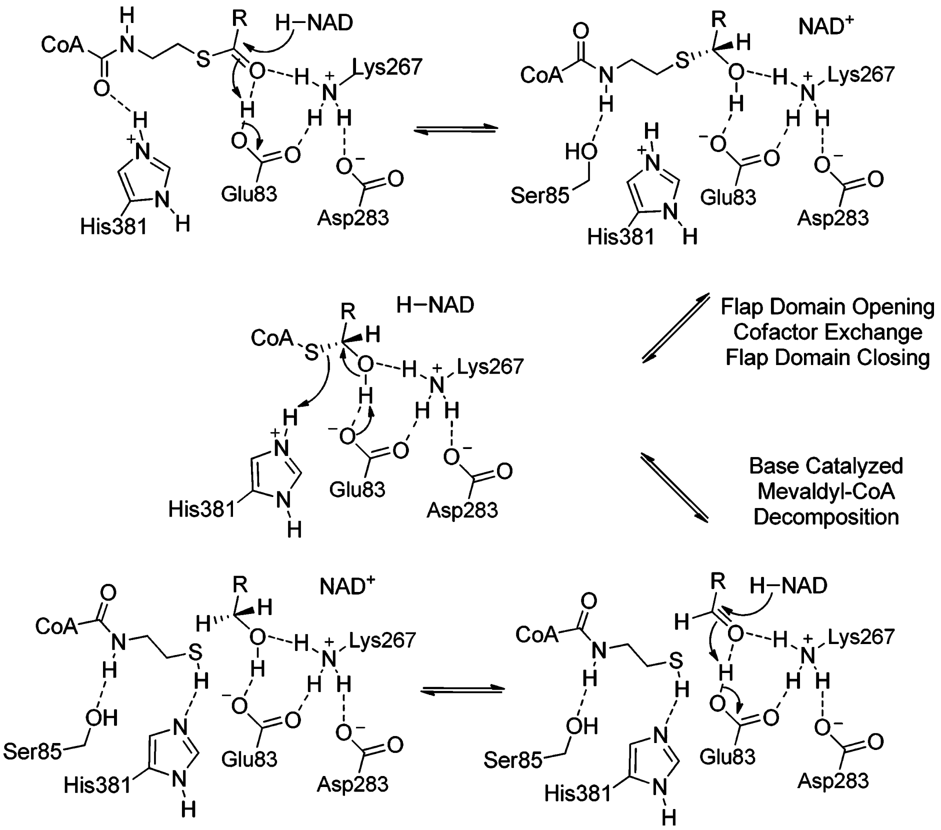

Figure 1.13 Revised mechanism proposed by *Haines et al.* [3]

1.4 The reason to study HMGR

Oliveira et al. conducted a study of the first and the rate-limiting step of reduction mechanism of HMG-CoA. They studied three different systems with different protonation states of catalytic residues. Firstly, they studied the so-called “Standard system”, where Glu559, His752 and Asp767 were deprotonated. Secondly, there was a “Glu559H system”, where Glu559 was protonated and other residues were deprotonated, and lastly, “His752H system”, with protonated His752. Furthermore, the last protonation state, the one of His752, was not derived from the literature, but from the study and observations itself. **[31]**

1.4.1 Standard System

The average distance of NADPH hydride to the HMG-CoA acceptor, as well as overall RMSd and active site average RMSd, were similar to the crystallographic structure. The active site of the minimised system gave the lowest active site RMSd of all three systems (RMSd=1.29 Å), and the close distance between Asp767 and Glu559 was 3.67 Å. Moreover, this system showed the shortest distance between NADPH hydride and the substrate. **[31]** Relatively short distance between glutamate and aspartate was noticed in the crystallographic structures (3.6 Å), and it is considered to raise the pKa of the glutamic side chain and protonated Glu559. **[2]**

Their results have shown that in the electrostatic context of the HMGCR active site, the interactions between Glu559 and His866, as well as the interactions between the 2'-hydroxyl group of the NADPH ribose and Asp767, allowed the extremely close co-existence of two charged carboxyl side-chains next to each other. **[31]** Charged His866 was suggested as the general acid for the CoA anion protonation after the decomposition of the intermediate in the form of hemithioacetal. **[2,10,11]** Interestingly, the final results shown that low activation free energy was not found for this system (**Figure 1.14**). **[31]** The system included different pathways, which were studied, like direct formation of the mevaldehyde intermediate and CoA-S$^-$ without passing through mevaldyl-CoA.

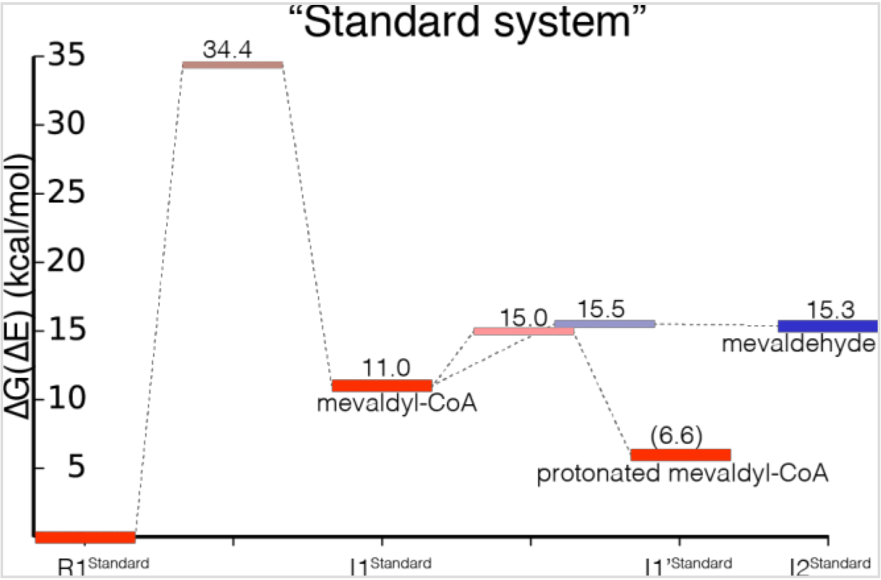

Figure 1.14 Free energy profile of the first hydride transfer in the "Standard system". [31]

1.4.2 His752H System

As mentioned before, this system was studied purely because of the observed interactions during the *Molecular Dynamics* simulations (MD), where oxygen of HMG-CoA came closer to His752 therefore, between Lys691 and His752. Thus, a theory of possible oxyanion hole for stabilization of the negative charge in the thioester oxygen was developed. **[31]** *Haines et al.* stated that there are several residues in the active site which are ionizable (His866, Glu559, Asp767 and Lys691), so there are various proposed mechanisms based on different protonation states of the residues, as well as their roles as acids or bases in the reaction. **[3, 8]** Indeed, the 6.2 pKa of the histidine made this hypothesis possible. However, after the minimization His752 was hydrogen bonded with Glu559, and not with the thioesther oxygen. In this case, the active site differentiate the most from the crystallographic structure (RMSd=1.48 Å), where His752 and Glu559 were hydrogen bonded, and Asn755 was pulled away. The lowest activation free energy was obtained only when using the X-ray conformation, where His752 and the carbonyl of the substrate polarised the C-O bond in HMG-CoA, thus the greater electrophilic nature of the substrate for easy hydride transfer. The role of the Lys691 in this system was probably to help His866 delocalise the charge of Glu559. **[31]**

1.4.3 Glu559H System

The system with the most favourable reaction energies and the most similar to the crystal structure (RMSD = 1.36 Å), was the one with the protonated Glu559, which is the opposite of the previous observed mechanism for prokaryotic HMGR. As previously described a protonated Glu559 reproduced an active site similar to the one from the crystal structure, whereas the deprotonated one was in repulsion with the Asp767 and the salt bridge with His866 that brought histidine deeper in the active site. **[8, 31]**

Moreover, the free activation energy of 17.8 kcal/mol was obtained with a slightly exothermic mevaldyl-CoA intermediate protonated by Lys691, which stabilised the negative charge at the thioester oxygen. The Glu559 was bonded to Asp767, thus the weaker interaction between the lysine and the aspartate.

Consequently, it lowered the pKa of Lys691 and allowed it to protonate the thioester. In contrast, *Haines et al.* suggested glutamate as the proton donor in the prokaryotic enzyme. It is also noted that the cofactor exchange happens prior to aldehyde formation, which is consistent with **[18, 32]**. They also stated that the second hydride transfer has a lower activation barrier then the first one by 2.9 kcal/mol. **[3, 8]**

In conclusion, there are several strong evidence that support the formation of the first intermediate protonated by the Lys691 with the protonated Glu559 - the lowest activation energy barrier, retained reversibility **[13]** and the stability of the intermediate. Additionally, the first hydride transfer is rate-limiting step due to lower electrophilicity of the thioester. Their proposal is supported by the mutagenesis study of *Bochar et al.* **[9]**, where they mutated three active site's lysins and caused major changes. They suggested that one of the lysine should be a general acid dragon the hydride transfer.

Therefore, we based our study and the chosen protonation states of the catalytic residues on the "Glu559H" system. The active site with the substrate mevaldehyde, cofactor NADPH and the catalytic residues Glu98, His405, Lys639 and His405 as shown in the first model we tested in **Figure 1.15**.

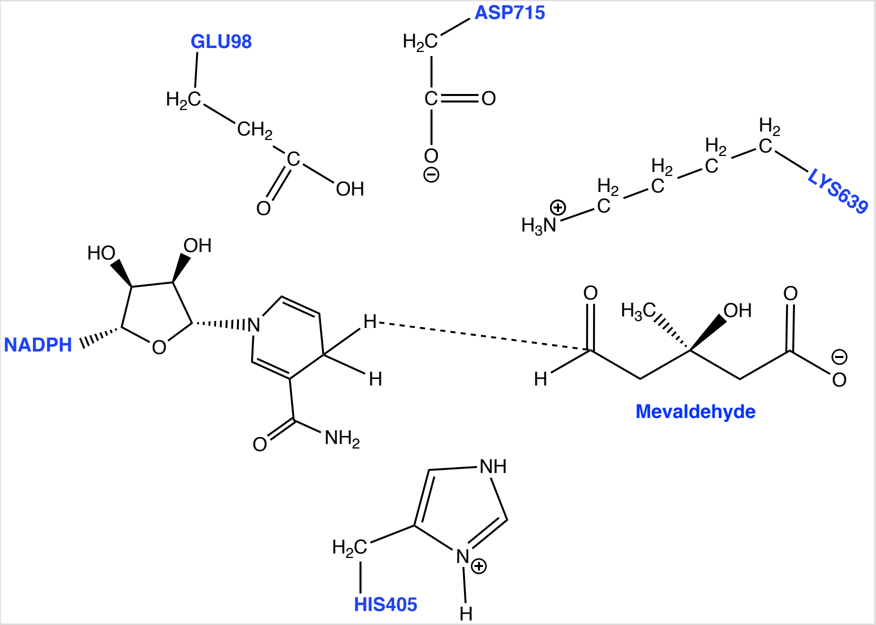

Figure 1.15 The active site with corresponding protonation states of the first studied model, where Glu98 and Lys639 were protonated, and His405 was double-protonated (cationic).

1.4.4 Statins

As noted before, the importance of this study lies in statins, which are mostly known as cholesterol-lowering drugs. **[8]** Statins block the rate-limiting step of cholesterol synthesis, where HMGCR is converted to mevalonate. **[33]**

Cardiovascular disease causes ~ 17 million deaths per year and is becoming a greater problem every day. Correspondingly, Statins inhibit some downstream products of mevalonate pathway and cause pleiotropic effects and therefore virtually modulate atherosclerosis mechanisms. Besides pleiotropic effects, statins also improve endothelial function which is one of the first steps in pathogenesis of atherosclerosis, where they inhibit prenylation of Racand Pho proteins **[34]** This leads to increased expression of endothelium-derived nitric oxide synthetase (eNOS) which leads to increased nitric oxide production and vasodilatation. Also, statins like atorvastatin and simvastatin have anti-inflammatory effects and it is showed that they reduce cholesterol levels, as well as inhibit inflammation. **[35]**

Moreover, they have immunomodulatory effects and anti-thrombin effects. Immunomodulatorty activity is observed in cardiac transplant rejection and some autoimmune disease like rheumatoid arthritis, ankylosing spondylitis, lupus, vasculitis and systemic sclerosis. **[36]** Statins successfully block clot formation and promote its destruction by decreasing plasminogen activator inhibitor 1 (PA1-1) levels and promoting the fibrinolytic enzyme plasminogen, thus they have anti-thrombotic effect. **[37, 38]**

Besides all previously mentioned benefits of statins, they can induce myopathy, diabetes and hemorrhagic stroke. Some studies have shown that they increase serum levels of liver enzymes and cause liver damage. Also, it is also possible that they cause memory loss. **[39]** Some evidence show that they may increase risk of breast cancer and all-site cancer **[40, 41]**, as well as neuropathy, sleep disturbances, suicidal behaviours and erectile dysfunction of aggression, but many of these side effects have never been confirmed due to lack of evidence.

The structures of some known statins are shown in the **Figure 1.16**.

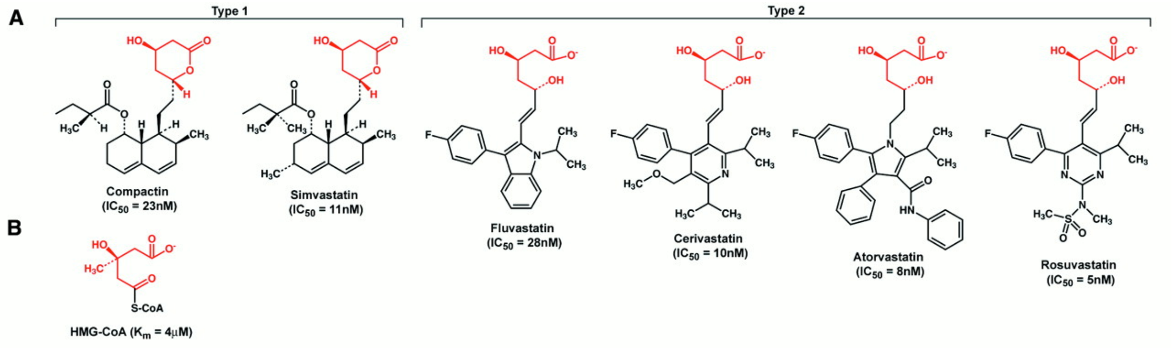

Figure 1.16 Structure of different statins.

Nevertheless, there are many open questions regarding HMGCR mechanism that have to be answered. In our work, we hope to answer and clarify the events that occur in the second hybrid transfer and how different pronation states of the catalytic residues affect the reaction mechanism.

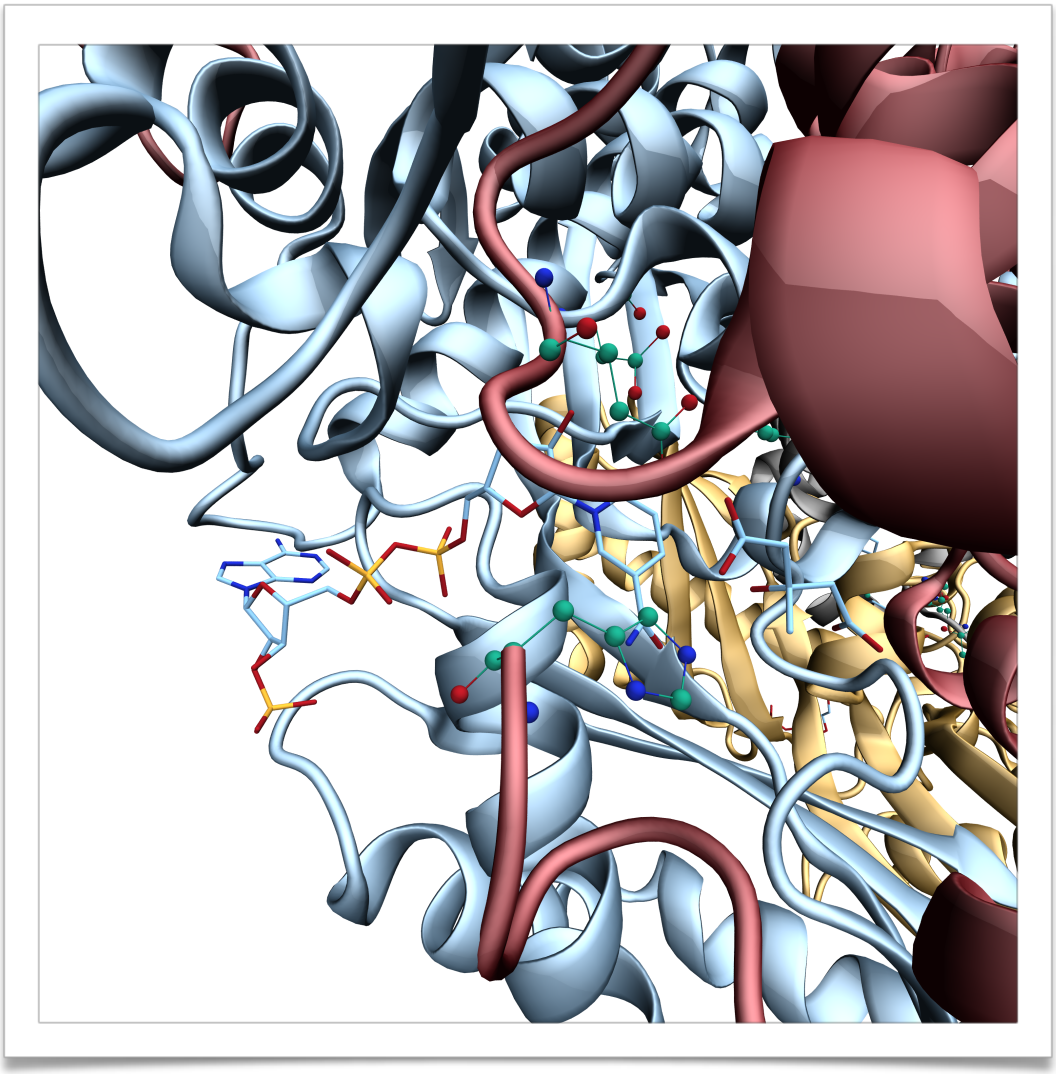

Chapter 2 - Methods

2. Introduction

With the development of computational methods, now it is possible to study unimaginable large systems like HMG-CoA reductase and their mechanisms. When it comes to catalysis, experimental data often cannot give detailed information about the formation and cleavage of chemical bonds within a system, but it can give us basic information about stable intermediates and structures of the complexes formed, which are important for mechanisms and modelling of a system. In that sense, experimental and theoretical (bio)chemistry are inseparable and each gives an answer to one piece of the puzzle. Computational approaches are used to study mechanisms and formation of intermediates in different steps of the same.

Currently, one can use *Ab Initio*, Density-Functional Theory (DFT), semi-empirical and Molecular Mechanics (MM) methods to study enzymatic mechanisms. These methods are based on different theoretical approaches and their usage depends on the number of used atoms in the model and computational power available. The accuracy of the result is directly connected to the chosen approach. The Post-Hartree-Fock methods are the most accurate but require a lot of computational power, therefore can only be used on a small models (often around ~10-20 atoms). Hartree-Fock methods allow more atoms in the system but they are less accurate than Pos-HF. In this work Density-Functional Theory methods were used as they are less computationally demanding than typical Pos-HF method, but it describes biological systems almost as accurate as the some of the Pos-HF alternatives, and considerably better than standard HF methods. Alternatively, the semi-empirical methods can be employed. Although, less demanding and based on HF formalism, they include some approximations and parameters that make them less accurate. Lastly, Molecular Mechanics methods can be employed to study biological system composed of thousands of atoms at low cost and computational power. However, as such methods are based on Newton’s classical physics and consider atoms as non-deformable spheres with charges and does not include electrons (“spring and ball” model), they cannot be used directly to study reactions and electronic events. Nowadays, there is also a possibility to combine different approaches through hybrid methods. Firstly, there are full enzyme QM/MM models or full enzyme models that consider enzyme dynamic effects. **[32, 42-45]** Alternatively, in the cluster model approach there is one chosen model of the active site, which is treated with quantum mechanics and as accurately as possible. **[46-49]** We opted for the QM/MM method, with the and DFT method as this is currently one of the best approach to study enzymatic mechanism. In the following chapter, these methods will be described in detail with focus on DFT and QM/MM methods.

2.1. Classical Mechanics

The interaction between two particles, like the motion of the Earth around the Sun or some other two-body system, is the gravitational force and it can be treated by classical mechanics **[50]:**

$$V(r_{12}) = -C_{grav}\frac{m_1 m_2}{r_{12}}. \qquad \text{Equation 2.1}$$

The Newton's second law of dynamics in differential form can be written as follows. **[50]**

$$-\frac{\partial V}{\partial r} = m\frac{\partial^2 r}{\partial t^2} \qquad \text{Equation 2.2}$$

Thus, includes a centre of mass system so that internal motion becomes a “particle” motion with a reduced mass **[50]:**

$$\mu = \frac{M_{Sun} mEarth}{M_{Sun} + m_{Earth}} = \frac{m_{Earth}}{1 + \frac{m_{Earth}}{M_{Sun}}} \cong m_{Earth} \qquad \text{Equation 2.3}$$

The approximation in this equation is that Sun is stationary and Earth is moving around the Sun, $\mu = 0.999997 m_{Earth}$. This is introduced by the fact that the mass of the Sun is $3 \cdot 10^{5}$ times larger than the Earth's. Moreover, the motion is in a plane and polar coordinate system (2D) consisted of *r* and *q* (**Figure 2.1**). The interaction depends only on the distance, *r*. **[50]**

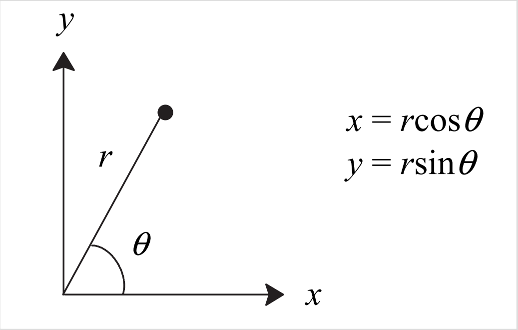

Figure 2.1 A polar coordinate system

Each bound orbit (elliptical) has associated total energy, and in classical mechanics there are no constraints on it. The energy of the two particles infinitively far apart corresponds to positive and negative values of the total energy, where positive values correspond to unbound solutions (hyperbolas) with kinetic energy larger than the potential energy, and negative values correspond to bound orbits (ellipsoids) with kinetic energy less then potential one.

Correspondingly, bound solutions are stationary orbits or points and particles returns to the same value within defined time interval. **[50]**

2.2 Molecular Mechanics (MM)

One of the major difficulties, that computational methods face, is the calculation of the electronic energy for some nuclear configuration to give a potential energy surface. **[50]** Additionally, the potential energy surface (PES) is defined by the potential energy of set of atoms over all possible atomic movements and arrangements. Thus, PES is a hyper surface with 3N - 6 coordinate dimensions, where N is the number of atoms ≥3, and its dimensionality is derived from the 3D nature of Cartesian space. Consequently, each point on the surface is defined by a vector X: **[51]**

$$X \equiv (x_1, y_1, z_1, x_2, y_2, z_2, \ldots, x_N, y_N, z_N)\,. \qquad \text{Equation 2.4}$$

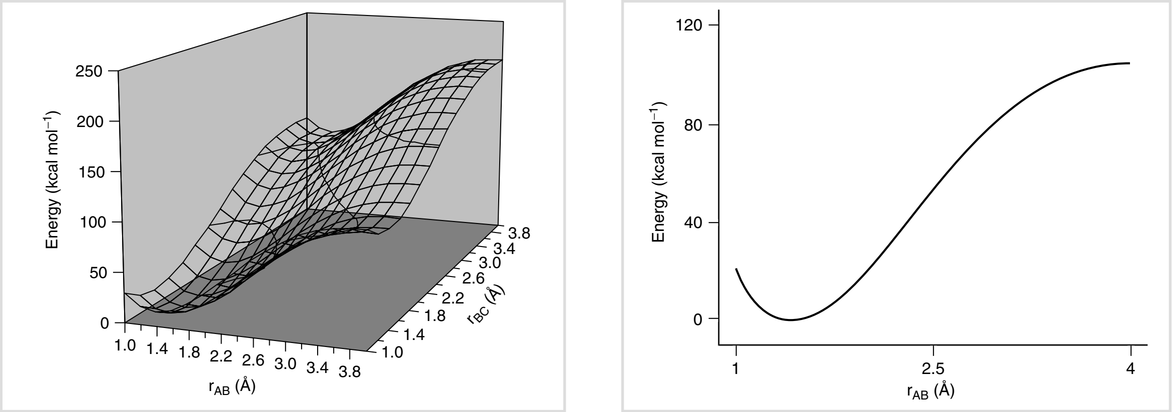

Figure 2.2 Potential energy surface for the hypothetical molecule ABC with 3N-6=3 coordinate degree of freedom and extra dimension for energy, where AB and BC are bond lengths. The PES energy shown as a function of one dimension (the AB bond length) while the other dimension is fixed.

Force field (FF) methods bypass this step by writing the electronic energy as a parametric function of the nuclear coordinates, as well as by fitting the parameters. In addition, parameters are fitted to experimental or higher level computational data. In these methods, electrons are not considered as individual particles and atoms are the “building blocks”. Therefore, information about the bonds has to be provided explicitly and is not a result of solving the electronic Schrödinger equation. Moreover, all the quantum nuclear motions are neglected, which means that the dynamics of the atoms are treated by Newton's laws of motions and classical mechanics. All molecules are described as a "ball and spring" (Hook's law) **[52]**, whereas atoms have different sizes and "softness", and bonds have different lengths and "stiffness". The energy is calculated at a given geometry of stable molecules and/or different conformations. The calculated energy is the energy minimum on the potential energy surface. Thus, the force field methods are referred to as *molecular mechanics* (MM) methods. All force field methods are based on the observation that molecules are consisted of structurally similar units. For example, all C-H bonds are roughly constant between 1.06 and 1.10 Å, and their stretch vibrations are between 2900 and 3300 cm^{-1}. Thus, C-H force constants are also comparable. Force field methods are somewhat a generalisation of the basic organic "ball and stick" models with the non-fixed atoms and bonds. The calculations enable one to predict relative energies and barriers for different conformations. In force fields, this idea is implemented as an atom *type*, which depends on the atomic number and the chemical bond type the atom is involved in. **[50]**

2.2.1 The Force Field Energy

The energy of the force field is written as a sum of energy terms describing bonded interactions like stretching, angle bending, torsional energy for rotation around a bond, non-bonded interactions (van der Waals and electrostatic interactions), and coupling between the first three terms. This means that the energy is calculated by a class I additive potential energy function. **[50, 53]** Furthermore, as MM does not use wave function for energy calculations, the energy is calculated as follows.

$$V_{system} = V_{bonded} + V_{non-bonded} \qquad \text{Equation 2.5}$$

This means that these methods require parameters from experimental data or *computational* calculations. This allows to approximate quantum mechanical PES with less computational power. **[53, 54]**

Correspondingly, the energy function of the nuclear coordinates, geometries and relative energies are calculated by optimisation, where stable molecules correspond to minima on the PES and they can be located by minimising the force field energy (E_{FF}) as a function of the nuclear coordinates. Transition states then can be described through location of transition structure on the E_{FF} surface. **[50]**

There are many different force fields that have been optimised and developed for specific types of systems. AMBER (Assisted Model Building with Energy Refinement) **[55]** is one of the most used ones for biomolecules. AMBER software includes ff10 **[56]** and GAFF (*General AMBER force fields*) **[57]** force fields that have been used in this work.

Several other often used force fields include CHARMM (*Chemistry at Harvard Macromolecular Mechanics*) **[58]**, GROMOS (*Groningen Molecular Simulation package*) **[59]** and OPLS (*Optimized Potentials for Liquid Simulations*) **[60]**.

2.2.1.1 The Bonded Interactions

In AMBER force fields, the bond interactions are divided into three terms: the bond stretching, the angle bending and the dihedral angle terms as follows:

$$V_{bonded} = \sum V_{str} + \sum V_{angle} + \sum V_{dihedral}\,. \qquad \text{Equation 2.6}$$

The bond stretching contributions are approximated by a harmonic oscillator as a function of the bond length (l), whereas the angle bending contribution as a function of the angle between three adjacent atoms (θ) **[54, 61]**

The bond stretching interactions and its contribution to the overall potential energy are described as

$$V_{bond} = \frac{1}{2}k_b(l - l_0)^2, \qquad \text{Equation 2.7}$$

where K_b is the force constant, l is the bond length and l_0 is the bond length at the equilibrium. **[54, 61]**

The angle between three adjacent atoms (θ) is described in the following equation:

$$V_{angle} = \frac{1}{2}k_a(\theta - \theta_0)^2, \qquad \text{Equation 2.8}$$

where k_a is the force constant, θ is the angle between three adjacent atoms and θ_0 is the angle between these atoms at the equilibrium. Only two parameters are needed to calculate these two potential energies, the force constant, k_a and the bond length, l_o or angle, θ_0.

The dihedral angle term or torsional angle is associated with the energy of the rotation of the atoms (A, B, C and D) separated by three bonds. Two dihedral angles can be considered, between planes ABC and BCD. The energy is given as a cosine functions,

$$V_{dihedral} = \frac{1}{2}k_d(1 + cos(n\omega + \gamma), \quad \text{Equation 2.9}$$

where k_d is the energy barrier for the dihedral rotation, ω is the dihedral angle (0° to 360°), γ is the dihedral angle where energy is minimum, and n defines the number of minimums. **[54, 61]**

2.2.1.2 The Non-Bonded Interactions

The non-bonded interactions include electrostatic and van der Waals interactions,

$$V_{non-bonded} = \sum V_{vdw} + \sum V_{el}. \quad \text{Equation 2.10}$$

The electrostatic interactions are result of the charges or permanent dipoles and are described by the Coulomb equation. The Coulomb equation considers atoms as charged points separated only by their interatomic distance as follows

$$V_{elec}\,(i,j) = \frac{1}{4\pi\varepsilon}\frac{q_i q_j}{r_{i,j}}, \quad \text{Equation 2.11}$$

where q_i and q_j are atomic charges of the atoms i and j, respectively, and $r_{i,j}$ is the distance between them, whereas ε is the dielectric constant. **[54, 61]**

Furthermore, the van der Waals interactions describe repulsive and attractive interactions which are not described by the Coulomb law. These non-bonded interactions include nuclear repulsion (Pauli's repulsion force, instantaneous and induced dipole attraction (London forces). In the AMBER force fields, the potential energy of van der Waals interactions is calculated using a 12-6 Lennard-Jones potential as described in **Equation 2.12. [54, 61]**

$$V_{van\ der\ Waals}(i,j) = \varepsilon_{i,j}\left(\left(\frac{\sigma_{ij}}{r_{ij}}\right)^{12} - \left(\frac{\sigma_{ij}}{r_{ij}}\right)^{6}\right), \quad \text{Equation 2.12}$$

where $\varepsilon_{i,j}$ is the function minimum; $r_{i,j}$ is the distance between atoms *i* and *j*; ε is the dielectric constant and σ_{ij} is the interatomic distance when energy is equal to zero. **[54, 61]**

2.3 Molecular Dynamics (MD)

Molecular dynamics (MD) simulations have been used to study protein stability and folding, molecular docking, transport through the cellular membranes and different conformational rearrangements. Moreover, it gives valuable information about the conformations of the systems, as well as thermodynamics and flexibility. Depending of the movements that we want to study and the computational cost, one chooses the duration of the MD simulations. Different movements and their time-scales can be seen in the *Table 2.1.*

Table 2.1 Different movements of the enzymes and their time-scales.

Type of motion	Functions	Time and Amplitude Scales
Local motions, atomic fluctuations, side chain motions	Ligand-docking flexibility, temporal diffusion pathways	Femtoseconds (fs) to picoseconds (ps), 10^{-15}-10^{-12} s, less than 1 Å
Medium-scale, loop, terminal-arm, rigid-body motions	Active site conformations, adaptation, binding specificity	Nanoseconds (ns) to microseconds (μs), 10^{-9}-10^{-6} s, 1-5 Å
Large-scale, domain, subunit motions	Hinge-bending motion, allosteric transitions	Microseconds (μs) to milliseconds (ms), 10^{-6}-10^{-3} s, 5-10 Å
Global motions, helix-coil transition, folding-unfolding, subunit, association/ dissociation	Hormone activation, protein functionality	Milliseconds (ms) to hours (ms), 10^{-3}-104 s, more than 10 Å

All MD simulations are based on the integration of the Newton's Second law, which gives data about velocity and position of each atom. A differential equation derivative from the Newton's law is defined for each particle in the system through some duration interval:

$$\frac{d^2x_i}{dt^2} = \frac{F_{x_i}}{m_i}, \quad \text{Equation 2.13}$$

where m is mass of the particle, x_i is the coordinate and F_{Xi} is the force.

The equation is difficult to solve analytically, therefore a finite integration step (Δt(is used to numerically calculate the position and the velocity for each atom, respectively:

$$\vec{x_i}(t_0 + \Delta t) = \vec{x_i}(t_0) + \vec{v_i}(t_0) \times \Delta t + \frac{1}{2}\vec{a_i}(t_0) \times \Delta t^2, \quad \text{Equation 2.14}$$

$$\vec{v_i}(t_0 + \Delta t) = \vec{v_i}(t_0) + \vec{a_i}(t_0) \times \Delta t\,. \quad \text{Equation 2.15}$$

Correspondingly, three different variables are used to describe the motion of the system. Atomic positions are usually obtained through X-ray crystallography or NMR, whereas the velocity is obtained by random assignment from a Maxwell-Boltzmann's distribution at the given temperature, *T*. Thus, the acceleration of each particle is calculated as the ratio of the force and the atomic mass. **[54]**

For each calculation, an integration step has to be set. Integration step defines the time interval between position and velocity calculations for all atoms in the system. Additionally, the smaller integration step, the higher computational cost and the minimum errors. In practice, this problem is solved by taking a ten times smaller integration time in comparison to the fastest movement in the system which is usually hydrogen bond stretching (C-H) ~ 10 *fs*. **[62]**

2.3.1 Ensembles

A macroscopic system is characterised by a+2 state functions, where α is the number of components in the system. We use statistical mechanics to describe macroscopic properties with microscopic events. In general, temperature, pressure, volume and number of particles are examples of the state functions. All macro states are defined as an ensemble of micro states under the same thermodynamic conditions. Therefore, there are several ensemble types:

- Canonic ensemble - number of particles (N), volume (V) and temperature (T) are constant,
- Isothermal-isobaric - N, pressure (P) and T are constant,
- Micro canonic - N, V and total energy (E) are constant,
- Grand canonic - V, T and chemical potential (μ) are constant.

We used the canonic (NVT) ensemble for the equilibration phase, and the isothermal-isobaric (NPT) ensemble for production phase through our MD simulations. **[54]**

2.3.2 Periodic Boundary Conditions And The Cut-Off

In MD simulations, our system is placed in a cubic water box. To avoid effects of the surface and any additional errors, the real system is presented in the centre of an infinite cubic network of replicas. The calculations are performed only for the central unit, but the movements are reproduced in all units. The chosen solvation box should be big enough to prevent atom interactions of the same atom with different boxes. Therefore, we used a minimum distance of 10 Å between the atoms of the enzyme and the surface of the box. **[62]**

The non-bonded interactions can be short and long range, whereas the short ones are described by Lennard-Jones potentials. Thus, the potential energy of the van der Waals interactions is calculated by *12-6 Lennard-Jones potential* where the highest term is r^{-6} dependent. This means that far away atoms already have small contribution to the total potential energy. In terms of Coulomb interactions with a r^{-1} dependency, more atoms influence the total potential energy. Therefore, as it is impossible to calculate all the non-bonded interactions for all the replica unites, a truncation radius is usually defined as an approximation to make the function smooth. **[62]**

2.4 Quantum Mechanics

The first concept of Quantum Theory was described by Max Planck in 1901, where he defined a quantum of matter and electricity on a black body. That work led to proportional relation between the energy and the radiation frequency known as Planck-Einstein relation:

$$E = h\nu, \tag{Equation 2.16}$$

where, *E* is the energy of a photon with frequency υ, and *h* is the Planck's constant (6.626069×10^{-34} $J\ s$).**[63]**

After that, Albert Einstein explained the photoelectric effect **[64]** discovered by Hertz **[65]**, whereas Compton confirmed the particle nature of the electromagnetic vale in 1923. **[66]** One year after, Louis de Broglie confirmed the reciprocity of the wave-particle duality of all matter. Further, each body has associated wave and it depends on its momentum, *p:*

$$\lambda = \frac{h}{p}, \tag{Equation 2.17}$$

where λ is the wavelength and p is momentum.

Afterwards, in 1927, Heisenberg introduced the uncertainty principle **[67]**, which indicates that it is impossible to accurately know both the position and the moment of a particle at the same time, as described in **Equation 2.18**,

$$\sigma_x \sigma_p \geq \frac{\hbar}{2}, \tag{Equation 2.18}$$

where σ_x and σ_p are the errors associated with the position and momentum, and ħ is the reduced Planck's constant (ħ = $h/2\pi$). **[67]**

Consequently, Dirac, Fermi, Born, Davisson, Germer, Debye and Maxwell introduced five fundamental postulates of quantum mechanics. The first postulate defines the system mathematically, which means that a physical system is defined by a wave function depending on the coordinates *x*, *y* and *z*, and time (t). Thus, it determines all the properties of a system. **[68, 69]** Moreover, a wave function is the probability amplitude which gives probability to find the electron as a function of the electron position. **[68]**

The second postulate describes how to get information about the system's properties through operators:

$$\hat{A}\Psi = e\Psi\,. \qquad \text{Equation 2.19}$$

The third postulate defines the eigenvalue, which is the only information that can actually be measured when the specific operator is used. **[68]**

2.4.1 Atoms Like Hydrogen

If we want to compare the Sun and the earth to particles at a quantum level, that would be like the nucleus and one electron like in a hydrogen-like atom. The Coulomb interaction is holding the nucleus and electron together. This interaction is described as follows **[50]**:

$$V(r_{12}) = \frac{q_1 q_2}{r_{12}}\,. \qquad \text{Equation 2.20}$$

This interaction depends on the distance but includes the small mass of the electron. Therefore, Newton's equation is replaced with Schrödinger's equation, where the time-dependence can be separated out for bound states giving the time-independent Schrödinger equation as **[50]**:

$$\hat{H}\Psi = E\Psi\,. \qquad \text{Equation 2.21}$$

The Schrödinger's equation is derived from the second quantum mechanics postulate (**Equation 2.19**), where the Hamiltonian is the operator and the given eigenvalue is the total energy of a system. **[50, 68, 69]** Correspondingly, the

Hamiltonian operator for atom with nuclear charge of Z, hydrogen-like atom, can be written in Cartesian coordinates and atomic units as:

$$\hat{H} = -\frac{1}{2M}\nabla_1^2 - \frac{1}{2m}\nabla_2^2 - \frac{Z}{\sqrt{(x_1 - x_2)^2 + (y_1 - y_2)^2 + (z_1 - z_2)^2}},$$ Equation 2.22

where *M* is the nuclear and m is the electron mass *(m*=1 in atomic units). **[50]**

The Laplace operator is described in **Equation 2.23. [50]**

$$\nabla_1^2 = \frac{\partial^2}{\partial x_1^2} + \frac{\partial^2}{\partial y_1^2} + \frac{\partial^2}{\partial z_1^2}$$ Equation 2.23

The two separated kinetic energy operators as each depends only on three coordinates. However, the potential energy operator involves all six coordinates and the centre of mass system is introduced by the following six coordinates. **[50]**

$$X = \frac{(Mx_1 + mx_2)}{M + m}; x = x_1 - x_2$$ Equation 2.24

$$Y = \frac{(My_1 + my_2)}{M + m}; y = y_1 - y_2$$ Equation 2.25

$$Z = \frac{(Mz_1 + mz_2)}{M + m}; z = z_1 - z_2$$ Equation 2.26

In this case, *X, Y* and *Z* coordinates define the centre of mass system, and the *x, y* and *z* the relative position of the two particles. Consequently, the Hamiltonian operator can be rewritten as

$$\hat{H} = -\frac{1}{2}\nabla_{XYZ}^2 - \frac{1}{2\mu}\nabla_{xyz}^2 - \frac{Z}{\sqrt{x^2 + y^2 + z^2}}.$$ Equation 2.27

The first term involves only *X, Y* and *Z* coordinates, and the operator ∇^2_{XYZ} is separable in terms of *X,Y* and *Z*. Solution of the *XYZ* give us translation of the entire system in three dimensions, and *xyz* coordinate describes the relative motion of two particles in terms of a pseudo-particle (reduced mass m) relative to the centre of mass. **[50]**

In addition, in terms of hydrogen atom, the nucleus is ~ 1800 times heavier than the electron (reduced mass *0.9995m_{elec}*), which is similar to the Sun-Earth system. Thus, approximation considers this system as a stationary fixed nucleus with a moving electron. **[50]**

In this case, the motion occurs in three dimensions and the Schrödinger equation can be transformed into a spherical polar set of coordinates as described in **Figure 2.3.** Consequently, the potential energy and kinetic energy operators are described as follows. **[50]**

$$\hat{H} = -\frac{1}{2\mu}\nabla^2_{r\theta\varphi} - Zr$$

Equation 2.28

$$\nabla^2_{r\theta\varphi} = \frac{1}{r_2}\frac{\partial}{\partial r}r^2\frac{\partial}{\partial r} + \frac{1}{r^2 sin\theta}\frac{\partial}{\partial\theta}sin\theta\frac{\partial}{\partial\theta} + \frac{1}{r^2 sin^2\theta}\frac{\partial^2}{\partial\varphi^2}$$

Equation 2.29

The kinetic energy operator is almost separable in spherical polar coordinates and it can be solved. The negative total energy solutions are known as the bound solutions or orbitals, which can be classified in terms of *n*, *l* and *m quantum numbers*. **[50]**

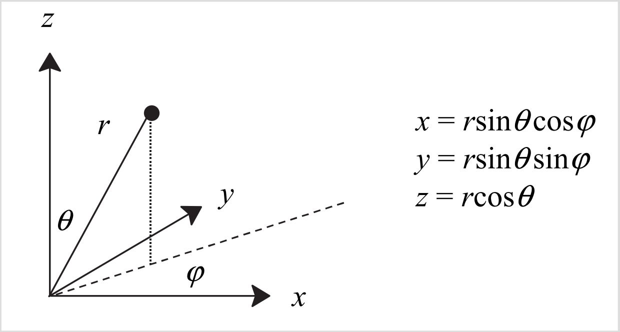

Figure 2.3 A spherical polar coordinate system.

Therefore, they correspond to the three spatial variables *r, q* and *j,* and arise from the boundary conditions on the wave function. Thus, the wave function has to be periodic in the variables *q* and *j*, and must decay to zero as r → ∞. As the Schrödinger equation cannot be completely separable in a spherical polar coordinates, some restrictions have to be applied; $n > l \geq |m|$. Additionally, the size of the orbitals is described by *n*, the shape of the orbital by *l*, whereas the orientation of the orbital in terms of a fixed coordinate system is described by *m*. When *l = 0* the orbital is called *s-orbital*, while p-orbital and d-orbital correspond to *l* = *1* and *l* = 2, respectively. **[50]**

The orbitals can be visualised by plotting a 3D objects that correspond to the wave function of specific value. Moreover, the orbitals can be written as a product of a radial function that describes behaviours regarding the distance *r* between the nucleus and electron, where spherical harmonic function Y_{lm} represents angular part in terms of *q* and *j* angles. For different quantum numbers, the orbitals are orthogonal and can be normalised. The orthogonality in the *l* and *m* quantum numbers (angular part) is stated from the shape of the spherical harmonic functions (*l* nodal planes - points where the wave function is zero), whereas in *n* quantum number (radial part) is from the (*n-l-1)* radial nodes in the wave function. **[50]**

$$\langle \Psi_{n,l,m} | \Psi_{n',l',m'} \rangle = \delta_{n,n'} \delta_{l,l'} \delta_{m,m'}$$ Equation 2.30

The energies of the wave functions are quantitised and only certain values are allowed. The energy is given by **Equation 2.31** and it depends on *n* for a given nuclear charge *Z*. **[50]**

$$E = \frac{Z^2}{2n^2}$$ Equation 2.31

In contrast to bound solutions and negative values, a positive total energy corresponds to scattering of an electron by the nucleus. **[50]**

2.4.2 The Helium Atom

In case we have a system with more than one electron the Schrödinger equation cannot be solved analytically. Thus, we have to implement some approximations. The simplest model would neglect the electron-electron interactions so that each orbital of the atom is obtained by solving a hydrogen-like system with one electron and one nucleus.(hydrogen-like orbitals:1s, 2s, 2p, 3s, 3p, 3d, etc., with $Z = 2$). After which, the total wave function is determined from the obtained orbitals subjected to the aufbau and Pauli principles, which state that the lowest energy orbitals should be filled first and only two electrons with different spin can occupy the orbital. To achieve the antisymmetry condition, the total wave function is written as a Slater determinant, which gives the non-normalised wave function. **[50]**

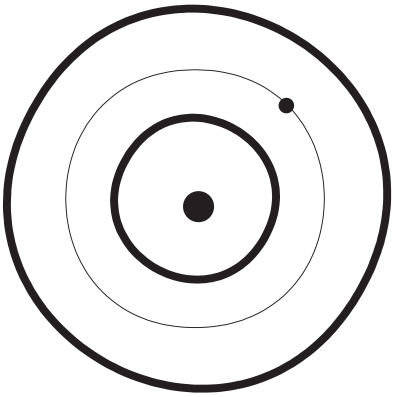

Figure 2.4. The Hartree-Fock model.

In the Hartree-Fock approximation, the *average* repulsion between the electrons is taken into account. If we know one orbital for one of the electrons, we can calculate the orbital for the second electron in the electric field. This is achieved through iterative methods and calculation of a self-consistent orbitals' set. **[50]**

The solution for a hydrogen atom is exponential, but this is not a case for many-electron systems. The Hartree-Fock model (**Figure 2.4**) is less accurate because of the equal mass of all the electrons and strong interactions between them. Moreover, the Hartree-Fock model accounts for ~ 99% of the total energy, but the remaining *correlation energy* is extremely important for chemical purposes. Additional, the main goal of correlated methods is to calculate remaining correlation energy of electron-electron interaction and approximately solve the Schrödinger equation. **[50]**

2.4.3 Hamiltonians And Approximations

To get information from the wave function about the properties of a studied system, we use operators. By applying an operator to an eigenfunction, gives us a wave function multiplied by the correspondent eigenvalue. Thus, the *Hamiltonian (H)* is an operator that gives us the total energy of a system from the wave function. The Hamiltonian is the result of the sum of the kinetic operators Tn and Te for nucleus and electrons, respectively, and the potential energy operators V_{ne}, V_{ee} and V_{nn}, that represent nucleus-electron, electron-electron and nucleus-nucleus interactions, respectively (**Equation 2.32**). **[54]**

$$\hat{H} = \hat{T}_n + \hat{T}_e + \hat{V}_{ne} + \hat{V}_{ee} + \hat{V}_{nn}$$ Equation 2.32

Correspondingly, the kinetic energy operator for a two particles system can be calculated as follows in **Equation 2.33. [54]**

$$\hat{T}_e = \left[\frac{-\hbar^2}{2\mu_{electron}}\left(\frac{\partial^2}{\partial x^2} + \frac{\partial^2}{\partial y^2} + \frac{\partial^2}{\partial z^2}\right)\right]_{electron} ; \hat{T}_n = \left[\frac{-\hbar^2}{2\mu_{nucleus}}\left(\frac{\partial^2}{\partial x^2} + \frac{\partial^2}{\partial y^2} + \frac{\partial^2}{\partial z^2}\right)\right]_{nucleus}$$

Equation 2.33

In addition, the potential energy operators are calculated using a Coulomb-like potential as described in **Equation 2.34.** For one-atom system, the potential energy operator is given only by the attractive energy between the nucleus and the electron, whereas for many-atom systems we have to include repulsion interactions between different electrons and nuclei. **[54]**

$$\hat{V}_{nn}=\sum_{A-B}^{N}\frac{Z_AZ_B}{r_{AB}};\hat{V}_{ne}=\sum_{A}^{N}\sum_{i}^{M}\frac{Z_AZ_i}{r_{iA}};\hat{V}_{ee}=\sum_{i-j}^{M}\frac{Z_iZ_j}{r_{ij}}$$

Equation 2.34

2.4.3.1 The Variational principle

The variational principle is an approximation for solving the Schrödinger equation through an arbitrary wave function. Consequently, this wave function to appropriately describe the coordinates of the system is being operated by the operator. Through **Equation 2.35** it is possible to prove that the obtained energy of the wave function is always greater or equal to the real and fundamental state energy. The relation itself allows us to determine through random wave function which one has the lowest value, and therefore the value closest to the real one. Moreover, we do not have to use a linear combination of orthonormal wave functions to build a wave function. **[51]**

$$\frac{\int \Psi_a \hat{H} \Psi_a d\tau}{\int {\Psi_a}^2 d\tau} \geq E_0$$

Equation 2.35

2.4.3.2 Born-Oppenheimer Approximation

For us to be able to apply a Hamiltonian to a wave function, we use the variational principle and the Born-Oppenheimer approximation. The Born-Oppenheimer approximation simplifies the wave function calculations and it postulates that the motion of the nuclei and electrons in the atom can be separated, which means that the total wave function can be written as the result of the nuclei function product by the electron wave function as described in **Equation 2.36. [70]**

$$\Psi_{Total}=\Psi_{nuclear}\times\Psi_{electronic}$$

Equation 2.36

If we apply this approximation to Hamiltonian operators, we can split the total system energy as follows in **Equation 2.37. [62]**

$$\hat{H}_{Total}=\hat{H}_{nuclear}+\hat{H}_{electronic}$$

Equation 2.37

The electronic and nuclear Hamiltonian are obtained through **Equations 2.38 and 2.39**, respectively. **[62]**

$$\hat{H}_{electronic} = \hat{T}_{electron} + \hat{V}_{electron-electron} + \hat{V}_{electron-nucleus}$$ Equation 2.38

$$\hat{H}_{nuclear} = \hat{T}_{nucleus} + \hat{V}_{nucleus-nucleus}$$ Equation 2.39

2.5 Wave Function-Based Theories

There are three main wave function based families of methods: the Hartree-Fock (HF), the post-Hartree-Fock (pos-HF) and the semi-empirical methods. These theories calculate the electronic part of the Schrödinger equation and create a PES. When it comes to catalytic mechanisms, the electronic Hamiltonian has the greatest contribution to the total energy. Thus, the nuclei position is usually fixed and the energy is calculated only with the electronic part.

2.5.1 The Hartree-Fock Theory

The Hartree-Fock theory (HFT) allows the exact calculation of the wave function for any system, as the Born-Oppenheimer approximation does not really allow energy calculation mathematically. The HFT describes the orbitals according to the movement of the electrons and gives the total wave function as a product of all described orbitals. The major disadvantage of this theory is the required computational power so it can be applied only to small systems. **[50]**

Although this theory is one of the most accurate ones, it neglects the electronic repulsion between two electrons, and consider their movement only a consequence of the electrostatic field produced by the nuclei and the average filed of the other electrons in the system (*n-1*). Consequently, each movement of the electrons can be described by a single-particle function, which is implicitly dependent on the movements and motion of other electrons in the system. **[70]**

The wave function can be calculated as the product of all single-particle functions of each electron in the system as described in **Equation 2.40.** However, due to the Pauli's exclusion principle, only electrons with different spin can occupy the same orbital. Therefore, the spin-orbital is calculated as the product of the spatial orbital and the spin function, α or β, as described in **Equation 2.41.**

$$\Psi_{Hartree\ Product}\ (r_1, \ldots, r_n) = \phi_1(r_1) \times \ldots \times \phi_n(r_n) \qquad \text{Equation 2.40}$$

$$\chi(x) = \phi(r)\ \alpha \qquad \text{Equation 2.41}$$

In the end, the wave function (Hartree product) is obtained using the spin-orbitals and not only the spatial orbitals as follows. **[70]**

$$\Psi_{Hartree\ Product}\ (x_1, \ldots, x_n) = \chi_1(x_1) \times \ldots \times \chi_n(x_n) \qquad \text{Equation 2.42}$$

As this calculation cannot be applied to all systems, Slater determinant (the spin orbitals determinant) has to be used to normalise and define the expression for all systems (**Equation 2.43**).**[70]**

$$\Psi_{electronic} = \frac{1}{\sqrt{N!}} \begin{vmatrix} \chi(x_1) & \cdots & \chi_N(x_1) \\ \vdots & \ddots & \vdots \\ \chi(x_N) & \cdots & \chi_N(x_N) \end{vmatrix} \qquad \text{Equation 2.43}$$

The variational principle allows the HF calculations, but the approximated solution is always greater than the real one. Correspondingly, better wave functions mean lower energy. After the application of the variational principle to the Slater determinant we obtain the following **Equation 2.44**. and **2.45**. **[51, 70]**

$$E_{electronic} = \int \chi_i \sum_{i=1}^{N} \hat{h}_\imath \chi_i d\tau_i + \sum_{i=1}^{N} \sum_{j>i}^{N} (J_{ij} + K_{ij}) \qquad \text{Equation 2.44}$$

$$\hat{h}_\imath = \hat{T}_{elect.} + \hat{V}_{elec.-nucleus} \qquad \text{Equation 2.45}$$

where last term describes the bi-electronic interactions; J_{ij} is Coulomb operator which describes the potential energy of an electron within the full electronic field distributed through occupied spin orbitals; K_{ij} is the exchange operator which describes the energy variation from electron exchange between two orbitals. **[70]**

The Hartree-Fock equation defines the Fock operator (**F**) as the sum of each spin orbital, which corresponds to the first term in **Equation 2.46**, as follows. **[70]**

$$\hat{F}\chi_i = \varepsilon_i \chi_i \qquad \text{Equation 2.46}$$

2.5.1.1 The Hartree-Fock Self-Consistent Field (SCF)

To solve the HF equation and obtain the energy of specific electron in the system, one has to know all the spin orbitals (solutions) beforehand. This problem is solved through the *self-consistent field* (SCF) method, where the equation is solved iteratively, as well as stopping when the solutions are self-consisted. So, in this method, a Fock operator is constructed with a trial set of spin-orbitals to solve the HF equations. Afterwards, this new set is used to construct a new and revised Fock operator to obtain better solutions, and so on. This cycle is repeated until a convergence criterion has been met. **[70]**

2.5.1.2 Linear Combination of Atomic Orbitals (LCAO)

The *linear combination of atomic orbitals* (LCAO) method is applied to molecules, as HF calculation is successful only in terms of atoms. Furthermore, the linear combination of basis sets was proposed by Roothaan and Hall as an approximation to HF calculations. The molecular orbitals are described as functions of one electron with atomic nucleus in the centre. The molecular orbital wave function based on a set of basis sets using spin orbitals is described in **Equation 2.47**. **[70]**

$$\psi_{MO} = \sum_{r} c_r \chi_r$$

Equation 2.47

2.5.2 Density Functional Theory

The Hartree-Fock, *ab initio*, methods all start with an approximation when solving the HF equation to obtain the spin-orbitals for construction of the configuration state functions. Their limitation lies in difficulties in accuracy when using large basis sets on large molecules. Alternatively, a *density functional theory (DFT)* is based on the concept of electron probability density, and does not solve a wave function. The DFT takes into account electron correlation and is less demanding computationally. Moreover, DFT describes systems with d-block metals much better and experimentally close than HF methods. **[51, 70]**

In DFT, the energy is described as an electron probability density, *r*, for a system of *n* electrons, where *r(r)* corresponds to total electron density at specific point *r* in space. Thus, the electronic energy (*E*) is a functional of the electron density and is written as *E[r],* which means that for a given function *r(r)* there is one corresponding energy. The term "functional" refers to a mathematical method of assigning a number to a function. **[70]**

2.5.2.1 Konh-Sham Orbitals And Equations

The initial concept of density functional for the energy was described and approximated in early models of the *Thomas-Fermi method* **[71, 72]** and the *Hartree-Fock-Slater method.* However, the formal proof of the theory was given by Hohenberg and Kohn **[73]** where they stated that the ground-state energy and all other electronic properties of the same state are determined by the electronic density. Their theorem proves only the existence of such functional, but tell us nothing about the dependence of energy on the density. Afterwards, DFT became more developed with the implementation of the derivation of a set of one-electron equations from which the electron density (*p*) could be obtained. **[70]**

As in restricted Hartree-Fock theory, only systems with paired electrons and described by the same spatial one-electron orbitals are considered. The *Kohn-Sham* theorem shows the form of the exact ground-state electronic energy (*E)* of an *n-electron* system in **Equation 2.48. [70]**

$$E[\rho] = -\frac{\hbar^2}{2m_e}\sum_{i=1}^{n}\int \psi_i^*(r_1)\,\nabla_1^2\psi_i(r_1)dr_1 - j_0\sum_{I=1}^{N}\frac{Z_I}{r_{I1}}\rho(r_1)dr_1 + \frac{1}{2}j_0\int\frac{\rho(r_1)\rho(r_2)}{r_{12}}dr_1dr_2 + E_{XC}[\rho],$$

Equation 2.48

where the first term on the right represents the kinetic energy of the electrons, the second term is the attraction between electron and nucleus, where the sum is over all nuclei *N* with the index *I* and the atomic number Z_I. The third term represents the Coulomb interaction between the total charge distribution at r_1 and r_2, whereas last term describes the exchange-correlation energy of the system, which is a functional of the density ρ and includes all non-classical electron-electron interactions. Furthermore, the only term in the **Equation 2.48** that cannot be obtained exactly is the term E_{XC}. Additionally, the Hohenberg-Kohn theorem states that *E* is a functional of the electron density, and therefore E_{XC} must be as well. Because of this issue, some approximation had to be made. **[70]**

In the Equation 2.48, the one-electron spatial orbitals ψ_i *(i = 1, 2, . . . , n)* are called the Kohn-Sham orbitals, whereas the exact ground-state electron density is given by **Equation 2.49**.

$$\rho(r) = \sum_{i=1}^{n} |\psi_i(r)|^2, \qquad \text{Equation 2.49}$$

where the sum is over all the *KS orbitals*; ρ is obtained once the KS orbitals have been computed. **[70]**

By solving the Kohn-Sham equations we obtain the KS orbitals, which are derived through application of the variational principle to the electronic energy *E[ρ]*. **[70]**

$$\left\{ -\frac{\hbar^2}{2m_e}\nabla_1^2 - j_0 \sum_{I=1}^{N} \frac{Z_I}{r_{I1}} + j_0 \int \frac{\rho(r_2)}{r_{12}} dr_2 + V_{XC}(r_1) \right\} \psi_i(r_1) = \varepsilon_i \psi_i(r_1) \qquad \text{Equation 2.50}$$

$$V_{XC}[\rho] = \frac{\delta E_{XC}[\rho]}{\delta \rho} \qquad \text{Equation 2.51}$$

The KS equations for the one-electron orbitals are described in **Equation 2.50**, where ε_i are the KS orbital energies; V_{xc} is the exchange-correlation potential and the functional derivative of the exchange-correlation energy (**Equation 2.51**). The importance of KS orbitals is that they allow the density (ρ) to be computed through **Equation 2.49** for ρ. Moreover, their solutions are self-consistent. **[70]**

So, through super positioning of atomic densities, we can guess the electron density *r*. We use some fixed approximate form of the functional *E_{xc}[r]* so that we can compute V_{XC} as a function of *r*. Afterwards, the set of the KS equations is solved to give us an initial set of KS orbitals from which we compute an improved density through **Equation 2.49.** The cycle is repeated until the exchange-correlation energy is converged, after which we compute electronic density through **Equation 2.48. [70]**

The KS orbitals can be either computed numerically or expressed in terms of a set of basis functions which requires finding the coefficients in the basis set. In terms of basis sets, STOs and GTOs can be used. In terms of accuracy, DFT formalism is usually computed more efficiently than HF formalism, but that does not necessarily mean it is more accurate. **[70]**

2.5.2.2 The Local Density Approximation (LDA)

The main source of error in DFT calculations is usually the approximation of E_{XC}. In addition. This functional is separated into two different functionals, an exchange functional that represents exchange energy, and a correlation functional that represents the dynamic correlation energy. The exchange-correlation functional in the *local density approximation (LDA)* is described as:

$$E_{XC} = \int \rho(r)\varepsilon_{XC}[\rho(r)]dr, \qquad \text{Equation 2.52}$$

where $e_{xc}[r(r)]$ represents the exchange-correlation energy for each electron in a homogeneous electron gas that has constant density: an infinite number of electrons move through infinite volume with an uniform and continuous positive charge distribution to retain electron neutrality. Thus, the **Equation 2.52** is an approximation as in reality charges are not uniformly distributed in molecules. Although, LDA's accuracy decreased with varying electron density and number of molecules, the LDA is extremely accurate for predicting structural properties. The LDA for which the exchange and correlation functionals depend only on *r* and not on its derivates, the obtained binding energies are larger than experimental values. **[70]**

Additionally, the gradient *r* is usually added to the exchange-correlation energy as a non-local correction that takes the inhomogeneity of the electron density into account. There are different gradient-correct functionals and the LDA with gradient correction is called the *generalised gradient approximation (GGA)*. **[70]**

Throughout the years, many different exchange-functionals have been developed especially for DFT: mPWPW91 **[74, 75]**, B3LYP **[76, 77]**, BLYP **[76, 77]** and PBE **[78, 79]**. In our work we opted for B3LYP **[76, 77]** functional as studies have shown extremely good results for biological systems. The BLYP functional is combined of the gradient-corrected exchange functional (A.D. Becke) and the gradient-corrected correlation functional (C. Lee, W. Yang, R. G. Parr).

DFT can also be applied to open-shell atoms and molecules with the extension of LDA, the *local spin-density approximation (LSDA)*. The spin density refers to the spin-up and spin-down electron density difference. In this case, the exchange-correlation energy depends on the spin and total electron density. So, the LSDA is usually used to study magnetic structures of metals and alloys. Moreover, for studies regarding the polarizabilities, excitation energies and electronic absorption spectra, *time-dependent density functional theory (TD-DFT)* is applied (**Equations 2.53 and 2.54**). **[70]**

$$\left\{ -\frac{\hbar^2}{2m_e}\nabla_1^2 - j_0\sum_{I=1}^{N}\frac{Z_I}{r_{I1}} + j_0\int\frac{\rho(r_2,t)}{r_{12}}dr_2 + V_{ext}(t) + V_{XC}(r_1,t)\right\}\psi_i(r_1,t) = i\hbar\frac{\partial}{\partial t}\psi_i(r_1,t)$$

Equation 2.53

$$\rho(r,t) = \sum_{i=1}^{n}|\psi_i(r,t)|^2$$

Equation 2.54

In TD-DFT, external potential V_{ext}, the exchange-correlation potential, the KS orbitals and the density are time-dependent. Its goal is to explore how the density changes with varying external potential. **[70]**

2.5.2.3 Basis Sets - Dispersion Corrections

Basis sets represent sets of mathematical functions used to describe atomic orbitals in the quantum mechanical methods. The more accurate orbital description, the better the results, however greater the computational cost. Thus, we use the basis set that is able to describe the real wave function and give us real results, and the basis sets that solve the exchange-correlation functional in a simple manner. *Slater-type orbitals (STOs)* and *Gaussian-type orbitals (GTOs)* are typically used. **[50]**

2.5.2.3.1 Slater-Type Orbitals (STO)

The *Slater-type orbitals* (STOs) are described in the **Equation 2.55**, where N is normalisation constant and $Y_{l,m}$ are spherical harmonic functions. The STOs do not have radial nodes so nodes in the radial part are introduced with linear combinations of STOs. Additionally, these orbitals are used for atomic and diatomic systems for highly accurate calculations. When it comes to DFT methods, STOs can be used only in cases when exact exchange is not included and where the Coulomb energy is obtained by fitting the density in the set of auxiliary functions. **[50]**

$$\chi_{\zeta,n,l,m}(r,\theta,\varphi) = NY_{l,m}(\theta,\varphi)r^{n-1}e^{-\zeta r} \qquad \text{Equation 2.55}$$

2.5.2.3.2 Gaussian-Type Orbitals (GTO)

The *Gaussian-type orbitals* (GTOs) are describe in terms of Cartesian coordinate system as shown in **Equations 2.56** and **2.57**.

$$\chi_{\zeta,n,l,m}(r,\theta,\varphi) = NY_{l,m}(\theta,\varphi)r^{2n-2-l}e^{-\zeta r^2} \qquad \text{Equation 2.56}$$

$$\chi_{\zeta,l_x,l_y,l_z}(x,y,z) = Nx^{l_x}y^{l_y}z^{l_z}e^{-\zeta r^2} \qquad \text{Equation 2.57}$$

These orbitals are improved in terms of e^{-r} dependence of the STOs, so that now we have e^{-r^2} dependency. In case all defining-orbital integers are zero, the GTO is an s-orbital, whereas for one unitary value of the integers, the p-orbital is defined with three different combinations (p_i, p_u and p_l). Correspondingly, there are six d-type orbitals (i, j, k = 2), x^j, y^j, z^j, xy, xz and yz, but the Schrödinger equation can predict only first five. **[50, 51]**

However, GTOs do not reproduce the orbital amplitude accurately because of their $r^{\wedge j}$ dependence. Also, there are the *contracted GTO functions (CGTO)* which are obtained throughout linear combination of GTO and STO orbitals. This means a better description of the orbitals, with a lower computational cost, but these orbitals do not have any particular role when it comes to chemical process as the description of the electron near the nucleus is not really significant. **[51, 70]**

Afterwards, the *split-valence basis (n-abcG)* concept was introduced, where the core orbitals are treated with Gaussian primitives, whereas the valence orbitals are treated with two or three different Gaussian contraction schemes. In *n-abcG*, *n* represents the number of primitives used to contract GTO of the core orbitals, while *abc* represents the treatment and division assigned to the valence orbitals. The most common basis set is 6-31G which is characterised by six primitive GTOs and the valence orbitals are into two. The most internal orbital is described with three primitive GTOs, whereas the external one only by one. **[51, 70]**

Furthermore, the CGTOs do not describe molecular systems accurately as they are not polarised and cannot be modified by the surrounding atoms. Thus, polarisation and diffuse functions are introduced and combined with GTOs. For 6-31G set that uses d-orbital polarisation, they are rewritten as 6-31G(d) or 6-31G*, which means that the d-orbital is polarising p-orbital. The polarisation functions have higher angular momentum than the valence orbitals and if we polarise one orbital with another one, we are distorting their electron cloud and defining a bond. Additional polarisation of s-orbitals by p-orbitals can be included and is written as 6-31G(d,p) or 6-31G**. Additionally, the diffusion functions are included for highly negative molecules like hydride transfer. In these systems, the electron cloud is more displaced, and we use diffusion functions to heavy atoms or heavy atoms (+) and hydrogen atoms (++). **[50, 51, 70]**

In this work we used 6-31G(d) and 6-311++G(2d,2p) sets as we studied one hydride transfer which is characterised by a negative charge.

2.5.3 Semi-Empirical Methods

In contrast to ‘pure’ theoretical *ab initio* methods, semi-empirical methods can be applied to large systems. Although these methods include the same approximations as *ab initio* and the ones that come from accuracy of experimental data for parameters, semi-empirical methods are widely used as adjustable parameters are optimised to reproduce important chemical properties. **[70]**

The optimisation itself is a very complex and difficult process as accurate experimental data are rarely available and the process itself is very time-consuming when parametrising large number of molecules simultaneously. Initially, semi-empirical methods were developed for conjugated p-electron systems studies. **[70]**

The semi-empirical methods differentiate in the neglect of a differential overlap, and in the inclusion of an overlap integral. The *complete neglect of differential overlap (CNDO)* is the most basic approach and considers only the valence orbitals using STO orbitals, as well as the only one function per orbital. All the two-electron integrals are parametrised and their dependency is reduced from N4 to N2, after which the rest is calculated through algebraic formulae and not explicit integration. Thus, these approach fails to accurately predict molecular structures. **[70]**

Furthermore, the *intermediate neglect of differential overlap (INDO)* better describes electron-electron interactions based on the spectroscopic transition. After that, the *neglect of diatomic differential overall (NDDO)* was developed and it neglect the differential overlap only when the basis function of a specific electron belongs to different atoms. Consequently, other methods were developed such as MNDO (*Modified Neglect of Diatomic Overlap*), AM1 (*Austin Model 1*), PM3 (*Parametrized Model 3)* and PM6 *(Parametrized Model 6)*. **[70]**

2.6 The Nuclear Hamiltonian

To obtain the total energy, we have to include the *nuclear Hamiltonian* to our calculations. The nuclear Hamiltonian provides the activation and reaction Gibbs free energy variation, which is important in the catalytic mechanisms. In general, the nuclear motion is never fixed, and the internal energy of the system is a sum of the *electronic energy* and the *zero-point energy* (ZPE). To obtain these values, we compute the thermal corrections and add them to the electronic energy to obtain the real energy at the specific temperature. **[62]**

The transitional energy ($E_{transational}$) is calculated when particles are placed in a box, whereas the rotational energy ($E_{rotational}$) is calculated with rigid rotor model. The vibrational energy ($E_{vibrational}$) is computed for each vibrational mode. We compute nuclear Hamiltonian through *frequency calculations* which also provide us with one imaginary frequency for transition states. The frequencies are calculated through the second derivative of the energy. Both reactants and products (minima) have positive frequencies. The internal energy at a specific temperature is obtained through **Equation 2.58**. **[62]**

$$E_{T=273.15\ K} = E_{electronic} + [E_{transational} + E_{rotational} + E_{vibrational}]_{T=273.15\ K}$$

Equation 2.58

2.7 Hybrid Methods

The *ab initio* and DFT methods are computationally demanding and limited to systems tipically comprised by only ~ 100-200 atoms. If we want to study large systems like enzymes we have to use a method that allows us to treat thousands of atoms. Thus, we use hybrid methods that combine the quantum mechanics and the molecular mechanics approaches. These methods are often referred to as QM/MM methods, because we treat the active site with quantum mechanics and the rest with molecular mechanics. In our work we used the QM/MM method to study the second hydride transfer of HMGR catalytic mechanism with the DFT to describe the active site. **[50, 51, 70]**

2.7.1. The QM/MM

The molecular mechanics calculations require less computational time than quantum methods, but they do not describe the system in terms of electrons or orbitals. Thus, a new method was developed to treat the active site of the enzyme with quantum mechanics, while treating all the rest faster and less accurate with molecular mechanics. This method can be applied when the studied system can be split into two regions: the active site (QM calculations) and the rest of the system (MM calculations). With QM calculations we can accurately treat bond-breaking and forming, while taking into account the rest of the protein and atoms using MM. Moreover, QM/MM calculations are iterative methods, where the conformation of the active site atoms is fixed while the MM calculation is run on the MM subpart. Correspondingly, the effects of the QM on the MM subpart and its potential are included by treating the QM atoms as fixed MM atoms. After that, the QM method is applied to the active site using self-consistent field calculations or similar that includes the MM subpart's potential energy. Consequently, the low energy geometry of the QM region is obtained, after which this new conformation of the active site is used to repeat the process until the geometry of all atoms is converged. **[70]**

Generally, for a two-partitioned system (*high and low layer)* we have to perform three calculations in order to obtain the total energy of the system (E), as shown in **Equation 2.59**. Firstly, the energy is calculated under the MM level, then the high layer's (HL) energy is calculated through MM, after which the low layer (LL) region is obtained by subtracting the last energy to the first one. Correspondingly, the energy of the HL is computed using the QM level and the final energy is summed. **[70]**

$$E^{All}_{QM/MM} = E^{All}_{MM} - E^{HL}_{MM} + E^{HL}_{QM} \qquad \text{Equation 2.59}$$

The greatest difficulty in these calculations is the interaction between two regions when the boundary between two regions intersects covalent bonds. However, this issue is resolved by the 'capping' atoms procedure, where one part of the molecule can be changed with another atom like hydrogen. **[70]**

This is called *link-atom approach* and it allows energetic and structural corrections. The HL atoms whose bonds are cut in between layers is replaced with hydrogen or halogen atoms, but these atoms are not considered during the calculations as they are not part of the system. The other method is less used and is called *frozen orbital approach*. **[51]**

The energy in the system can be calculated using additive or subtractive method. However, the additive method cannot compute the coupling term accurately. **[80]**

In addition, the *integrated molecular orbital / molecule mechanics (IMOMM)* is a QM/MM scheme that combines a high-level molecular orbital calculations with MM. The QM/MM is generally used for large system studies (proteins, metalloenzymes, catalysis…). **[70]**

2.7.2. ONIOM

ONIOM (our own *N*-layered integrated molecular orbital molecular mechanics) is a subtractive hybrid method that allows partitioning of a studied system. **[81]** It requires an explicit charges description, as well as the spin multiplicities for each subsystem. **[51]** Usually, the active site is treated with the DFT method, while the protein is treated with the MM. We used a two-layer system (**Figure 2.5**) where the HL was treated with DFT (B3LYP) and the LL with MM. The energy was obtained through **Equation 2.60.**

$$E_{DFT/MM}^{All} = E_{MM}^{All} - E_{MM}^{HL} + E_{DFT}^{HL} \quad \text{Equation 2.60}$$

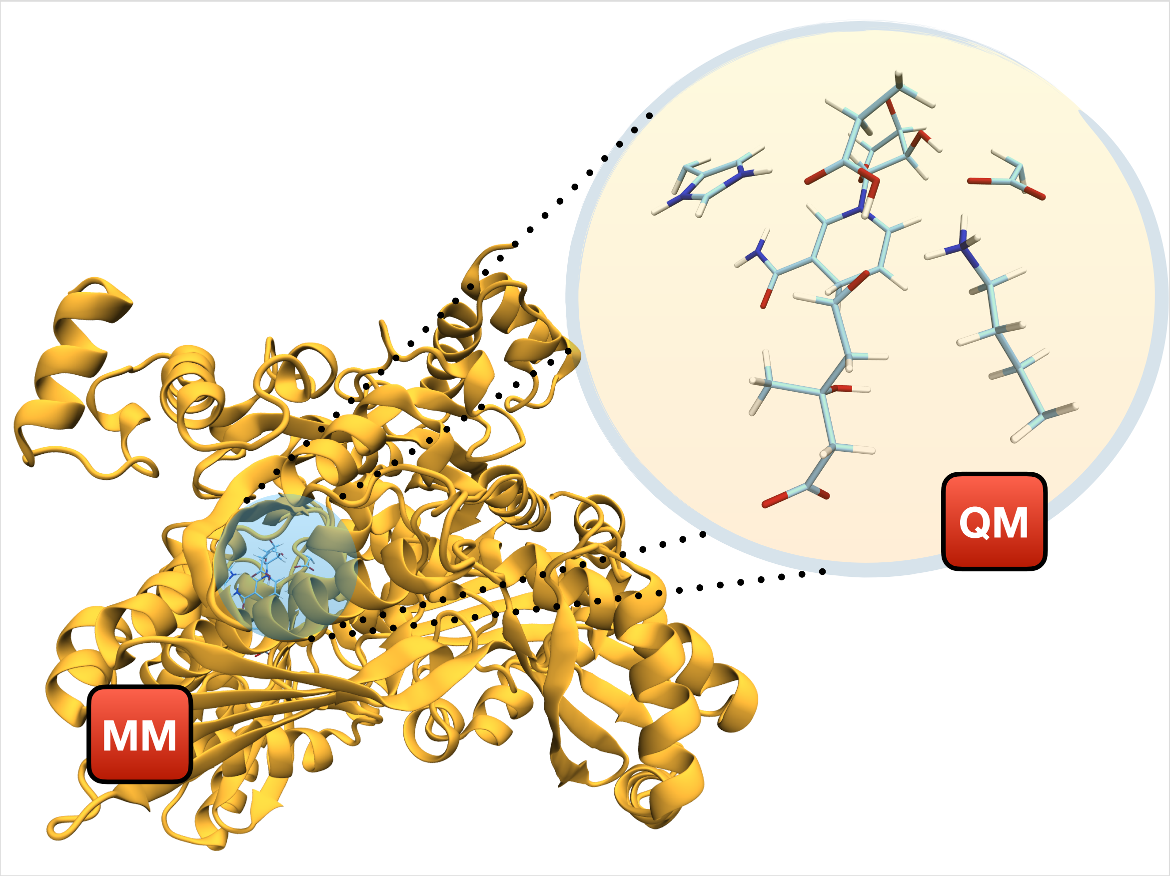

Figure 2.5 Graphical representation of the two-layered ONIOM model using VMD software.

2.7.2.1 Mechanical And Electrostatic Embedding

Due to some difficulties related to the electrostatic and van der Waals interactions between atoms of two different layers, some methods were developed to transfer the polarisations effect between two layers as polarisations effects are neglected and the boundary regions are over polarised.

Mechanical embedding allows LL polarisations which is induced by the HL. The HL part is calculated without polarisations effect, after which the LL part is calculated with induced HL polarisations through punctual charges. The HL charges are obtained in each step but the new optimisation step does not include these new charges. Thus, the Lennard-Jones parameters are not updated throughout the simulations. Electrostatic embedding allows the opposite polarisations, a HL polarisations by the LL part, which is introduced through an extra mono-electronic term added to the QM Hamiltonian. In addition, this term is calculated from the atomic charge distribution in the LL part. This method adds a new self-consistent cycle so that the MM layer has to converge in terms of the new orbital coefficients obtained after each cycle of the QM. **[62]**

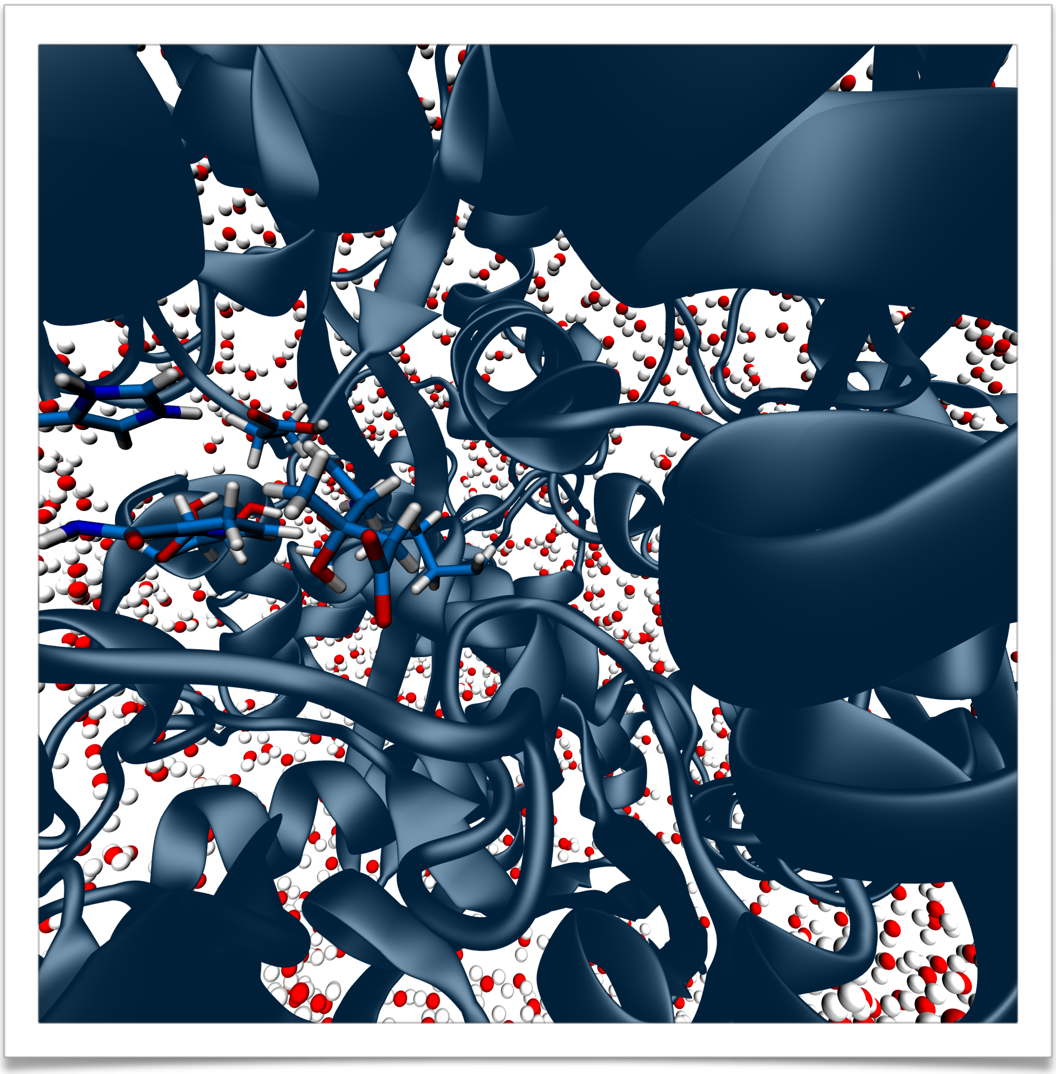

Chapter 3 - Results and Discussion

3. Introduction

The research itself was composed of many steps, which included the initial preparation of the model from crystallographic structure taken from the Protein Data Bank (PDB). We used the *GaussView* **[82]** software to convert mevalonate analogue to a mevaldehyde structure which we needed to study the second reduction step of the mechanism. Since the enzyme itself is extremely large, we decided to extract only two chains from the PDB structure, that is with the most favourable distances between substrate and cofactor. After that, the enzyme with a substrate and the cofactor were solvated using TIP3P type of water molecules. **[83]**

After that, we neutralised the negative charge of the system with sodium ions (Na+) added with *Xleap*. We parametrised the external substrate using *ab initio* Hartree-Fock method and performed short molecular dynamics simulations (minimisation, equilibration and production) to get the most stable conformation. After we obtained the most stable structure, preparation of the model for the ONIOM calculations followed. To get the transition state structure (TS), it was necessary to run linear transit *scan* calculations along selected reaction coordinates, after which we optimised the transition state and run frequency calculations to confirm that the TS is the one we were looking for. Furthermore, optimisation and frequency calculations for both, the reactants and the products, and single point calculations for the transition state, reactants and products for all the hypothesis studied, were conducted, as well. After that we estimated the Gibbs free activation and reaction energy of the three different models. All structures were fully optimised to the minimum or the transition states, if not stated otherwise. Consequently, we analysed the structural properties obtained through MD simulations. We used *Visual Molecular Dynamics (VMD)* **[84]** software as a visualisation tool, as well as to obtain all the figures in this chapter. All calculations were performed with the *Gaussian09* software **[82]** or with the AMBER simulation package.

3.1 Model Preparation

3.1.1 A Crystallographic PDB Structure Analysis

The initial step involves the choice of a proper crystallographic structure from the PDB bank database, which includes all the cofactors and substrates we need to study a catalytic mechanism. However, as we based our hypothesis on the first hydride transfer, as well as the Oliveira et al.'s previous study, **[31]** we chose the same wild-type structure as in their study, PDB ID: 1DQA. The structure includes nicotinamide adenine dinucleotide phosphate (NADP), coenzyme A (CoA) and 3-hydroxy-3-methyl-glutaric acid (mevalonate analogue), and has resolution of 2 Å. Currently, there are many different crystallographic structures of human HMGR, but only few of them include all the substrates and cofactors as shown in the *Table 3.1*.

Table 3.1 List of crystallographic structure of human HMG-CoA reductase with substrates and/or cofactor.*

PDB ID	Resolution (Å)	Chains	Ligands
1DQ8	2.1	A, B, C, D	COA, DTT, MAH
1DQ9	2.8	A, B, C, D	HMG
1DQA	2.0	A, B, C, D	COA, MAH, NAP

** Where DTT is 2,3-DIHYDROXY-1,4-DITHIOBUTANE, MAH = 3-HYDROXY-3-METHYL-GLUTARIC ACID, HMG = 3-HYDROXY-3-METHYLGLUTARYL-COENZYME A, NAP = NADP NICOTINAMIDE-ADENINE-DINUCLEOTIDE PHOSPHATE, COA = COENZYME A.*

We opted for one dimeric structure composed of intercepting monomeric chains A and B as the distances between the cofactor, substrate and catalytic residues were the most favourable. Furthermore, the hypothesis included one dimeric structure, NADPH cofactor and mevaldehyde intermediate. As in the initial crystallographic structure there were only NADP and mevalonate analogue (i.e. a product analogue), the structures were modelled using *GaussView Software*. **[82]**

All catalytic residues' protonation states were taken from the most favourable model of *Oliveira et al.*'s study **[31]**. They used H++ and PROPKA (ph=6.8) to predict the protonation states. Based on the read literature, in the first model Glu98 and Lys639 were protonated, whereas His405 was double-protonated. In the second model, Glu98 and Lys639 were also protonated, but His405 was only protonated and not cationic. In the last model, Glu98 and His405 were protonated, and Lys639 was deprotonated.

3.1.2 Model preparation

As previously mentioned, we had to model the $NADP^+$ and mevalonate analogue structures to NADPH and mevaldehyde intermediate using *GaussView software*. **[82]** To the NADP structure one hydrogen was added as shown in **Figure 3.1 (a)**, and as for mevalonate structure, 3-hydroxil group was changed to a carbonyl one (one hydrogen was erased directly from the carbon-3 atom and 3-hydroxil group was changed to a double bonded oxygen) as shown in **Figure 3.1 (b)**.

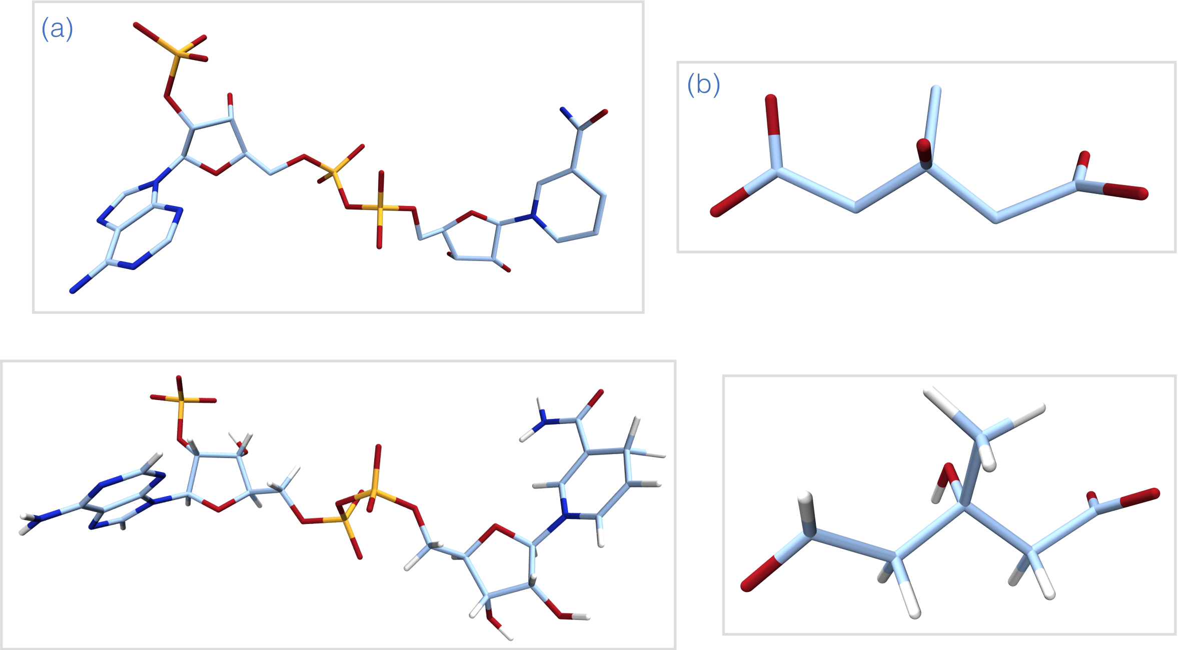

Figure 3.1 Graphical representation of the NADPH cofactor (a) and mevaldehyde substrate (b) taken from the crystallographic structure PDB ID: 1DQA (up) and parametrised structures (down) in *Licorice* using *Visual Molecular Dynamics* software (VMD).

3.2 Molecular Dynamics Simulations

After initial model preparation, a short MD simulation was run to relax the structure. The MD simulations included minimisation, equilibration and production phase. Consequently, the structure from the MD simulation with the most distances between NADPH, mevaldehyde and all the catalytic residues, as well as adequate geometry, was taken as the starting structure for all the following calculations.

3.2.1 Parametrisation

MD simulations require parametrisation of all the external molecules in the system which are not included in the parameters in the used force field. In this work the following force fields have been used: ff10 **[56]** and GAFF **[57].** Correspondingly, parameters for the mevaldehyde (*Table 3.2)* intermediate were obtained through *ab initio* Hartree-Fock (HF) method with the 6-31G(d) basis set (Atomic Charges). Other parameters for mevaldehyde were taken from the general amber force field using Antechamber. The parameters for NADPH (*Table 3.3)* were obtained from the literature **[85]**. Atom types were assigned to each atom of these molecules using the ANTECHAMBER **[86]** program from the AMBER12 **[55]** software package.

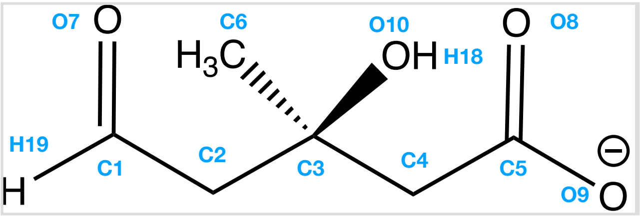

Figure 3.2 Structure of mevaldehyde.

Table 3.2 Charges for each atom in mevaldehyde substrate obtained from parametrisation with ff10 [56] and GAFF [57] force fields in AMBER12 [55] package.

Charges of mevaldehyde (a.u.)					
C1	0.587408	H18	0.438521	C5	0.894256
O7	-0.585257	H19	-0.314639	O9	-0.803099
H19	-0.01452	H20	0.05882	O8	-0.803099
C2	-0.264282	H21	0.05882		
H11	0.059044	H22	0.05882		
H12	0.059044	H23	-0.304992		
C3	0.582013	H24	0.034159		
O10	-0.775176	H25	0.034159		

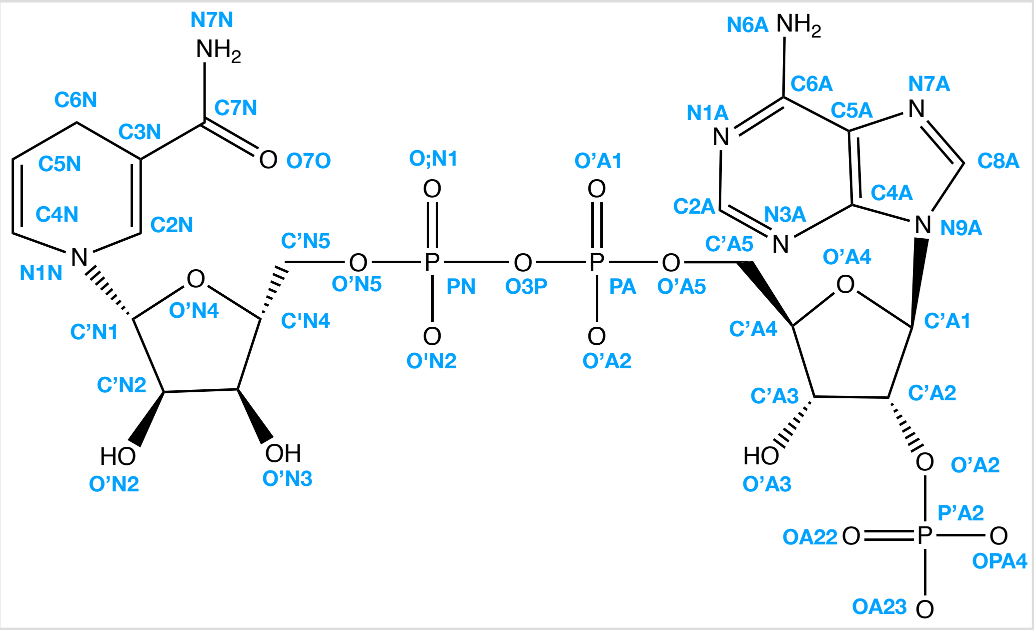

Figure 3.3 Structure of NADPH.

Table 3.3 Charges for each atom in NADPH cofactor obtained from **[85].**

Charges of NADPH (a.u.)							
C6N	-0.3552	**H'N2**	0.0972	OPA1	-0.8558	OA24	-0.8984
H6N	0.2219	**O'N2**	-0.6139	OPA2	-0.8558	C'A1	0.0394
C5N	-0.173	**HON2**	0.4186	O'A5	-0.5661	H'A1	0.2007
H5N	0.1257	**C'N3**	0.2022	C'A5	0.0558	N9A	-0.0251
C4N	0.1348	**H'N3**	0.0615	HA51	0.0679	C8A	0.2006
H41	0.0196	**O'N3**	-0.6541	HA52	0.0679	H8A	0.1553
H42	0.0196	**HON3**	0.4376	C'A4	0.1065	N7A	-0.6073
C3N	-0.2227	**C'N4**	0.1065	H'A4	0.1174	C5A	0.0515
C7N	0.8285	**H'N4**	0.1174	O'A4	-0.3548	C6A	0.7009
O7N	-0.6099	**O'N4**	-0.3548	C'A3	0.2022	N6A	-0.9019
N7N	-0.9935	**C'N5**	0.0558	H'A3	0.0615	H61	0.4115
H71	0.4047	**HN51**	0.0679	O'A3	-0.6541	H62	0.4115
H72	0.4047	**HN52**	0.0679	HOA3	0.4376	N1A	-0.7615
C2N	-0.184	**O'N5**	-0.5661	C'A2	-0.2829	C2A	0.5875
H2N	0.1422	**PN**	1.3729	H'A2	0.2326	H2A	0.0473
N1N	0.2293	**OPN1**	-0.8558	O'A2	-0.5828	N3A	-0.6997
C'N1	-0.0384	**OPN2**	-0.8558	P'A2	1.2972	C4A	0.3053
H'N1	0.1617	**O3P**	-0.576	OA22	-0.8984		
C'N2	0.067	**PA**	1.3729	OA23	-0.8984		

3.2.1 MD Simulations - Minimisation, Equilibration and Production

3.2.1.1 The MD simulations

After all the parameters and topology files were obtained using the AMBER12 package **[55]**, a short MD simulation was run. As previously mentioned, for this model the ff10 **[56]** and the GAFF **[57]** force fields were used for parametrisation. The system was neutralised with 8 sodium ions (Na+) and solvated using a TIP3P **[83]** type of water molecules with 10 Å distance from a protein, assigned using *Xleap* software. The system was equilibrated after four minimisation phases, after which one production phase was run. All MD simulations were done using SANDER software from AMBER12 package. **[55]**

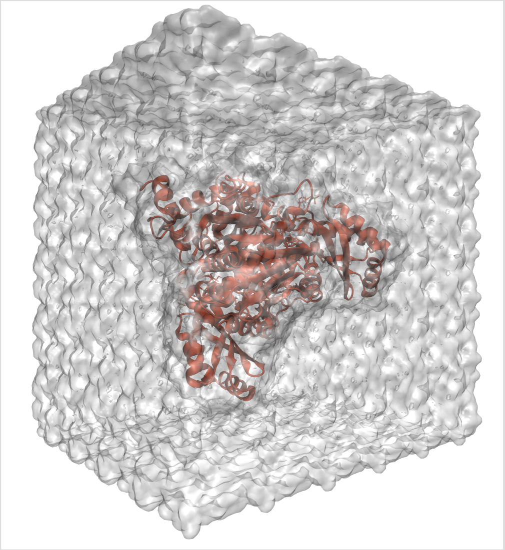

Figure 3.4 Graphical representation of the TIP3P water box with the chains A and B.

During the first 20 ps (integration step 2 fs), of the equilibration phase, the temperature of the system was increased from 0.00 K to 310.15 K in small increments using the Langevin thermostat, considering canonical ensemble (NVT). **[87]** After that, we run short production phase considering an isothermal-isobaric (NPT) ensemble for 20 ns. All the obtained results were analysed using *Ptraj* software **[88]** from AMBER12 package **[55]** and visualised using *Molecular Dynamics software (VMD)*. **[84]**

3.2.1.1.1 Structural Analysis

During the MD simulations, we obtained and analysed the general physical properties of the system as shown in the **Figure 3.5**, which indicates that the system was stabilised without any major conformational changes. Also, a *root mean square deviation* (RMSd) was determined, which shows how the protein is moving in the given time interval in comparison with the initial structure, highlighting possible conformational movements. The details diagram of the

RMSd for all system and chain A, as well as the backbone and the active site can be seen in the **Figure 3.6 (a),** whereas on the **Figure 3.6 (b)** detailed diagram comparison of the chain B can be seen with the entire system is shown.

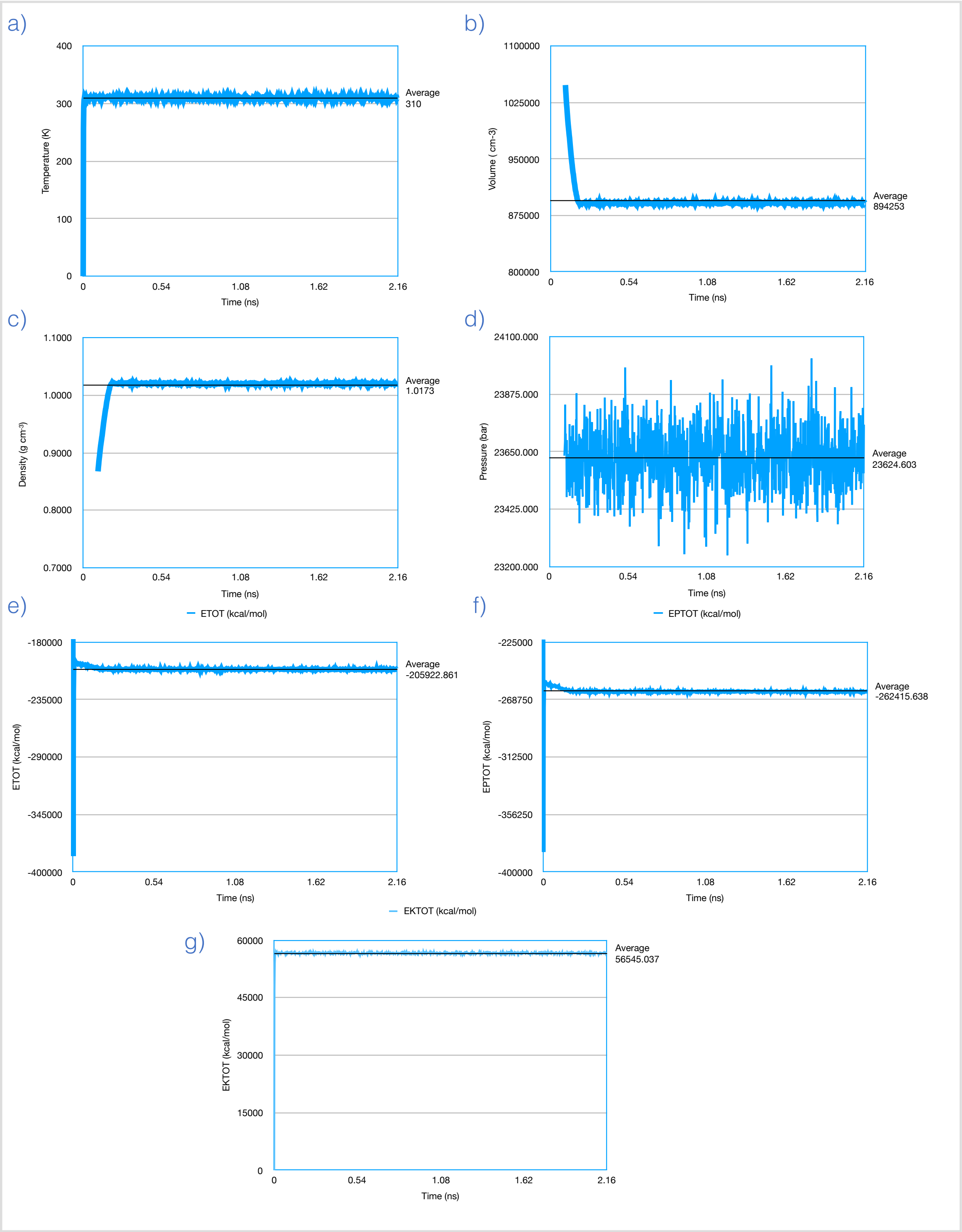

Figure 3.5 General physical properties (temperature, volume, density, kinetic, potential energy) obtained through MD simulations. Obtained temperature (K) (a), volume (cm^{-3}) (b), density (g/cm^{3}) (c), pressure (bar) (d), total energy (kcal/mol) (e), total potential energy (kcal/mol) (f), total kinetic energy (kcal/mol) (g).

As shown on the **Figures 3.6 (a)** and **(b)**, no major fluctuations have been observed for the chains A and B, as well as for the active site of the chain A that was used for all the later simulations. The RMSd of the entire system with the active site for catalytic residues Glu98, Lys639, His405 and Asp715, mevaldehyde substrate and cofactor NADPH of the chain A, was evaluated as 1.510Å±0.001 (**Figure 3.6 (a)**). The RMSd for the backbone was determined as 0.57Å±0.03.

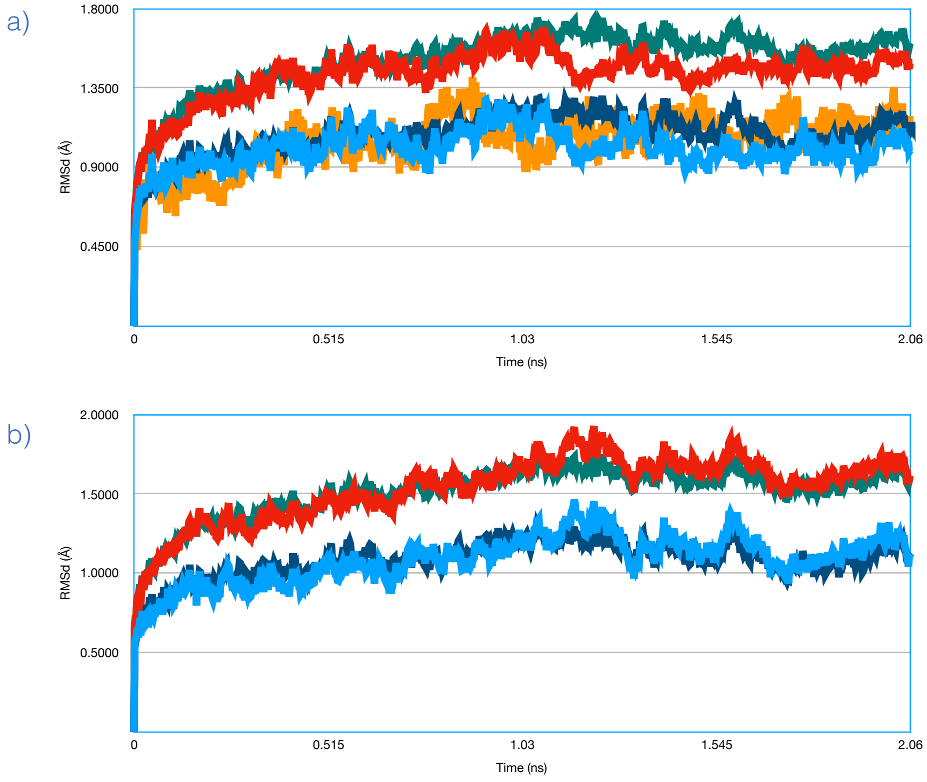

Figure 3.6 Graphical representation of the determined RMSd:

(a) Entire system (***blue***), entire system's backbone (***red***), chain A (***light blue***), chain A's backbone (***green***) and active site (***orange***).

(b) Entire system (***blue***), entire system's backbone (***red***), chain B (***light blue***) and chain B's backbone (***green***).

Additionally, we evaluated the *root-mean square fluctuations (RMSf)* which describes the flexibility of the protein in terms of each residue or atom. As seen in the **Figure 3.7** the most flexible parts are α-helices, whereas the least flexible parts are β-sheets. The residues in the active site are mostly less flexible, while the residues Leu410, Pro325 and Lys639 are the most flexible residues in the system.

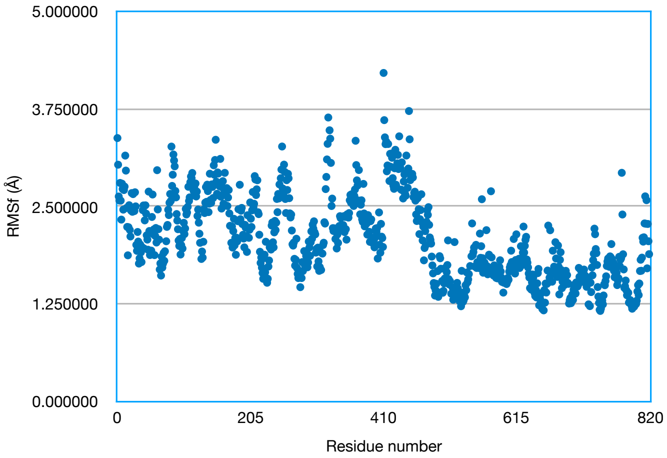

Figure 3.7 Graphical representation of the residue flexibility measured as RMSf (Å) vs. number of residues in the system.

Due to lack of water molecules in the near proximity of the active site, we did not evaluate radial distribution functional (RDF). However, the closest water molecule was around 5 Å from the active site, showing that the active site was well shielded from the solvent (**Figure 3.8**).

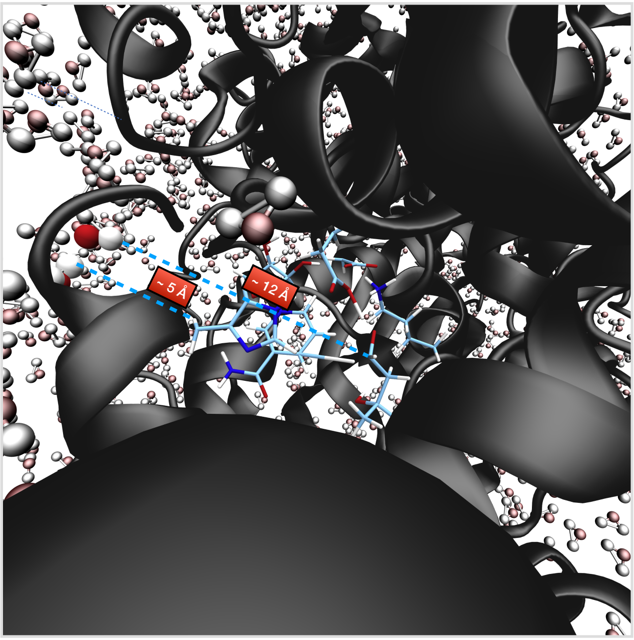

Figure 3.8 Graphical representation of the distance between the active site and the closest water molecules.

Furthermore, we determined hydrogen bonds that were occupied at least during 50% of the simulation time. *Table 3.4* shows the hydrogen bonds between the catalytic residues of the active site and other residues, as well as the substrate and cofactor.

Table 3.4 The list of all hydrogen bonds that include the residues from the active site with occupancy more then 50%.

DONOR	ACCEPTORH	ACCEPTOR	Occupancy (%)	Distance
815@O8	632@HG	632@OG	90.1	2.715 (0.12)
638@OD2	815@H18	815@O10	87.48	2.733 (0.12)
815@O10	538@HH21	538@NH2	81.75	2.840 (0.08)
818@O7N	538@HH12	538@NH1	56.41	2.833 (0.10)
98@OE1	639@HZ1	639@NZ	53.11	2.725 (0.09)
715@OD2	639@HZ3	639@NZ	50.49	2.760 (0.09)

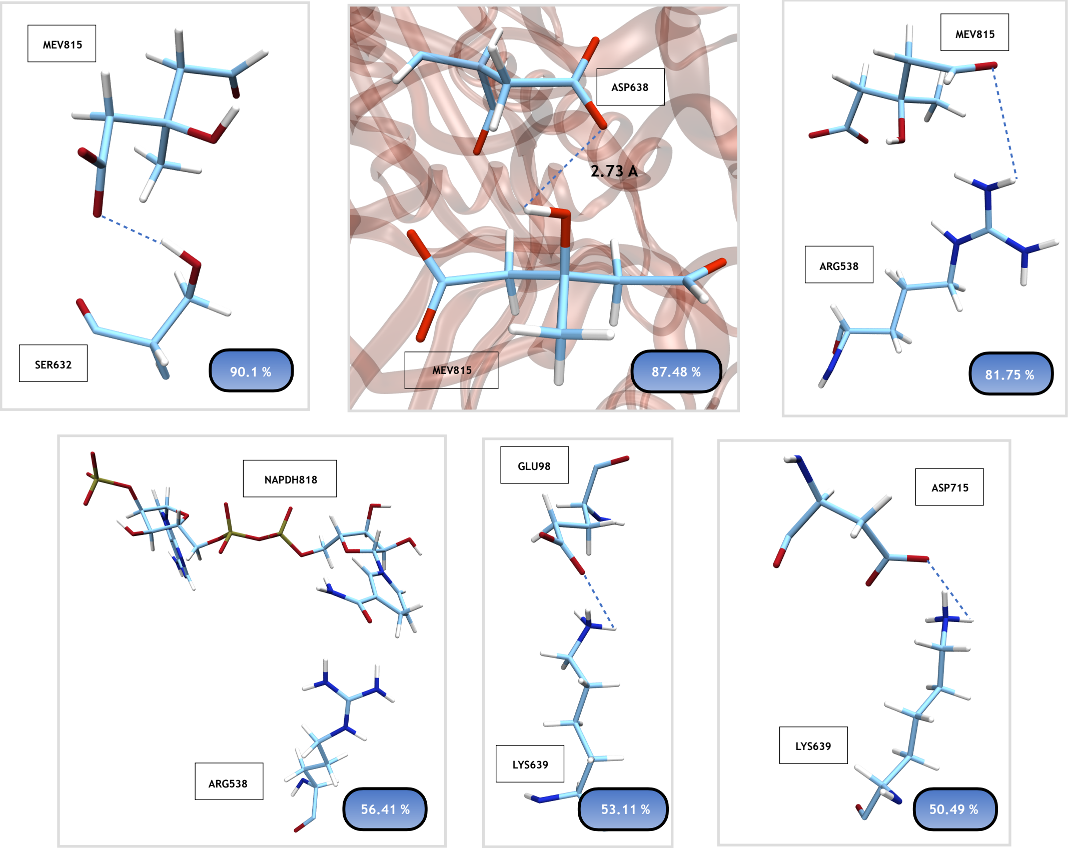

3.9 Graphical representation of the hydrogen bonds that include all the residues of the active site.

3.3 The Catalytic Mechanism - The Second Hydride Transfer

The main focus of our work was to model and study the second hydride transfer of HMG-CoA reductase shown in **Figure 3.10**. As mentioned before, we based our model on the most favourable model of *Oliveira et al.'s* **[31]** study. After molecular dynamics simulation, we used the structure with the most favourable distances and appropriate geometry between cofactor NADPH, substrate mevaldehyde and catalytic residues (Glu98, Lys639, His405 and Asp715) for all calculations.

Oliveira et al. **[31]** described the first and rate-limiting step of this reaction, where Lys691 protonated the mevaldyl-CoA, in contrast to the study of *PmHMGR* of *Haines et al.,* where Glu83 was proton donor. Besides, the reaction was more favourable when Glu559 was protonated, and not deprotonated like in the prokaryotic mechanism. A cofactor exchange happens prior to mevaldehyde formation **[18, 32]**, and the activation free energy of 17.8 kcal/mol was obtained with intermediate protonated by Lys691, whereas Glu559 and Asp767 were bonded, thus the weaker interaction between Lys691 and Asp767. *Haines et al.* **[3, 8]** suggested that for the second hydride transfer of prokaryotic enzyme, the activation barrier was 2.9 kcal/mol lower then in the first transfer and the proton donor was Glu83.

Mainly, there are three different models that can follow the *Oliveira et al.'s* study. Firstly, the reaction mechanism can proceed with the final protonation state of the first hydride transfer, where Lys639 is deprotonated, Glu98 is neutral (protonated) and His405 is cationic (double-protonated). After that it is likely that His405 will protonate Glu98, which will then protonate the Lys639. There is also one other possibility where Lys639 and Glu98 are protonated, whereas His405 is cationic as $^{-}$SCoA leaves the active site and protonates itself in the solvent. We assumed that $^{-}$SCoA leaves the active site and therefore we did not include it in the active site nor HL of the QM region.

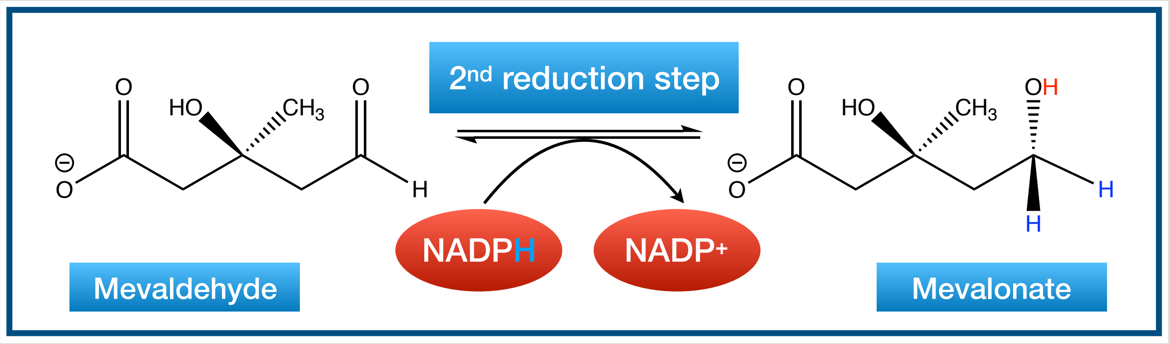

Figure 3.10 Generally accepted reaction for second hydride transfer of HMGCR catalytic mechanism.

As mentioned in the previous subchapters, the initial structure for all calculations was obtained through MD simulations, which we used to determine a potential energy surface (PES) through ONIOM **[94-102]** (QM/MM) calculations using *Gaussian09* software. **[82]** In the *high layer* (HL, quantum mechanics) we included mevaldehyde substrate, NADPH cofactor and Glu98, Glu98, Lys639, His405 and Asp715 catalytic residues, wheres in the *low layer* (LL, molecular mechanics) we included the remaining part of the protein and water molecules 5 Å of the protein **(Figure 3.11)**. Moreover, the HL region was calculated using DFT:B3LYP/6-31G(d) **[103-106, 107-114]**, whereas the LL region using AMBER force field. Surprisingly, in this mechanism no water molecules are near the active site nor relevant for the catalytic mechanism, therefore we fixed all the water molecules 15 Å from the active site. All the remaining atoms were free during the geometry optimisation so that the most favourable minima and conformation can be obtained, as all the movements and conformational changes affect entire system. We used electrostatic embedding in all calculations. **[91-93]**

Initially, we optimised the starting structure retrieved from the MD simulations and we optimised it a the minima. After that, we determined the transition state (TS) through *scan* calculations along the reaction coordinate of the mechanism. Furthermore, after the TS was obtained and fully characterised, the corresponding reactant and product structures were determined through geometry optimisation of the structures on the each side of the *scan* plot.

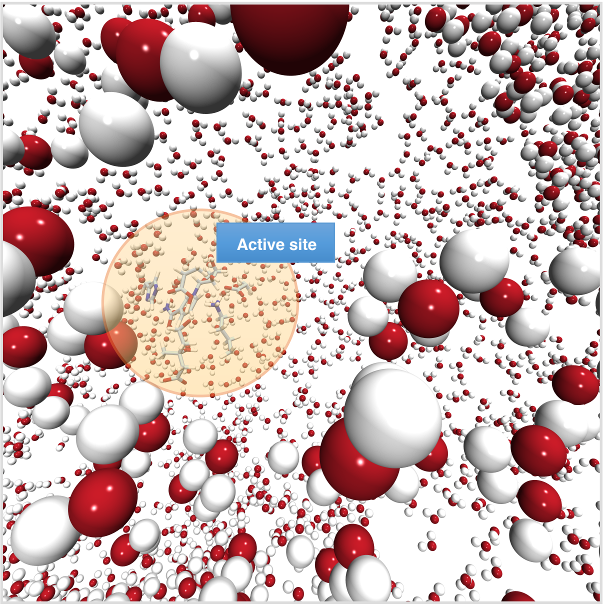

Figure 3.11 Graphical representation of the fixed water molecules in *VDW* and unfixed *Licorice* active site in the middle using *VMD software.*

Additionally, *intrinsic reaction coordinate (IRC)* calculations were used to determine the reactants and the products, but due to technical issues we used the prior method to obtain the required structures. Technically, both methods achieve the same result, but in the IRC method, the algorithm takes the obtained TS structure and finds the minima in reversed and forward coordinates to obtain reactants and products, respectively. In contrast to that, in the used method, we manually took one structure on each side of the *scan* plot and optimised it to the minima. All structures, reactants, TS and products, were determined using standard Gaussian convergence criteria. In addition, all minimal and Ts were characterised through nuclear Hamiltonian calculations or simply *frequency* calculations, where one imaginary (negative) frequency was obtained for the TS, whereas for reactants and products all vibrational frequencies were positive. Through these calculation we obtained the effect of the nuclei on the total energy. Correspondingly, all structures were additionally characterised through *single-point* calculations with the higher basis sets, B3LYP: 6-311++G(2d,2p). In the final result, thermal corrections were added. The energy difference between two structures is designated by the ΔE, which means that only an electronic Hamiltonian was used to determine the energy, whereas an activation energy (E_a) is the difference between the optimised TS and reactant. The difference between the products and the reactants is designated as E_r. After we withdraw the thermal corrections from the nuclear Hamiltonian calculations (enthalpy, entropy and zero-point corrections), we were able to compute the Gibbs free energy ΔG for the respective activation and the reaction energies. Correspondingly, when the reaction energy is negative, the reaction itself is exothermic, whereas for positive value the reaction is endothermic. If the Gibbs free reaction energy is negative, the reaction is exergonic, wheres for positive values, the reaction is endergonic. We used *GaussView* **[82, 83]** and *molUP* **[90]** to prepare and analyse all the files.

3.3.1 The Second Hydride Transfer

We modelled three different systems with the assumption that SCoA leaves the site deprotonated and protonates in the solvent. The only difference between these three models is the different protonation states of the Lys639 and His405. According to the previous studies, the proton donor for human HMGR should be lysine **[31]**, whereas in the prokaryotic enzyme glutamate **[3, 8]**. Additionally, all the protonation states of the catalytic residues were taken from the previous studies and literature, and help stabilise the charge delocalisation in the mechanism.

3.3.1.1 The First Model - Protonated Glu98 And Lys639, Double-Protonated His405 and Deprotonated Asp715

Firstly, we modelled a system with 92 atoms in the HL and 20 405 atoms in the LL. The HL included the full structure of mevaldehyde substrate, one part of the NADPH cofactor and side chains of the catalytic residues in the following protonation states: protonated Glu98 and Lys639, cationic (double-protonated) His405 and deprotonated Asp715 (**Figure 3.12**). The total charge of the system was -4, whereas the total charge of the HL was -1. Additionally, the mevaldehyde has an approximate charge of -1, NADPH -4, whereas His405 and LYS639 both +1. Asp715 has a charge of -1, whereas Glu98 is neutral.

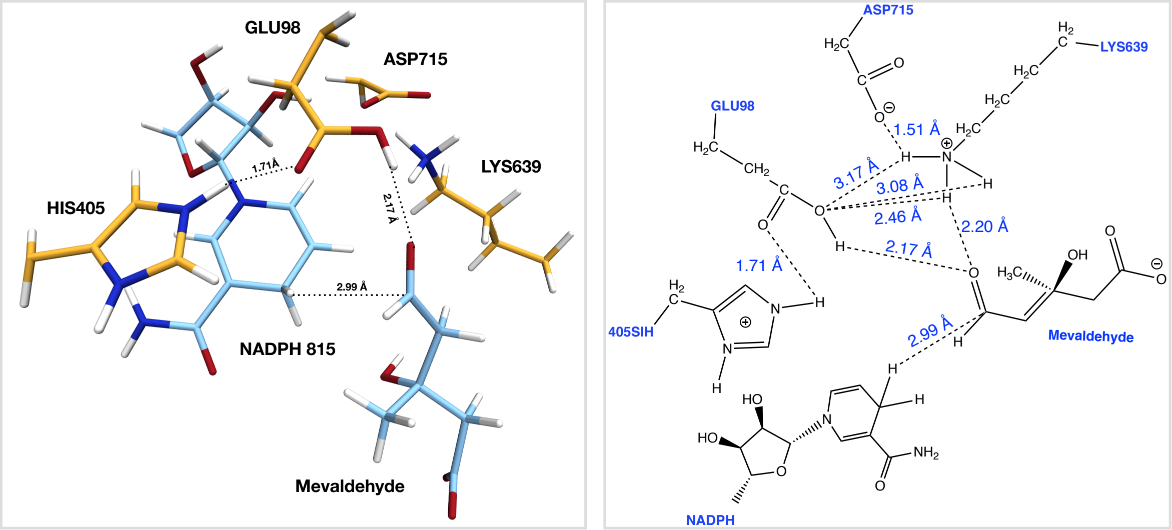

Figure 3.12 Graphical representation of the active site obtained from the optimised reactants' structure in *Licorice* using VMD software and ChemDraw.

The structure with the highest energy and peak was determined as the TS structure from the linear *scan* calculations. The *scan* gives us a rough evaluation of the energies of the system as generally, after which the structures are fully optimised and characterised with the geometry optimisation and nuclear Hamiltonian calculations.

After geometry optimisation, we determined energy difference values for reactants, TS and products, obtained through electronic Hamiltonian calculations, are shown in the **Figure 3.13**. The energy difference of the TS and the reactants corresponds to E_a, while the energy difference of the products and the reactants corresponds to E_r.

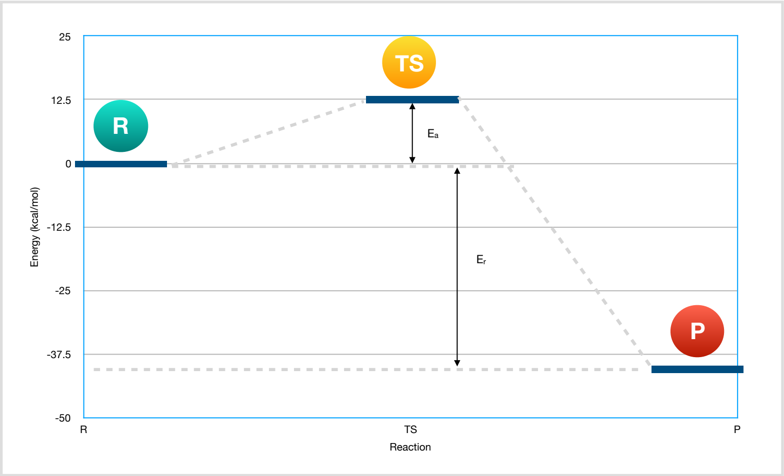

Figure 3.13 Graphical representation of approximate activation energy (E_a) and reaction energy (E_r).

After nuclear Hamiltonian calculations we determined the thermal corrections for enthalpy (ΔH), entropy (ΔS) and zero-point energy (ZPE), which were added to the previous results. Thus, we estimated the Gibbs free energies of the activation and the reaction. The **Figure 3.14** shows the fully characterised system with corresponding reactants, TS and products structures and the estimated delta G with a basis set B3LYP/6-311G(d) for the second hydride transfer of 13.0 kcal/mol.

Oliveira et al. **[31]** stated that the first hydride transfer occurred with the 17.8 kcal/mol of the activation barrier, whereas *Haines et al.* **[3, 8]** stated that for the second hydride transfer in *PmHMGR* occurred at the energy barrier 2.9 kcal/mol lower then in the first transfer. As such, the obtained values correspond and follow obtained data from the previous studies. Nevertheless, the energy profile corresponds to the previous study, but we observed protonated Glu98 as a proton donor for mevaldehyde, and not Lys639 (analogue to Lys 691 in *Oliveira et al.* **[31]**. Additionally, the Glu98 stabilises its negative charge through proton exchange with His405, which then becomes neutral. The Asp715 and Lys639 stay in the close proximity of 1.64 Å, but Asp767 is also stabilised through hydrogen bond interaction with NADPH hydroxyl group (1.69 Å), which places Asp767 in the centre between NADPH and Lys639. Moreover, Lys639 is 1.89 Å from the O7-mevaldehyde substrate, which is stabilised through a given proton of Glu98 (0.99 Å). Consequently, Glu98 stabilise itself through proton exchange with a His405 (1.02 Å). The new bond between NADPH and mevaldehyde, after the Hydride transfer is 1.09 Å. All these interactions support the hydride transfer and thus, lower the energy barrier for it to happen. The reaction seems to be converted, however it is possible that stabilisation of mevaldehyde's negative charge happens after the hydride transfer, which would need some extra simulations.

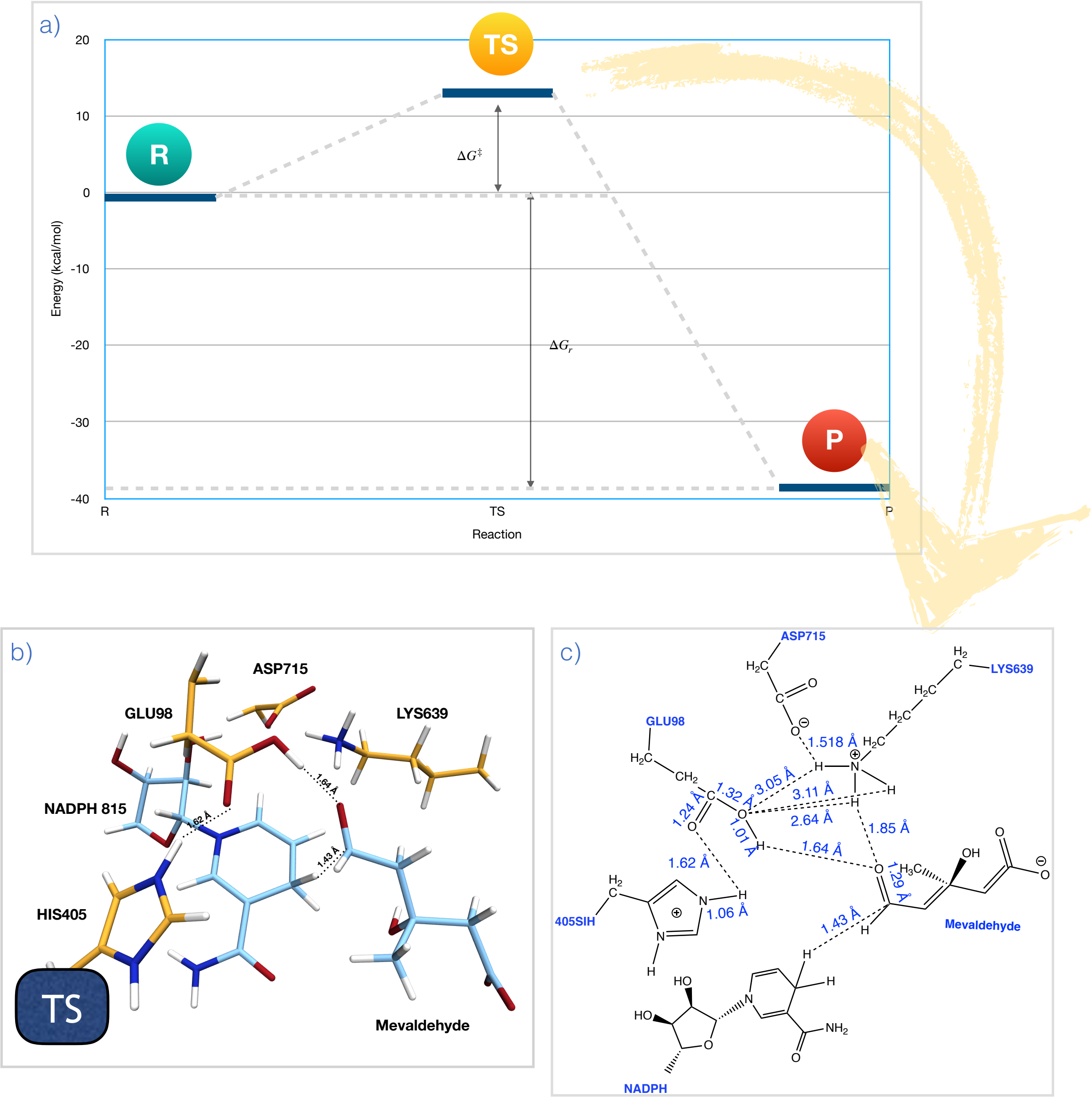

Figure 3.14

(a) Graphical representation of the activation energy (E_a) and reaction energy (E_r) after added thermal corrections.

(b) Graphical representation of the TS and corresponding distances in *Licorice* using VMD software.

(c) 2D representation of the active site of the TS structure.

Furthermore, we performed additional characterisation with the *single point* calculations using higher basis set (B3LYP:6-311G(2d,2p)) and obtained the results as shown in the **Figure 3.15**.

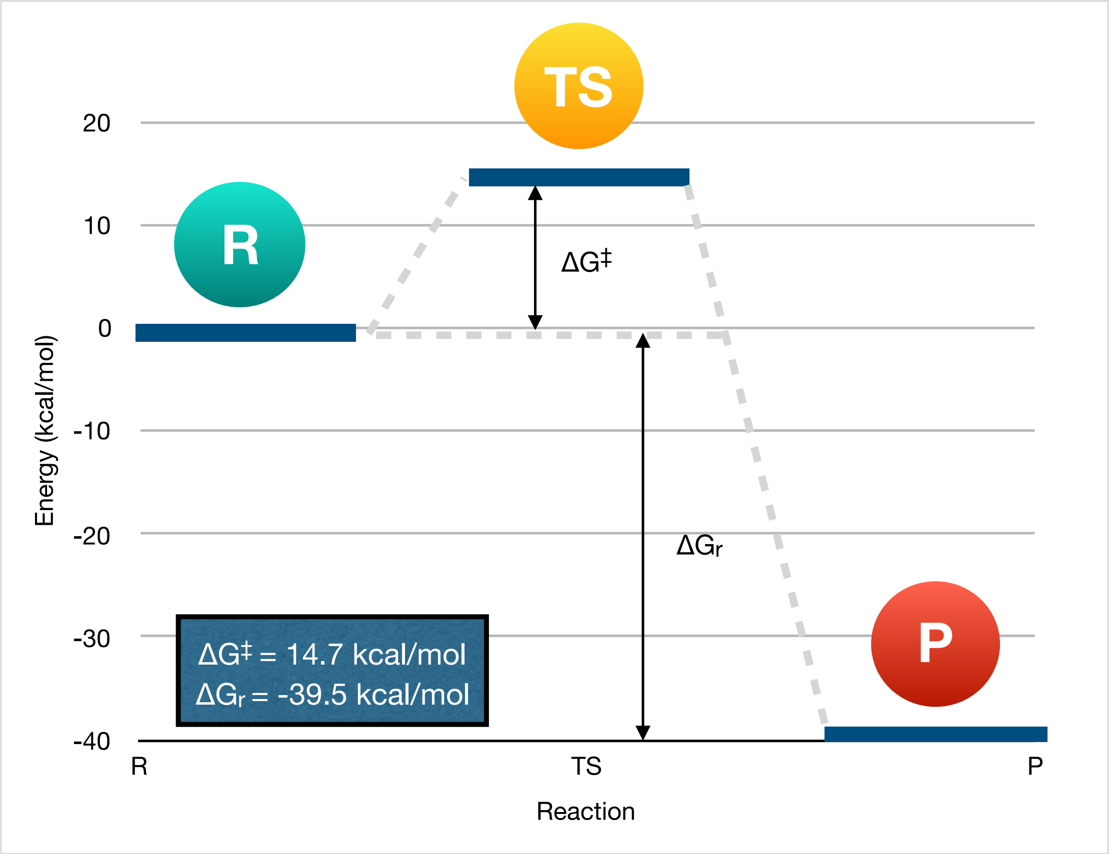

Figure 3.15 Graphical representation of the results obtained through *single point* calculations using B3LYP:6-311G(2d,2p) basis set.

Additionally, we superimposed the crystallographic structure 1DQA with the fully optimised structure of the products and obtained the RMSd 2.95 Å and 1.48 Å for the entire system and backbone of the protein, respectively. Superimposed structures are shown in the **Figure 3.16**, whereas the **Figure 3.17** represents the fully optimised structure of products with the formed bonds between hydride and mevaldehyde, which now corresponds to mevalonate, and rest catalytic residues.

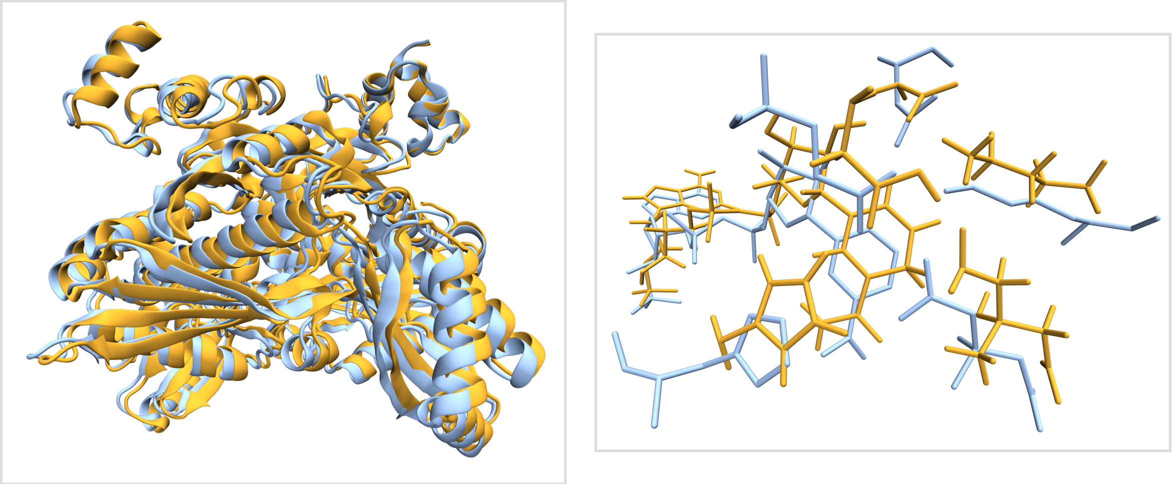

Figure 3.16 (a) Graphical representation in *NewCartoon* of the superimposed crystallographic structure (PDB ID: 1DQA) and fully optimised structure of products.

(b) Graphical representation of the active site of the crystallographic structure (PDB ID: 1DQA) and fully optimised structure of products in *Licorice* using VMD software.

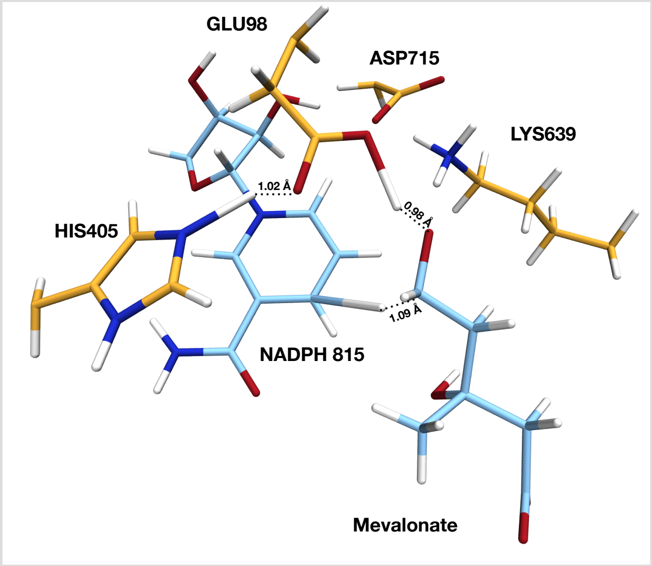

Figure 3.17 Graphical representation of the active site obtained through fully optimised products' structure in *Licorice* using VMD software.

3.3.1.2 The Second Model - Protonated Glu98 And Lys639, Protonated His405 and Deprotonated Asp715

In the second model, His405 was not cationic, while all the rest catalytic residues stayed in the same protonation states (**Figure 3.18**). The ONIOM HL included 91 atoms, whereas charge of the HL and the LL were -5 and -1, respectively. According to the most literature, this model should be the most favourable, but this would require additional characterisation of the transition state. Due to major movements of His405 we did not manage to fully optimise the TS of the second model. However, it is not possible to state anything as this would require TS characterisation.

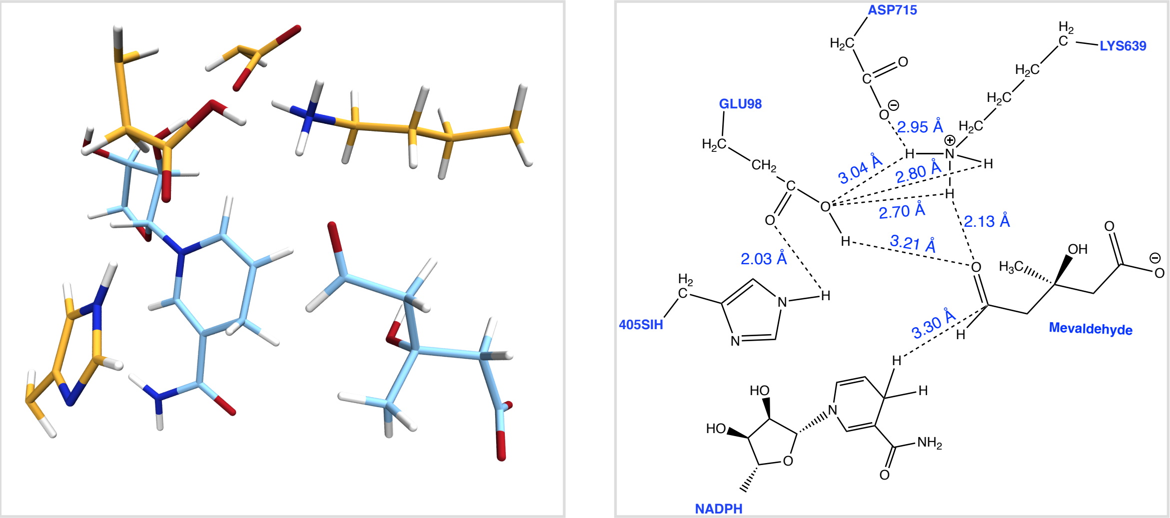

Figure 3.18 Graphical representation of the active site obtained from the optimised reactants' structure in *Licorice* using VMD software and ChemDraw.

As shown in **Figure 3.19** activation barrier is approximately the same as in the first model, 15.8 kcal/mol, but this is just an estimated value through *scan* calculations and data obtained through optimisation of the reactants and products. Moreover, this model implies that His405 protonates Glu98, which then protonates Lys639 in the step before second hydride transfer.

a)

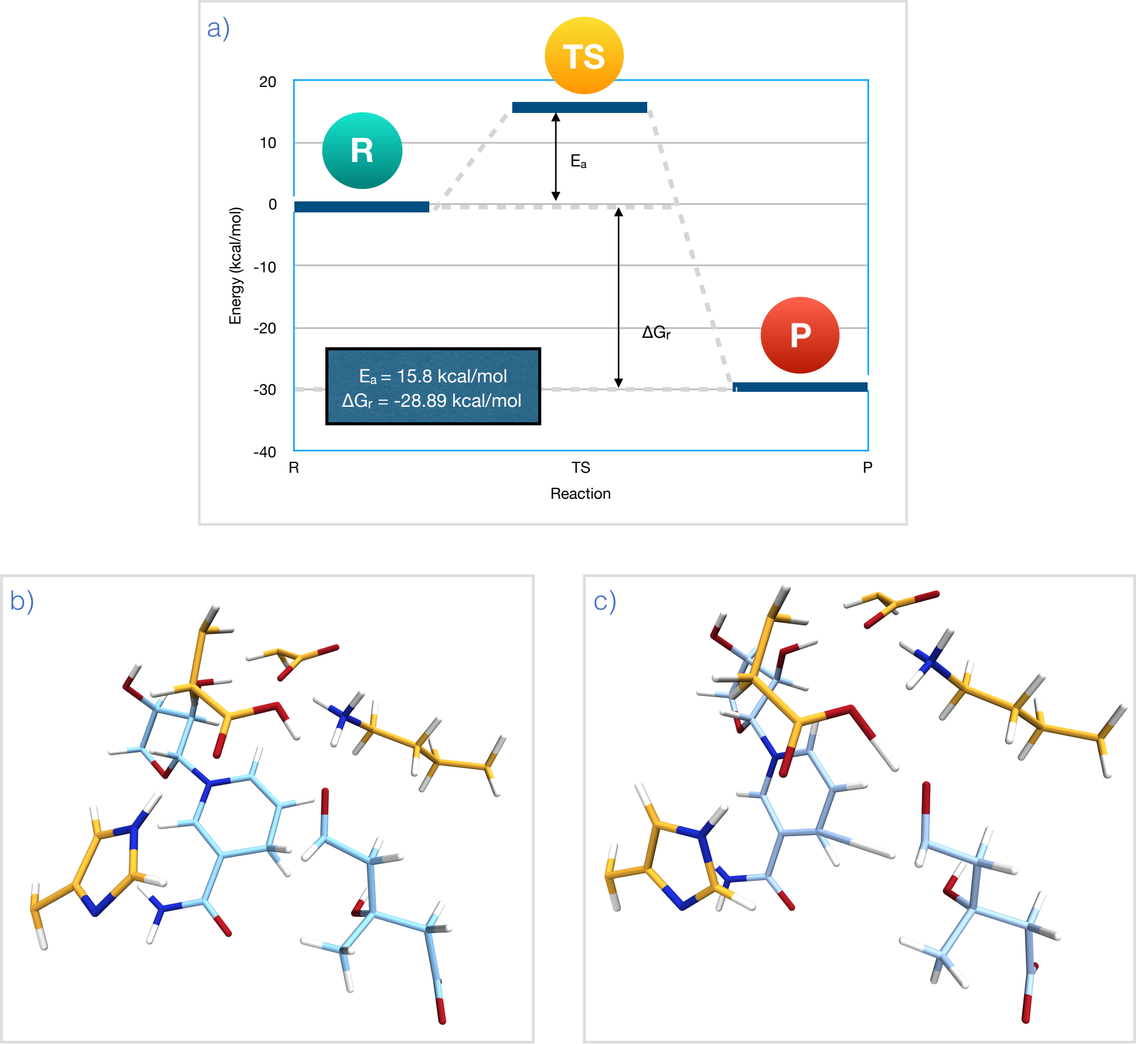

Figure 3.19

(a) Graphical representation of the obtained results from the *scan* calculations (for TS), whereas the data for the reactants and products were obtained from geometry optimisation calculations.

(b)Graphical representation of the TS's structure for the second model that is not fully characterised nor optimised in *Licorice* using VMD software. The structure is taken from the highest peak of the *scan* calculations.

(c)Graphical representation of the products' structure for the second model in *Licorice* using VMD software.

Besides data from the *scan* calculations we fully characterised the reactants and products. Additionally, we estimated the RMSd values of 3.27 Å and 2.04 Å from entire system and backbone of the protein, respectively (**Figure 3.20**).

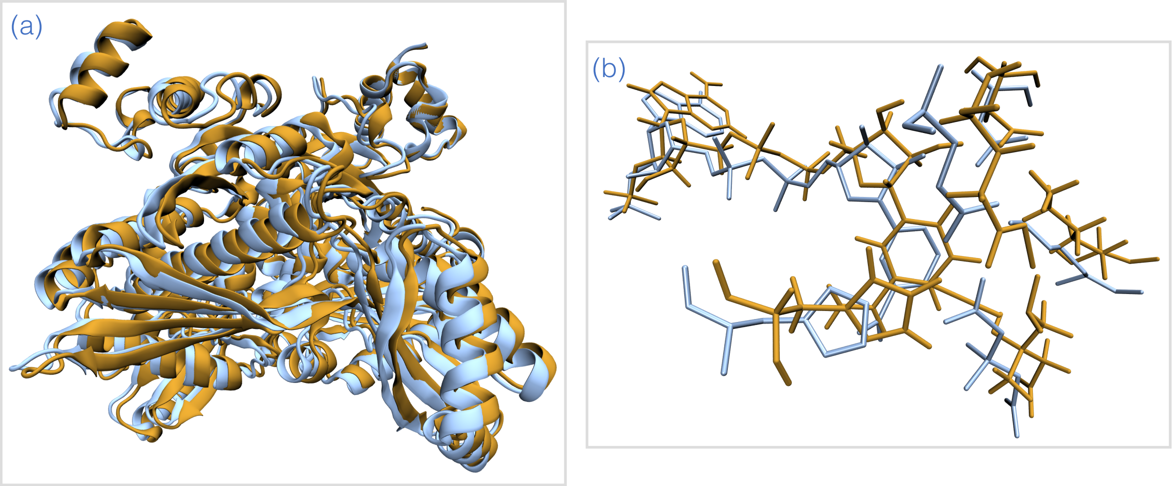

Figure 3.20

(a) Graphical representation in *NewCartoon* of the superimposed crystallographic structure (PDB ID: 1DQA) and fully optimised structure of products.

(b) Graphical representation of the active site of the crystallographic structure (PDB ID: 1DQA) and fully optimised structure of products in *Licorice* using VMD software.

3.3.1.3 The Third Model - Protonated Glu98, Double-Protonated His405 and Deprotonated Lys639 And Asp715

In the third model, Lys639 and Asp715 are deprotonated, whereas Glu98 and His405 are protonated and double-protonated (cationic), respectively. We expected for this model to be the least favourable as there are two negative charges in the close proximity without positive charge of Lys639 to stabilise that negative charge (**Figure 3.21**). The HL included 91 atoms and the only difference in this model is protonation state of Lys639. This model is a follow up from the first hydride transfer fully characterised by *Oliveira et al*. **[31]** It implies that the protonation states are as those ones in products of the first hydride transfer, and that the mechanism is continuing. It also implies that the second model goes through this phase first until Glu98 protonates Lys639, after a proton transfer from His405. This phase would be really fast and would not affect the total energy barrier.

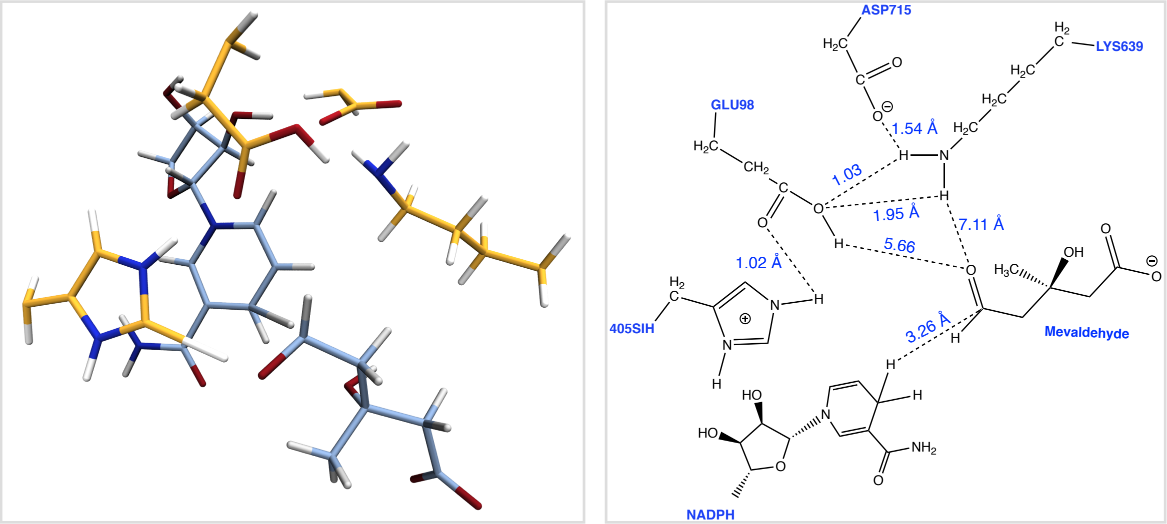

Figure 3.21 Graphical representation of the active site obtained from the optimised reactants' structure in *Licorice* using VMD software and ChemDraw.

The **Figure 3.22** represents rough approximation (*scan)* of the reaction energies. Although, there were some fluctuations in the HL and LL region, the maximum total energy value (*red*) was less then 20 kcal/mol.

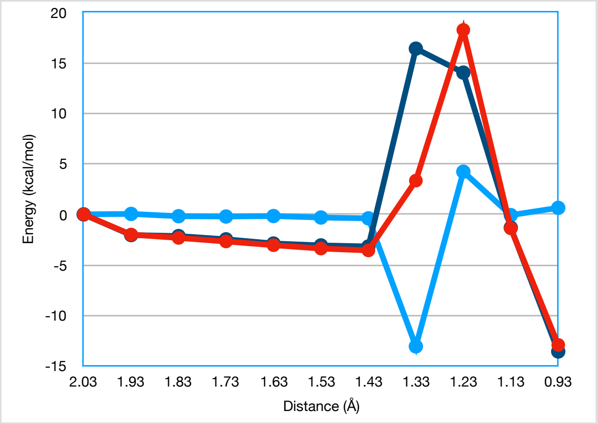

Figure 3.22 Graphical representation of the *scan* with total energy (red), HL energy (dark blue) and LL energy (bright blue).

As shown in **Figure 3.23**, the maximum value of the total energy was ~18.2 kcal/mol. However, to get the exact value of the Gibbs activation and reaction energy we would have to fully characterise all three structures. We extracted that structure for geometry optimisation. However, after the full characterisation of the reactants and products, we were able to estimate the Gibbs free reaction energy, as well as the activation energy barrier through *scan*. The barrier is extremely high and therefore this reaction cannot occurs in the human body. The activation barrier is approximately 69.2 kcal/mol, whereas the Gibbs free reaction energy is 47 kcal/mol. Thus, the reaction would be endorgenic.

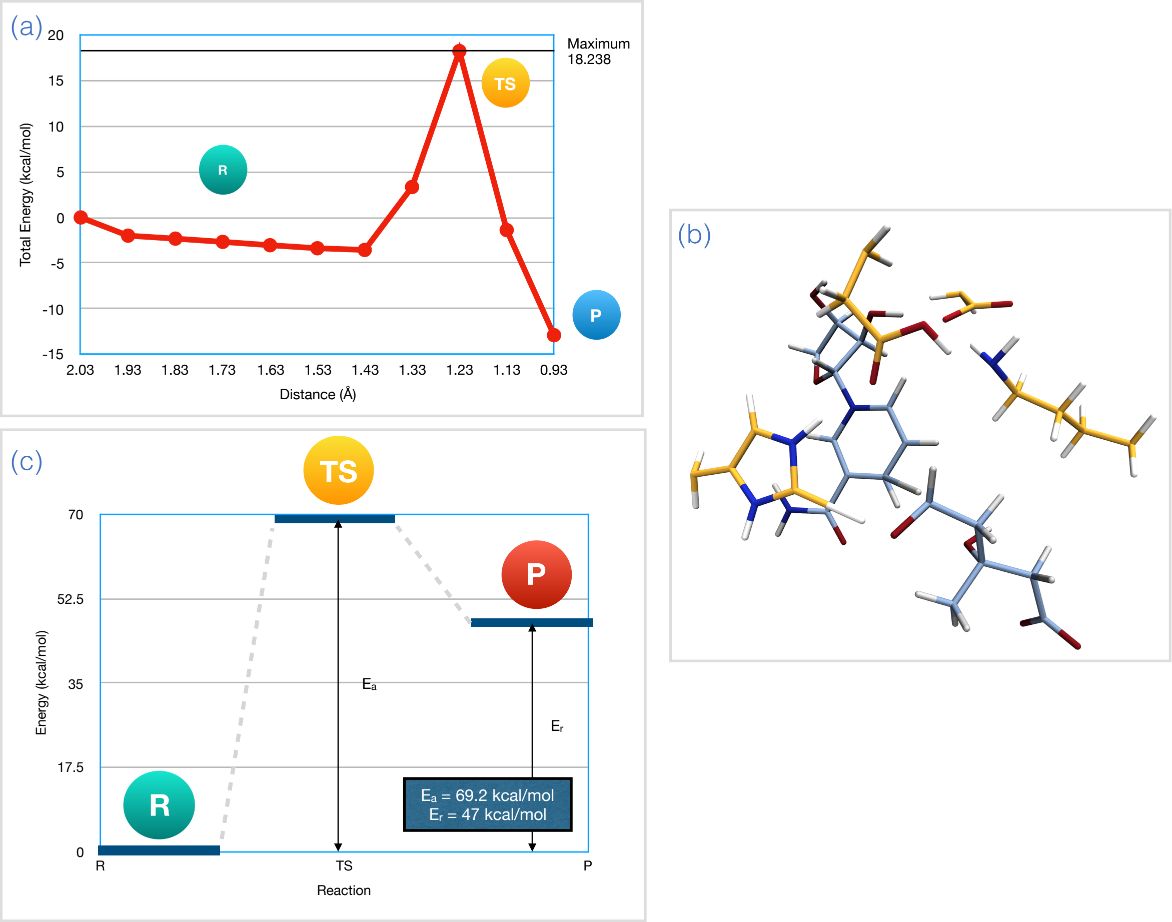

Figure 3.23

(a) Graphical representation of the total energy (kcal/mol) for entire system showing maximum value, which corresponds to the transition state structure.

(b) Graphical representation of the active site obtained from the optimised products structure in *Licorice* using VMD software.

(c) Graphical representation of the energy profile for the third model.

Moreover, the resulting optimised structure of the products shows the unusual final *zwitterion* structure of the His405 (**Figure 3.24**), as a consequence of the proton exchange between C-atom of His405 and mevaldehyde. As Lys639 is neutral, this model would have to get additional penalty on the total ΔG as this state corresponds to the lysine at the pH~10.5, while all the calculations were performed at the pH 7.5. Thus, this implies 3 pK_a difference between these two pH states. Correspondingly, for each pK_a unit 1.4 kcal/mol is added to the final result, which means that the final ΔG would be 4.2 kcal/mol higher then the estimated value through simulations.

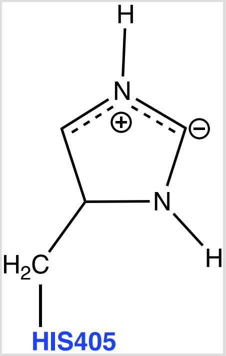

Figure 3.24 Structure of the unusual *zwitterion* His405 structure obtained through optimised structure of products.

Correspondingly, the RMSd values were estimated for both entire system and backbone of the protein, of 3.17 Å and 1.87 Å And, respectively, thus the superimposed structures are shown in the **Figure 3.25**.

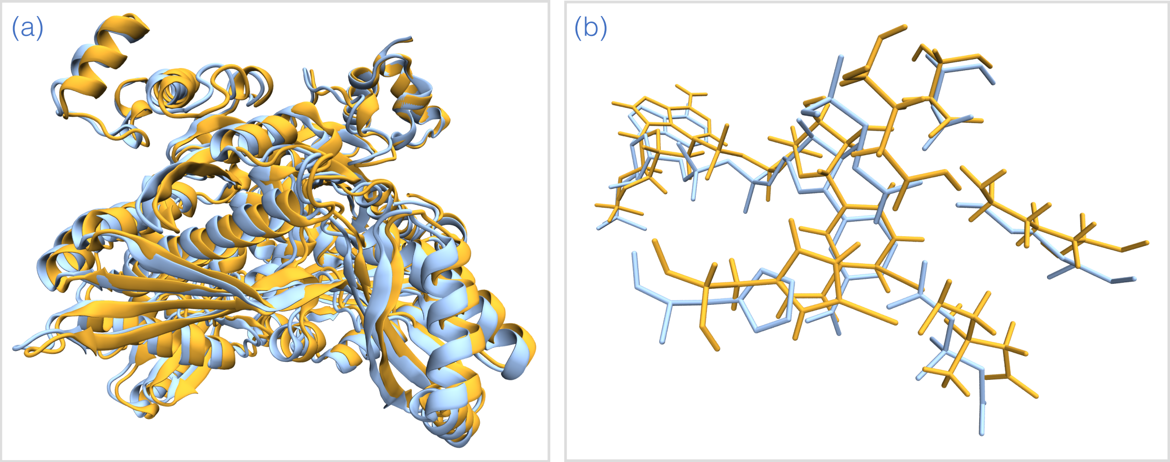

Figure 3.25

(a) Graphical representation in *NewCartoon* of the superimposed crystallographic structure (PDB ID: 1DQA) and fully optimised structure of products.

(b) Graphical representation of the active site of the crystallographic structure (PDB ID: 1DQA) and fully optimised structure of products in *Licorice* using VMD software.

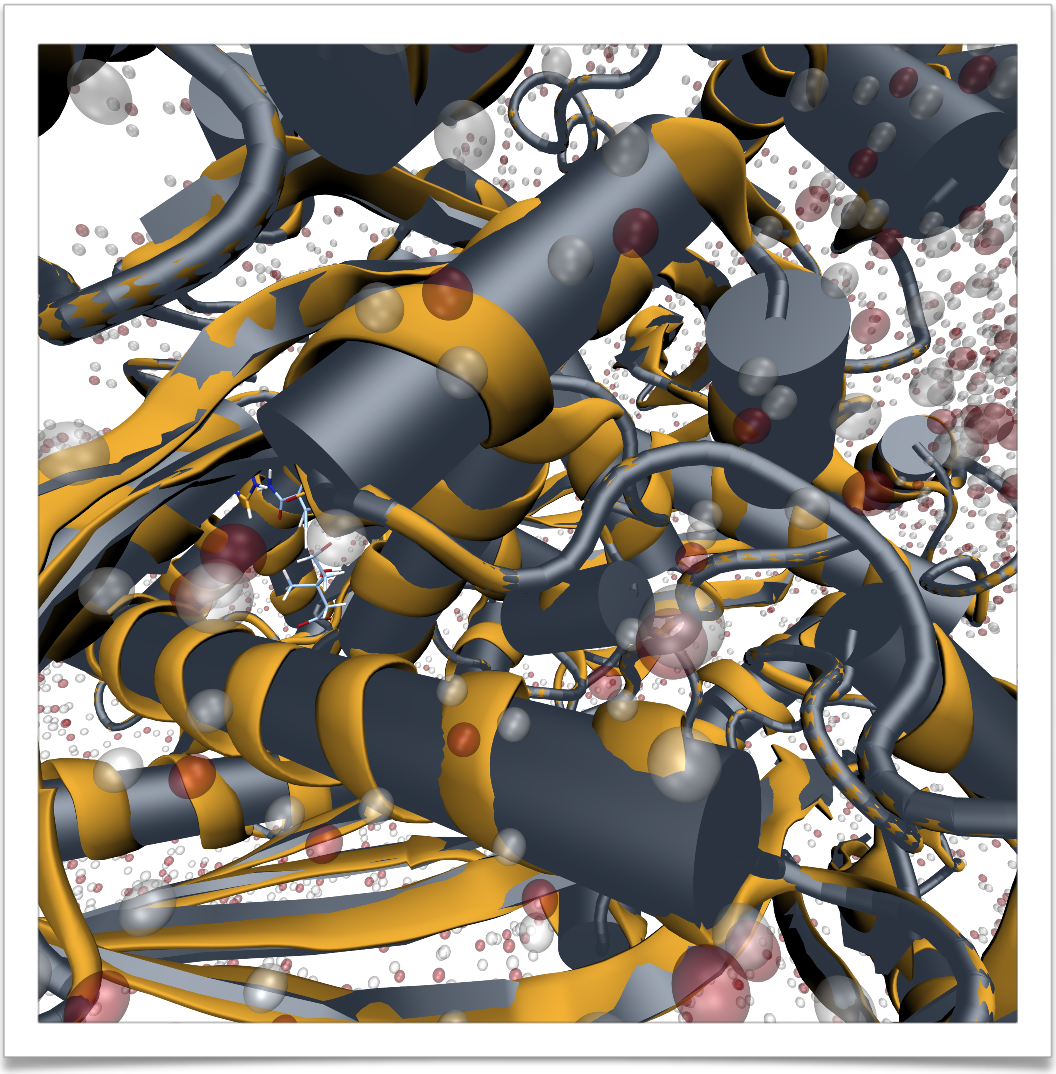

Chapter 4 - Conclusions

In this study, we studied three different model proposals for the catalytic mechanism of a human HMGCR with various protonation states. Firstly, we found the adequate crystallographic structure (1DQA) that had all needed substrates and cofactor to study this mechanism. All external molecules were parametrised using Antechamber, with RESP charges determined at the Hartree-Fock level (HF: 6-31G(d)) after which we studied conformational changes in the system using MD simulations (minimisation, equilibration and production phase). Consequently, the structure with the most favourable and optimal geometry between the mevaldehyde substrate, NADPH cofactor and catalytic residues, was used for all later calculations as a starting point. We studied this mechanism with the QM/MM (ONIOM) method where we partitioned the system in two layers. The high layer was treated with quantum mechanics approach using DFT:B3LYP/6-311G(d) method, while the low layer was treated with molecular mechanics using the AMBER force filed. After obtaining the structure from the MD simulations, we prepared the ONIOM model and optimised the initial structure. Furthermore, we obtained a TS structure through linear transit *scan* calculations, which we confirmed through nuclear Hamiltonian calculations after geometry optimisation. The confirmation of the TS as having one imaginary frequency in the nuclear Hamiltonian (*frequency)* calculations was performed. Correspondingly, we optimised the reactants and products, and confirmed them through *frequency* calculations which have to be all positive. Lastly, we performed *single point* calculations with a higher basis set DFT:B3LYP/6-311G(2d,2p) to get the better estimated Gibbs free activation and reaction energies.

Our calculations were based on the previous *Oliveira et. al's* **[31]** study as they fully the first hydride transfer, which is also the rate-limiting step. The first model we tested included protonated Glu98 and Lys639, deprotonated Asp715 and cationic His405. The second model included neutral His405 in the HL, and it is actually the following step after the continuous reaction mechanism where Lys639 is deprotonated, which was the third model we tested.

Although we did not succeed in optimising the second model, the final result of the first model (**Figure 4.1**) with protonated Lys639 and Glu98, cationic His405 and deprotonated Asp715, follows the data from the previous studies of *Oliveira et al*. **[31]** and *Haines at al*. **[3, 8]** in terms of energy. Notwithstanding the fact that *Oliveira et al*. **[31]** proposed Lys691 as a proton donor (analogue to Lys639 in this study), and not Glu98, it follows the study of *Haines et al*. **[3, 8]**, but in deprotonated protonation state. We assume it is due to the class-difference between prokaryotic and human enzyme. **[3, 8]** Furthermore, we superimposed optimised structure of the products with initial crystallographic structure PDB ID:1DQA, and obtained RMSd of 2.95 Å for entire system, as well as 1.48 Å RMSd for the backbone of the protein.

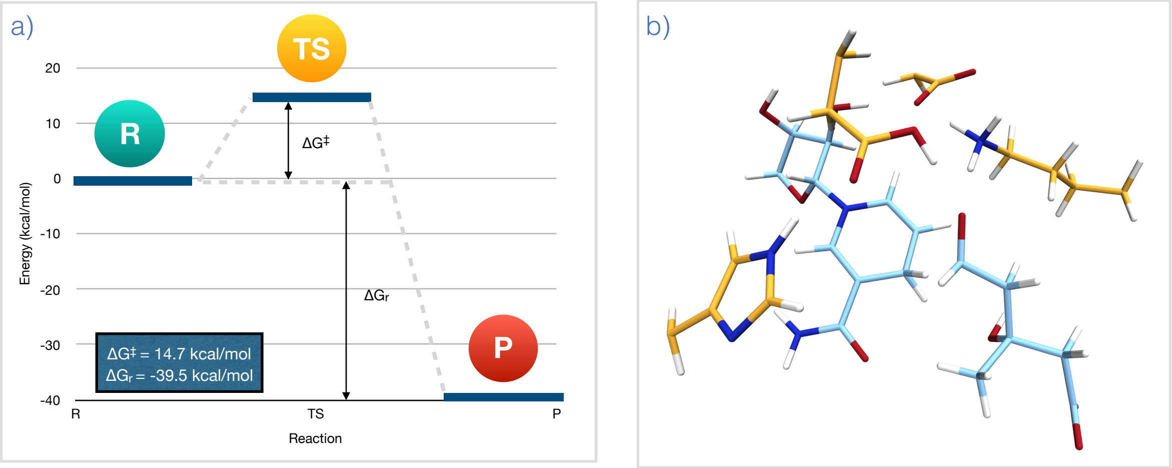

Figure 4.1

(a)The final results for the first model obtained through *single point* calculations with B3LYP: 6-311G(2d,2p) basis set.

(b)The optimised TS structure in *Licorice* using VMD software.

Moreover, after the hydride transfer from NADPH to mevaldehyde, Glu98 protonates the substrate to obtain the final mevalonate product. Consequently, His405 transfers its proton to Glu98, thus stabilising its negative charge. It is also possible that the proton exchange from the Glu98 and mevaldehyde intermediate occurs in the second step, however that would reacquire additional modelling and calculations. This hypothesis is based on the constant charge on the oxygen of the mevaldehyde in the TS and products' structures. There is no decrease nor increase in punctual Muliken charges.

The final proposed catalytic mechanism is shown in the **Figure 4.2** with the corresponding Gibbs free activation energy of 15 kcal/mol. However, from the *scan* calculations and obtained Gibbs free reaction energies for other two models it is obvious that the second model is the preferred one. This would mean that the second model actually goes through one additional step where Glu98 protonates neutral Lys639 after the first hybrid transfer. This is reasonable as Glu98 would be much more acidic then the neutral Lys639. To see whether the reaction is indeed really concerted, we would have to perform some additional calculations.

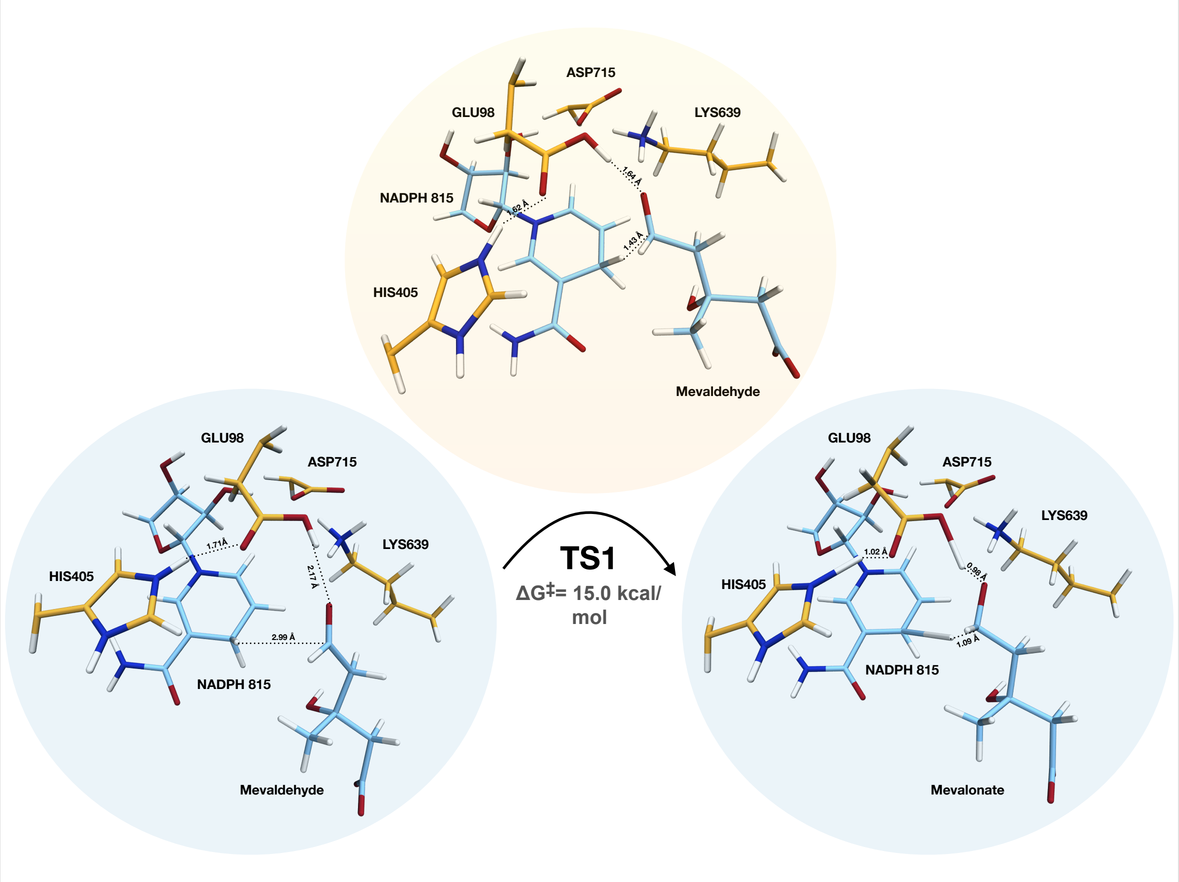

Figure 4.2 The new proposed mechanism for the second hydride transfer of the human HMGR.

Moreover, through third model it is easy to see how Lys639 is important for this reaction. Not only that Lys639 acts like a general acid in the first hydride transfer **[31]**, but it also anchored the substrate in the favourable conformation. Also, it lowers the pK_a, thus the Glu98 easily transfers its proton to the substrate.

The obtained results of the *single point* calculations (14.7 kcal/mol) for the first model have been compared with two other models in **Figure 4.3**. However, activation barrier of the second model is rough approximation from the obtained results of the *scan* and geometry optimisation of the reactants and products (15.76 kcal/mol). This result would change after optimisation of the TS, as well as after *single point* calculations. The highest obtained barrier was for the third model, as there was no protonated Lys639 to anchor the substrate and to lower the pK_a (69.22 kcal/mol).

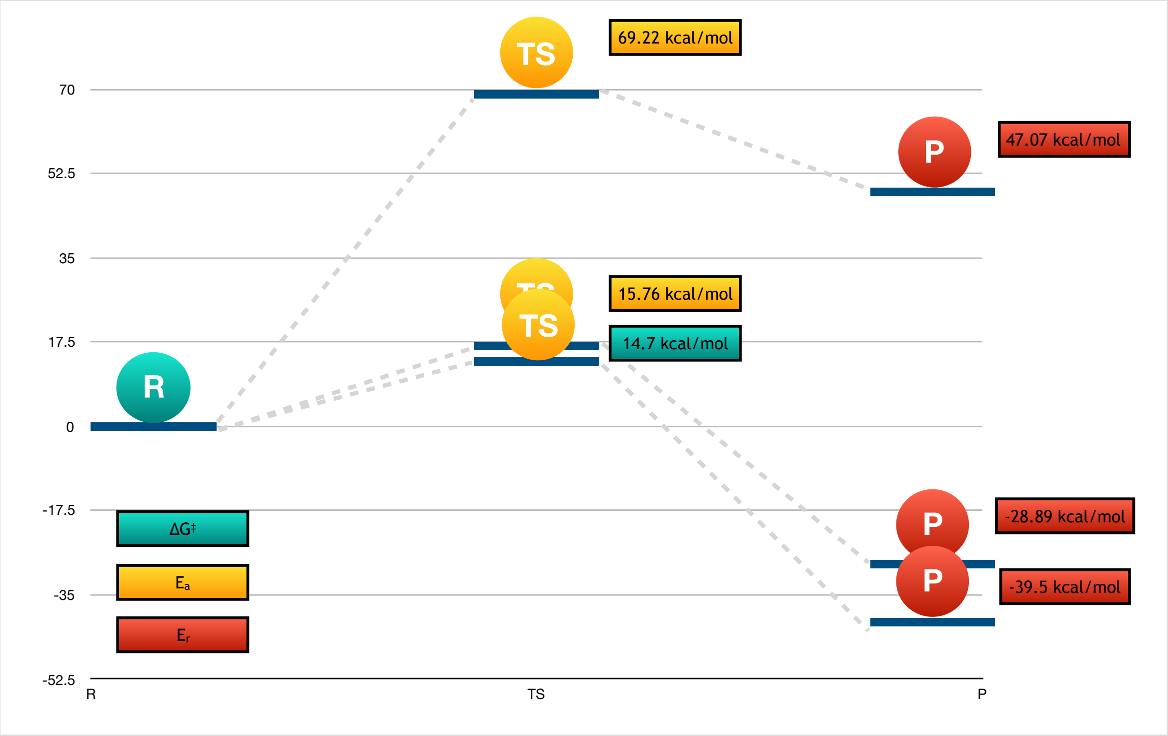

Figure 4.3 The comparison of tested models and obtained activation barriers and reaction energies.

Bibliography

1. Friesen, J. A. Rodwell, V. W., The 3-hydroxy-3-methylglutaryl coenzyme-A (HMG-CoA) reductases, *Genome Biology 2004, 5(11):248, doi: 10.1186/gb-2004-5-11-248*
2. Istvan, E. S., Palnitkar M., Buchanan, S.K. and Deisenhofer, J., Crystal structure of the catalytic portion of human HMG-CoA reductase: insights into regulation of activity and catalysis, The European Molecular Biology Organization, 2000, *Vol.19 No.5 pp.819–830*
3. Haines, B. E., Steussy, C. N., Stauffacher, C. V. and Wiest, O., Molecular Modeling of the Reaction Pathway and Hydride Transfer Reactions of HMG-CoA Reductase, *Biochemistry*, 2012, *51* (40), pp 7983–7995, doi**:** 10.1021/bi3008593
4. Medina, M. W. and Krauss, R. M., The role of HMGCR alternative splicing in statin efficacy, *Trends Cardiovasc Med.,* 2009 Jul; 19(5): 173–177, doi: 10.1016/j.tcm.2009.10.003
5. Nelson, D.L., Lehninger, A. L. and Cox, M. M., Lehninger Principles of Biochemistry, W. H. Freeman, 2008, 5th Edition
6. Suganya, S., Nandagopal, B., Anbarasu A., Natural Inhibitors of HMG-CoA Reductase-An Insilico Approach Through Molecular Docking and Simulation Studies, *J Cell Biochem*. 2017, 118(1):52-57. doi: 10.1002/jcb.25608
7. Gesto, D. S., Cerqueira ,N. M., Ramos, M. J., Fernandes, P. A., Discovery of new druggable sites in the anti-cholesterol target HMG-CoA reductase by computational alanine scanning mutagenesis, J Mol Model., 2014, 20(4):2178. doi: 10.1007/s00894-014-2178-8
8. Haines, B. E., Wiest, O. And Stauffacher, C. V., The Increasingly Complex Mechanism of HMG-CoA Reductase, Acc Chem Res., 2013, 19; 46(11): 2416–2426, doi: 10.1021/ar3003267
9. Bochar, D.A., Stauffacher, C. V., Rodwell, V. W., Sequence comparisons reveal two classes of 3-hydroxy-3-methylglutaryl coenzyme A reductase, Mol Genet Metab., 1999, 66(2):122-7, doi: 10.1006/mgme.1998.2786
10. Istvan, E. S., Deisenhofer J., Structural mechanism for statin inhibition of HMG-CoA reductase, Science. 2001, 292(5519):1160-4, doi: 10.1126/science.1059344
11. Steussy, C.; Critchelow, C.; Schmidt, T.; Min, J.-K.; Wrensford, L.; Burgner, J.; Rodwell, V.; Stauffacher, C. V. A novel role for CoA during hydride transfer in 3-hydroxy-3- methylglutaryl-coenzyme A reductase Biochemistry 2013, 52, doi: 10.1021/bi400335g
12. Tabernero, L.; Bochar, D. A.; Rodwell, V. W.; Stauffacher, C. V. Substrate-Induced Closure of the Flap Domain in the Ternary Complex Structures Provides Insights into the Mechanism of Catalysis by 3-hydroxy-3-methylglutaryl-CoA Reductase. Proc. Natl. Acad. Sci. U.S.A. 1999, 96, 7167–7171.
13. Frimpong, K.; Rodwell, V. W. Catalysis by Syrian-Hamster 3-Hydroxy-3-Methylglutaryl-Coenzyme-A Reductase: Proposed Roles of Histidine-865, Glutamate-558, and Aspartate-766. J. Biol. Chem. 1994, 269, 11478–11483.
14. Brown, M. S.; Goldstein, J. L. A Receptor-Mediated Pathway for Cholesterol Homeostasis. Science 1986, 232, 34–47.

15. Bensch, W. R.; Rodwell, V. W. Purification and Properties of 3-Hydroxy-3- Methylglutaryl Coenzyme-A Reductase from Pseudomonas. J. Biol. Chem. 1970, 245, 3755–3762.
16. Durr, I. F.; Rudney, H. Reduction of Beta-Hydroxy-Beta-Methylglutaryl Coenzyme-A to Mevalonic Acid. J. Biol. Chem. 1960, 235, 2572–2578.
17. Knappe, J.; Ringelmann, E.; Lynen, F. Uber Die Beta-Hydroxy-Beta-Methyl-Glutaryl-Reduktase Der Hefe: Zur Biosynthese Der Terpene 0.9. Biochem. Z. 1959, 332, 195–213.
18. Qureshi, N.; Dugan, R. E.; Cleland, W. W.; Porter, J. W. Kinetic-Analysis of Individual Reductive Steps Catalyzed by Beta-Hydroxy-Beta-Methylglutaryl-Coenzyme A Reductase Obtained from Yeast. Biochemistry 1976, 15, 4191–4197.
19. Retey, J.; Stetten, E. V.; Coy, U.; Lynen, F. A Probable Intermediate in Enzymic Reduction of 3-Hydroxy-3-Methylglutaryl Coenzyme-A. Eur. J. Biochem. 1970, 15, 72–76.
20. Lawrence, C. M.; Chi, Y. I.; Rodwell, V. W.; Stauffacher, C. V. Crystallization of Hmg-CoA Reductase from Pseudomonas mevalonii. Acta Crystallogr., Sect. D: Biol. Crystallogr. 1995, 51, 386–389.
21. Jordan-Starck, T. C.; Rodwell, V. W. Pseudomonas mevalonii 3-Hydroxy-3-Methylglutaryl-CoA Reductase - Characterization and Chemical Modification. J. Biol. Chem. 1989, 264, 17913–17918.
22. Darnay, B. G.; Wang, Y. L.; Rodwell, V. W. Identification of the Catalytically Important Histidine of 3-Hydroxy-3-Methylglutaryl-Coenzyme-A Reductase. J. Biol. Chem. 1992, 267, 15064–15070.
23. Jordan-Starck, T. C.; Rodwell, V. W. Role of Cysteine Residues in Pseudomonas mevalonii 3-hydroxy-3-methylglutaryl-CoA Reductase. Site-directed Mutagenesis and Characteriza- tion of the Mutant Enzymes. J. Biol. Chem. 1989, 264, 17919–17923.
24. Wang, Y. L.; Darnay, B. G.; Rodwell, V. W. Identification of the Principal Catalytically Important Acidic Residue of 3-Hydroxy-3-Methylglutaryl Coenzyme-A Reductase. J. Biol. Chem. 1990, 265, 21634–21641.
25. Lawrence, C. M.; Rodwell, V. W.; Stauffacher, C. V. Crystal-Structure of Pseudomonas mevalonii Hmg-CoA Reductase at 3.0 Angstrom Resolution. Science 1995, 268, 1758–1762.
26. Istvan, E. S.; Deisenhofer, J. The Structure of the Catalytic Portion of Human HMG-CoA Reductase. Biochim. Biophys. Acta, Mol. Cell Biol. Lipids 2000, 1529, 9–18.
27. Veloso, D.; Cleland, W. W.; Porter, J. W. pH Properties and Chemical Mechanism of Action of 3-Hydroxy-3-Methylglutaryl Coenzyme-A Reductase. Biochemistry 1981, 20, 887–894.
28. Gill, J. F.; Beach, M. J.; Rodwell, V. W. Mevalonate Utilization in Pseudomonas Sp-M: Purification and Characterization of an Inducible 3-Hydroxy-3-Methylglutaryl Coenzyme-A Reductase. J. Biol. Chem. 1985, 260, 9393–9398.
29. Frimpong, K.; Rodwell, V. W. The Active-Site of Hamster 3-Hydroxy-3-Methylglutaryl-CoA Reductase Resides at the Subunit Interface and Incorporates Catalytically Essential Acidic Residues from Separate Polypeptides. J. Biol. Chem. 1994, 269, 1217–1221.

30. Wrensford, L. V.; Rodwell, V. W.; Anderson, V. E. 3-Hydroxy-3-methylglutaryldithio- Coenzyme A: A Potent Inhibitor of Pseudomonas mevalonii HMG-CoA Reductase. Biochem. Med. Metab. Biol. 1991, 45, 204–208.
31. Oliveira, E. F, Cerqueira, N. M. F. S. A., Ramos, M. J., Fernandes, P. A., QM/MM study of the mechanism of reduction of 3-hydroxy-3-methylglutaryl coenzyme A catalyzed by human HMG-CoA reductase, Catalysis Science & Technology, 2016, 6 (19): 7172-7185, doi: 10.1039/ C6CY00356G
32. Dokainish, H. M.; Gauld, J. W., Formation of a Stable Iminol Intermediate in the Redox Regulation Mechanism of Protein Tyrosine Phosphatase 1B (PTP1B), ACS Catal. 2015, 5 (4), 2195–2202.
33. Pinal-Fernandez, I., Casal-Dominguez, M., Mammen AL., Statins: pros and cons., Med Clin (Barc). 2018, 150(10):398-402. doi: 10.1016/j.medcli.2017.11.030.
34. Gupta SC, Hevia D, Patchva S, Park B, Koh W, Aggarwal BB. Upsides and downsides of reactive oxygen species for cancer: the roles of reactive oxy- gen species in tumorigenesis, prevention, and therapy. Antioxid Redox Signal. 2012;16:1295–322.
35. Strandberg TE, Vanhanen H, Tikkanen MJ. Effect of statins on C-reactive protein in patients with coronary artery disease. Lancet. 1999;353:118–9.
36. Jain MK, Ridker PM. Anti-inflammatory effects of statins: clinical evidence and basic mechanisms. Nat Rev Drug Discov. 2005;4:977–87.
37. Sahebkar A, Catena C, Ray KK, Vallejo-Vaz AJ, Reiner Zˇ, Sechi LA, et al. Impact of statin therapy on plasma levels of plasminogen activator inhibitor-1. A system- atic review and meta-analysis of randomised controlled trials. Thromb Haemost. 2016;116:162–71.
38. Stanley FM, Linder KM, Cardozo TJ. Statins increase plasminogen activator inhibitor type 1 gene transcription through a pregnane X receptor regulated element. PLOS ONE. 2015;10:e0138097.
39. Richardson K, Schoen M, French B, Umscheid CA, Mitchell MD, Arnold SE, et al. Statins and cognitive function: a systematic review. Ann Intern Med. 2013;159:688–97.
40. Sacks FM, Pfeffer MA, Moye LA, Rouleau JL, Rutherford JD, Cole TG, et al. The effect of pravastatin on coronary events after myocardial infarction in patients with average cholesterol levels. Cholesterol and Recurrent Events Trial investigators. N Engl J Med. 1996;335:1001–9.
41. Shepherd J, Blauw GJ, Murphy MB, Bollen EL, Buckley BM, Cobbe SM, et al. Pravas- tatin in elderly individuals at risk of vascular disease (PROSPER): a randomised controlled trial. Lancet. 2002;360:1623–30.
42. Pang, J.; Li, X.; Morokuma, K.; Scrutton, N. S.; Sutcliffe, M. J. J. Am. Chem. Soc. 2012, 134 (4), 2367–2377.
43. Liao, R.-Z.; Thiel, W. J. Phys. Chem. B 2013, 117 (5), 1326–1336.
44. Calixto, A. R.; Brás, N. F.; Fernandes, P. a.; Ramos, M. J. ACS Catal. 2014, 4 (11), 3869–3876.
45. Van der Kamp, M. W.; Mulholland, A. J. Biochemistry 2013, 52 (16), 2708–2728.

46. Siegbahn, P. E. M.; Himo, F. Wiley Interdiscip. Rev. Comput. Mol. Sci. 2011, 1 (3), 323–336.
47. Lind, M. E. S.; Himo, F. ACS Catal. 2014, 4 (11), 4153–4160.
48. Ribeiro, A. J. M.; Alberto, M. E.; Ramos, M. J.; Fernandes, P. A.; Russo, N. Chem. - A Eur. J. 2013, 19 (42), 14081–14089.
49. Dourado, D. F. A. R.; Fernandes, P. A.; Ramos, M. J.; Mannervik, B. Biochemistry 2013, 52 (45), 8069–8078.
50. Jensen, F., Introduction to Computational Chemistry. 2nd ed. 2007: John Wiley & Sons.
51. Cramer, C.J., Essentials of Computational Chemistry - Theories and Models. 2nd ed. 2004: John Wiley & Sons. 596.
52. Hooke, R., De Potentia Restitutiva, or of Spring. Explaining the Power of Springing Bodies, London, 1678.
53. Vanommeslaeghe, K., O. Guvench, and A.D. MacKerell, *Molecular Mechanics.* Current Pharmaceutical Design, 2014. 20(20): p. 3281-3292.
54. Leach, A., Molecular Modelling: Principles and Applications (2nd Edition). 2001: Prentice Hall.
55. Case, D.A., et al., *AMBER 12*. 2012, University of California, San Francisco.
56. Case D. A.; Darden T. A.; Cheatham T. E. III; Simmerling C. L.; Wang J.; Duke R. E.; Luo R.; Walker R. C.; Zhang W.; Merz K. M.; Roberts B.; Hayik S.; Roitberg A.; Seabra G.; Swails J.; Goetz A. W.; Kolossváry I.; Wong K. F.; Paesani F.; Vanicek J.; Wolf R. M.; Liu J. ; Wu X.; Brozell S. R.; Steinbrecher T.; Gohlke H.; Cai Q.; Ye X.; Wang J.; Hsieh M. J.; Cui G.; Roe D. R.; Mathews D. H.; Seetin M. G.; Salomon-Ferrer R.; Sagui C.; Babin V.; Luchko T.; Gusarov S.; Kovalenko A.; Kollman P. A.AMBER 12, University of California: San Francisco, 2012.
57. Wang, J., Wolf, R. M.; Caldwell, J. W.;Kollman, P. A.; Case, D. A. "Development and testing of a general AMBER force field". *Journal of Computational Chemistry*, 25, 2004, 1157-1174.
58. Brooks, B.R., et al., Charmm - a Program for Macromolecular Energy, Minimization, and Dynamics Calculations. Journal of Computational Chemistry, 1983. 4(2): p. 187-217.
59. Jorgensen, W.L. and J. Tiradorives, The Opls Potential Functions for Proteins - Energy Minimizations for Crystals of Cyclic-Peptides and Crambin. Journal of the American Chemical Society, 1988. 110(6): p. 1657-1666.
60. Christen, M., et al., The GROMOS software for biomolecular simulation: GROMOS05. Journal of Computational Chemistry, 2005. 26(16): p. 1719-1751.
61. Hornak, V., et al., Comparison of multiple Amber force fields and development of improved protein backbone parameters. Proteins, 2006. **65**(3): p. 712-25.
62. Fernandes, H. S., Computational studies addressed to Histidine decarboxylase" | Master's Thesis | UCIBIO-REQUIMTE – Departamento de Química e Bioquímica da Faculdade de Ciências da Universidade do Porto, 2016
63. Planck, M., Ueber die Elementarquanta der Materie und der Elektricität. Annalen der Physik, 1901. 309(3): p. 564-566.

64. Einstein, A., Generation and conversion of light with regard to a heuristic point of view. Annalen Der Physik, 1905. 17(6): p. 132-148.
65. Hertz, H., Ueber einen Einfluss des ultravioletten Lichtes auf die electrische Entladung. Annalen der Physik, 1887. 267(8): p. 983-1000.
66. Compton, A.H., A Quantum Theory of the Scattering of X-rays by Light Elements. Physical Review, 1923. 21(5): p. 483-502.
67. Heisenberg, W., Über den anschaulichen Inhalt der quantentheoretischen Kinematik und Mechanik. Zeitschrift für Physik. 43(3): p. 172-198.
68. Dorobantu, V., The Postulates of Quantum Mechanics. Quantum Computability, 2006. **1**: p. 1-26.
69. Nottale, L. and M.N. Celerier, Derivation of the postulates of quantum mechanics from the first principles of scale relativity. Journal of Physics a-Mathematical and Theoretical, 2007. **40**(48): p. 14471-14498.
70. Atkins, P. and R. Friedman, *Molecular Quantum Mechanics*. 4th ed. 2005: OXFORD UNIVERSITY PRESS. 573.
71. Thomas, L.H., *The calculation of atomic fields.* Mathematical Proceedings of the Cambridge Philosophical Society, 1927. **23**(05): p. 542-548.
72. Fermi, E., Un metodo statistico per la determinazione di alcune priorietà dell'atome. Rend. Accad. Naz. Lincei, 1927. **6**: p. 602–607.
73. Kohn, W. and L.J. Sham, Self-Consistent Equations Including Exchange and Correlation Effects. Physical Review, 1965. **140**(4A): p. A1133-A1138.
74. Adamo, C.; Barone, V. Exchange Functionals with Improved Long-Range Behavior and Adiabatic Connection Methods without Adjustable Parameters: The mPW and mPW1PW Models. J. Chem. Phys. 1998, 108, 664–675.
75. Perdew, J. P. Electronic Structure of Solids. Akademic Verlag: Berlin, Germany, 1991.
76. Becke, A. D. Density-Functional Exchange-Energy Approx- imation with Correct Asymptotic Behavior. Phys. Rev. A 1988, 38, 3098–3100.
77. Lee, C. T.; Yang, W. T.; Parr, R. G. Development of the Colle- Salvetti Correlation-Energy Formula into a Functional of the Electron Density. Phys. Rev. B 1988, 37, 785–789.
78. Perdew, J. P.; Burke, K.; Ernzerhof, M. Generalized Gradient Approximation Made Simple. Phys. Rev. Lett. 1996, 77, 3865–3868.
79. Perdew, J. P.; Ernzerhof, M.; Burke, K. Rationale for Mixing Exact Exchange with Density Functional Approximations. J. Chem. Phys. 1996, 105, 9982–9985.
80. Young, D., Computational Chemistry: A Practical Guide for Applying Techniques to Real World Problems. 2001: John Wiley & Sons.
81. Dapprich, S., et al., A new ONIOM implementation in Gaussian98. Part I. The calculation of energies, gradients, vibrational frequencies and electric field derivatives. Journal of Molecular Structure-Theochem, 1999. **461**: p. 1-21.
82. Frisch, M.J., et al., *Gaussian 09*. 2009, Gaussian, Inc.: Wallingford, CT, USA.

83. Gaussian 09, Revision D.01, M. J. Frisch, G. W. Trucks, H. B. Schlegel, G. E. Scuseria, M. A. Robb, J. R. Cheeseman, G. Scalmani, V. Barone, B. Mennucci, G. A. Petersson, H. Nakatsuji, M. Caricato, X. Li, H. P. Hratchian, A. F. Izmaylov, J. Bloino, G. Zheng, J. L. Sonnenberg, M. Hada, M. Ehara, K. Toyota, R. Fukuda, J. Hasegawa, M. Ishida, T. Nakajima, Y. Honda, O. Kitao, H. Nakai, T. Vreven, J. A. Montgomery, Jr., J. E. Peralta, F. Ogliaro, M. Bearpark, J. J. Heyd, E. Brothers, K. N. Kudin, V. N. Staroverov, T. Keith, R. Kobayashi, J. Normand, K. Raghavachari, A. Rendell, J. C. Burant, S. S. Iyengar, J. Tomasi, M. Cossi, N. Rega, J. M. Millam, M. Klene, J. E. Knox, J. B. Cross, V. Bakken, C. Adamo, J. Jaramillo, R. Gomperts, R. E. Stratmann, O. Yazyev, A. J. Austin, R. Cammi, C. Pomelli, J. W. Ochterski, R. L. Martin, K. Morokuma, V. G. Zakrzewski, G. A. Voth, P. Salvador, J. J. Dannenberg, S. Dapprich, A. D. Daniels, O. Farkas, J. B. Foresman, J. V. Ortiz, J. Cioslowski, and D. J. Fox, Gaussian, Inc., Wallingford CT, 2013.
84. Mahoney, M.W. and W.L. Jorgensen, A five-site model for liquid water and the reproduction of the density anomaly by rigid, nonpolarizable potential functions. The Journal of Chemical Physics, 2000. **112**(20): p. 8910-8922.
85. Humphrey, W., Dalke, A. and Schulten, K., "VMD - Visual Molecular Dynamics", J. Molec. Graphics, 1996, vol. 14, pp. 33-38.
86. Holmberg, N., Ryde, U. and Bulow, L., Redesign of the coenzyme specificity in L-lactate dehydrogenase from Bacillus stearothermophilus using site-directed mutagenesis and media engineering., Prot. Engin., 12 (1999) 851-856.
87. Wang, J., Wang, W., Kollman P. A., Case, D. A. "Automatic atom type and bond type perception in molecular mechanical calculations". Journal of Molecular Graphics and Modelling , 25, 2006, 247260.
88. Larini, L., R. Mannella, and D. Leporini, Langevin stabilization of molecular- dynamics simulations of polymers by means of quasisymplectic algorithms. J.Chem Phys, 2007. **126**(10): p. 104101.
89. Roe, D.R. and T.E. Cheatham, 3rd, PTRAJ and CPPTRAJ: Software for Processing and Analysis of Molecular Dynamics Trajectory Data. J Chem Theory Comput, 2013. **9**(7): p. 3084-95.
90. Fernandes, H.S, Ramos, M. J., N. M. F. S. A., A VMD plugin to handle QM and ONIOM calculations using the gaussian software, Cerqueira, J. Comput. Chem., (2018) doi.org/10.1002/jcc.25189
91. Cisneros, G. A.; Piquemal, J.-P.; Darden, T. A., Quantum Mechanics/Molecular Mechanics Electrostatic Embedding with Continuous and Discrete Functions. The journal of physical chemistry. B 2006, 110 (28), 13682-13684. dx.doi.org/10.1021/jp062768x
92. Vreven, T.; Byun, K. S.; Komáromi, I.; Dapprich, S.; Montgomery, J. A.; Morokuma, K.; Frisch, M. J., Combining Quantum Mechanics Methods with Molecular Mechanics Methods in ONIOM. Journal of Chemical Theory and Computation 2006, 2 (3), 815-826. dx.doi.org/10.1021/ct050289g

93. Cisneros, G. A.; Piquemal, J.-P.; Darden, T. A., Quantum Mechanics/Molecular Mechanics Electrostatic Embedding with Continuous and Discrete Functions. The journal of physical chemistry. B 2006, 110 (28), 13682-13684. http://dx.doi.org/10.1021/jp062768x
94. Vreven, T.; Byun, K. S.; Komáromi, I.; Dapprich, S.; Montgomery, J. A.; Morokuma, K.; Frisch, M. J., Combining Quantum Mechanics Methods with Molecular Mechanics Methods in ONIOM. Journal of Chemical Theory and Computation 2006, 2 (3), 815-826.
95. Vreven, T. and Morokuma, K., "Chapter 3 Hybrid Methods: Oniom(Qm:Mm) and Qm/Mm." In Annual Reports in Computational Chemistry, edited by C. Spellmeyer David, vol Volume 2, 35-51: Elsevier, 2006.
96. Clemente, Fernando R., Thom Vreven, and Michael J. Frisch. "Getting the Most out of Oniom: Guidelines and Pitfalls." In Quantum Biochemistry, 61-83: Wiley-VCH Verlag GmbH & Co. KGaA, 2010.
97. Orozco, Modesto, Ivan Marchán, Ignacio Soteras, Thom Vreven, Keiji Morokuma, Kurt V. Mikkelsen, Alberto Milani, Matteo Tommasini, Mirella Del Zoppo, Chiara Castiglioni, Manuel A. Aguilar, Maria L. Sánchez, M. Elena Martín, Ignacio Fdez Galván, and Hirofumi Sato. "Beyond the Continuum Approach." In Continuum Solvation Models in Chemical Physics, 499-605: John Wiley & Sons, Ltd, 2007.
98. Vreven, Thom, K. Suzie Byun, István Komáromi, Stefan Dapprich, John A. Montgomery, Keiji Morokuma, and Michael J. Frisch. "Combining Quantum Mechanics Methods with Molecular Mechanics Methods in Oniom." Journal of Chemical Theory and Computation 2, no. 3 (2006/05/09 2006): 815-26. doi.org/10.1021/ct050289g
99. Humbel, Stéphane, Stefan Sieber, and Keiji Morokuma. "The Imomo Method: Integration of Different Levels of Molecular Orbital Approximations for Geometry Optimization of Large Systems: Test for N-Butane Conformation and Sn2 Reaction: Rcl+Cl−." The Journal of Chemical Physics 105, no. 5 (1996): 1959-67. doi.org/10.1063/1.472065
100. Svensson, Mats, Stéphane Humbel, Robert D. J. Froese, Toshiaki Matsubara, Stefan Sieber, and Keiji Morokuma. "Oniom: A Multilayered Integrated Mo + Mm Method for Geometry Optimizations and Single Point Energy Predictions. A Test for Diels−Alder Reactions and Pt(P(T-Bu)3)2 + H2 Oxidative Addition." The Journal of Physical Chemistry 100, no. 50 (1996/01/01 1996): 19357-63. doi.org/10.1021/jp962071j
101. Maseras, Feliu and Keiji Morokuma. "Imomm: A New Integrated Ab Initio + Molecular Mechanics Geometry Optimization Scheme of Equilibrium Structures and Transition States." Journal of Computational Chemistry 16, no. 9 (1995): 1170-79. doi.org/10.1002/jcc.540160911
102. Matsubara, Toshiaki, Stefan Sieber, and Keiji Morokuma. "A Test of the New “Integrated Mo + Mm” (Imomm) Method for the Conformational Energy of Ethane and N-Butane." International Journal of Quantum Chemistry 60, no. 6 (1996): 1101-09. doi.org/10.1002/(SICI)1097-461X(1996)60:6<1101::AID-QUA1>3.0.CO;2-3

103.Vreven, Thom and Keiji Morokuma. "On the Application of the Imomo (Integrated Molecular Orbital + Molecular Orbital) Method." Journal of Computational Chemistry 21, no. 16 (2000): 1419-32. doi.org/10.1002/1096-987X(200012)21:16<1419::AID-JCC1>3.0.CO;2-C

104.A.D. Becke, J.Chem.Phys. 98 (1993) 5648-565 doi.org/10.1063/1.464913

105.C. Lee, W. Yang, R.G. Parr, Phys. Rev. B 37 (1988) 785-789 doi.org/10.1103/PhysRevB.37.785

106.S.H. Vosko, L. Wilk, M. Nusair, Can. J. Phys. 58 (1980) 1200-1211 doi.org/10.1139/p80-159

107.P.J. Stephens, F.J. Devlin, C.F. Chabalowski, M.J. Frisch, J.Phys.Chem. 98 (1994) 11623-11627 doi.org/10.1021/j100096a001

108.R. Ditchfield, W. J. Hehre, and J. A. Pople, “Self-Consistent Molecular Orbital Methods. 9. Extended Gaussian-type basis for molecular-orbital studies of organic molecules,” J. Chem. Phys., 54 (1971) 724. http://dx.doi.org/10.1063/1.1674902

109.W. J. Hehre, R. Ditchfield, and J. A. Pople, “Self-Consistent Molecular Orbital Methods. 12. Further extensions of Gaussian-type basis sets for use in molecular-orbital studies of organic-molecules,” J. Chem. Phys., 56 (1972) 2257 http://dx.doi.org/10.1063/1.1677527

110.P. C. Hariharan and J. A. Pople, “Influence of polarization functions on molecular-orbital hydrogenation energies,” Theor. Chem. Acc., 28 (1973) 213-22. http://dx.doi.org/10.1007/BF00533485 P. C. Hariharan and J. A. Pople, “Accuracy of AH equilibrium geometries by single determinant molecular-orbital theory,” Mol. Phys., 27 (1974) 209-14. http://dx.doi.org/10.1080/00268977400100171 M. S. Gordon, “The isomers of silacyclopropane,” Chem. Phys. Lett., 76 (1980) 163-68. http://dx.doi.org/10.1016/0009-2614(80)80628-2

111.M. M. Francl, W. J. Pietro, W. J. Hehre, J. S. Binkley, D. J. DeFrees, J. A. Pople, and M. S. Gordon, “Self-Consistent Molecular Orbital Methods. 23. A polarization-type basis set for 2nd-row elements,” J. Chem. Phys., 77 (1982) 3654-65. http://dx.doi.org/10.1063/1.444267

112.R. C. Binning Jr. and L. A. Curtiss, “Compact contracted basis-sets for 3rd-row atoms – GA-KR,” J. Comp. Chem., 11 (1990) 1206-16. http://dx.doi.org/10.1002/jcc.540111013

113.J.-P. Blaudeau, M. P. McGrath, L. A. Curtiss, and L. Radom, “Extension of Gaussian-2 (G2) theory to molecules containing third-row atoms K and Ca,” J. Chem. Phys., 107 (1997) 5016-21. http://dx.doi.org/10.1063/1.474865

114.V. A. Rassolov, J. A. Pople, M. A. Ratner, and T. L. Windus, “6-31G* basis set for atoms K through Zn,” J. Chem. Phys., 109 (1998) 1223-29. http://dx.doi.org/10.1063/1.476673

115.V. A. Rassolov, M. A. Ratner, J. A. Pople, P. C. Redfern, and L. A. Curtiss, “6-31G* Basis Set for Third-Row Atoms,” J. Comp. Chem., 22 (2001) 976-84. http://dx.doi.org/10.1002/jcc.1058

Appendices

List of Abbreviations

HMGCR (HMGR) - β-hydroxy-β-methylglutaryl-CoA reductase

HMG-CoA - β-hydroxy-β-methylglutaryl-CoA

HMG - β-hydroxy-β-methylglutaryl

CoA - coenzyme A

NADPH - dihydronicotinamide-adenine dinucleotide phosphate

COOH - carboxylate

Ser - serin

Asp - aspartate

Lys - lysine

Glu - glutamate

Leu - leucine

Val - valin

Ala - alanin

K_i - the inhibitory constant

His - histidine

pKa - acid dissociation constant

RMSd - root

CoA-S$^-$ - deprotonated coenzyme A

MD - Molecular Dynamics

MM - Molecular Mechanics

HF - Hartree-Fock

Pos-HF - Post-Hartree-Fock

DFT - Density-Functional Theory

QM/MM - quantum mechanics/molecular mechanics

PES - Potential Energy Surface

2D - two-dimensional

3D - three-dimensional

STOs - Slater-type orbitals

GTOs - Gaussian-type orbitals

$\hat{H}$ - Hamiltonian

AM1 - Austin model 1

PM3 - Parametrised model 3

B3LYP - Becke, 3-parameter, Lee-Yang-Parr.

AMBER - Assisted Model Building with Energy Refinement

ONIOM - Our Own N-layered Integrated Molecular Orbital

CHARM - Chemistry at HARvard Macromolecular Mechanics

OPLS - Optimized Potential for Liquid Simulations

E_a - the activation energy

E_r - the reaction energy

ΔG - the Gibbs free energy

Index of Tables

Index of Figures

Biography

Paula Mihaljević-Jurič was born on 20th August 1991 in Osijek, Croatia. She was raised in Belišće, a small town 30 km from Osijek, where she lived her entire life and attended Elementary school I. Kukuljević. After that, she attended General-Education High School of Valpovo and graduated in 2010/2011. During those years she attended English and French lessons, as well as guitar lessons. In 2011 she enrolled her self in the first year of Undergraduate study of Chemistry at Department of Chemistry (University of Osijek). In 2014/2015 she was awarded an Erasmus$^+$ fellowship for Marmara University in Istanbul, Turkey. Upon her return, she enrolled herself in the Master program of Chemistry at her home faculty in Osijek. She was awarded another Erasmus$^+$ fellowship in 2017/2018 for University of Porto, where she studied a catalytic mechanism of HMG-CoA reductase with the QM/MM methods, which was the main focus of her Master thesis, *The Mechanism of Reduction of HMG-CoA Catalyzed by Human HMG-CoA Reductase*. On Fall 2018 she will start her PhD project "*Structure And Function of The Ribosome From Molecular Simulations*" in prof. Thomas Simonson's group at École polytechnique (France).

References

1. Conference paper in proceedings: Šter, Anamarija; Medvidović-Kosanović, Martina; Balić, Tomislav; Ćurić, Iva; Mihaljević-Jurič, Paula, Electrochemical characterization of (1E)-1-N-{; ; [4-(4-{; ; [(E)-N-(4- aminophenyl) carboxyimidoyl] phenoxy} butoxy) phenyl]methylidene} benzene-1, 4-diamine, Proceedings of International Scientific and Professional Conference 15th Ružička Days "Today Science – Tomorrow Industry" (2014).

2. Poster presentation: Šter, Anamarija; Medvidović-Kosanović, Martina; Balić, Tomislav; Ćurić, Iva; Mihaljević-Jurić, Paula, Electrochemical characterization of (1E)-1-N- {;[4-(4-{;[(E)-N-(4- aminophenyl)carboxyimidoyl]phenoxy};butoxy) phenyl] methilidene};benzene -1, 4-diamine, *15th Ružička days "Today science – tommorow industry"* / Osijek: Faculty of Food Technology Osijek ; HDKI, (2014).